universität wien

MASTERARBEIT / MASTER'S THESIS

Titel der Masterarbeit / Title of the Master's Thesis

„Petrography and Geochemistry of the Impact to Post-Impact Transition Layer at the El'gygytgyn Impact Structure in Chukotka, Arctic Russia"

verfasst von / submitted by

Karin Maierhofer B.Sc.

angestrebter akademischer Grad / in partial fulfilment of the requirements for the degree of

Master of Science (M.Sc.)

Wien, 2018 / Vienna 2018

Studienkennzahl lt. Studienblatt / degree programme code as it appears on the student record sheet:	A 066 815
Studienrichtung lt. Studienblatt / degree programme as it appears on the student record sheet:	Erdwissenschaften
Betreut von / Supervisor:	Univ. -Prof. Dr. Christian Koeberl

Statutory Declaration

I declare that I have authored this thesis independently, that I have not used other than the declared sources/resources, and that I have explicitly marked all material which has been quoted either literally or by content from the used source.

_____	_____
Date	*Signature*

Danksagung

Ich möchte hiermit allen danken, die mich während meiner Studienzeit unterstützt und begleitet haben und all denen, die zum Gelingen der hier vorliegenden Arbeit beigetragen haben.

Besonders danken möchte meinen Betreuer Herrn Univ.-Prof. Dr. Christian Koeberl, der mir die Möglichkeit eröffnet hat, in einem sehr speziellen Gebiet der Erdwissenschaften Erfahrungen zu sammeln. Ich durfte die Tagung der „Meteoritical Society“ in Berlin besuchen und mit einem Poster meine anfänglichen Schritte dieser Arbeit präsentieren.

Herzlich danken möchte ich Dr. Lidia Pittarello und Dr. Ludovic Ferriere. Ihr wart mir eine sehr wertvolle Unterstützung und ich konnte durch euch sehr viel lernen, auch wenn eure Zeit sehr begrenzt war. Ein besonderes Dankeschön gilt Dr. Dieter Mader für die Betreuung bei der Neutronenaktivierungsanalyse.

An der Mikrosonde wurde ich von Herrn Dr. Dan Topa betreut, dessen Hilfe ausgesprochen wertvoll war. Auch den Dünnschliffpräparatoren des Naturhistorischen Museum, Goran Batic, und der Universität Wien, Ilka Wünsche, gilt ein ganz besonderer Dank.

Ganz besonders möchte ich mich bei meinem Partner, Christian, bedanken, der mir in dieser Zeit mit unglaublich viel Positivität zur Seite stand und der nie aufgehört hat an mich zu glauben. Auch meinen Freunden, Jessica, Daniela und Elisa, gilt ein ganz besonderer Dank. Überdies bin ich auch sehr dankbar über die Unterstützung von meinen Studienkollegen, Waltraud, Silvia, Kathi, Ruth und Philipp. Ihr alle habt mir wirklich viel Motivation geschenkt und weitergeholfen.

Abschließend möchte ich meinen unglaublich phantastischen Eltern, meinen Brüdern und meiner Familie danken. Das tiefe Vertrauen, dass ihr in mich habt, bedeutet mir unendlich viel. Ich kann in jeden Lebenslagen auf euch zählen. Dankeschön.

Abstract

The 3.6 Ma old impact structure El'gygytgyn, located in north-east Chukotka in arctic Russia, was formed mostly in acidic volcanic rocks. The 18 km in diameter circular depression is filled with Lake El'gygytgyn (with a diameter of 12 km) that contains a continuous record of lacustrine sediments of the Arctic from the past 2.8 Ma (Melles et al. 2011). In 2009, El'gygytgyn became the focus of the International Continental Scientific Drilling Program (ICDP). This project took almost a decade to come to fruition due to financial and logistical challenges. The recovery of a total of 642.4 m of drill core from two sites, from four holes, yielded material including sedimentary and impactite rocks.

Lithostratigraphically, the drill cores comprise lacustrine sediment sequences, impact breccias, and deformed target rocks. The impactite core was recovered from 316.08 to 517.30 meters below lake floor (mblf). The target rocks are part of the Late Cretaceous Okhotsk-Chukotka Volcanic Belt and consist of lavas, tuffs, ignimbrites of rhyolitic, dacitic, and andesitic compositions, including modest intercalations of basalt.

In the process of this master's thesis, the transition zone, ranging from 311.467 to 317.38, between the post-impact lacustrine sediments and the impactite sequences, was studied petrographically and geochemically. The transition layer comprises a mixture of six meters of loose sedimentary and volcanic material containing isolated clasts. Petrographical investigations of the transition layer were conducted on 27 polished thin sections of 23 samples, using optical and electron microscopy, and raman spectroscopy. Shock metamorphic effects, such as planar fractures (PFs) and planar deformation features (PDFs), were observed in a few quartz grains. The discoveries of silica diaplectic glass hosting coesite, kinked micas and amphibole, lechatelierite, numerous impact melt shards and clasts, and spherules are associated with the impact event. Geochemical investigations of selected samples include bulk rock analyses measured via instrumental neutron activation analyses (INAA), as well as major element analyses of minerals, spherules, and melt clasts measured by electron probe micro analysis (EPMA).

The occurrence of spherules, impact melt clasts, silica diaplectic glass, and lechatelierte, about one meter below the onset of the transition marks the beginning of the more coherent impact ejecta layer. The results of siderophile interelement ratios of the transition layer spherules give indications of the contribution of a meteoritical component. Similar results for spherules, but from the impactite drill core, were documented by Goderis et al. (2013), who concluded that a LL-chondrite represents the most probable projectile.

Zusammenfassung

Der 3.6 Millionen Jahre alte Impaktkrater El'gygytgyn, welcher sich in Nord-Ost Chukotka im arktischen Russland befindet ist der bisher einzig bekannte Meteoritenkrater, der in sauren vulkanischen Gesteinen gebildet wurde. Mit einem Durchmesser von 18 km ist diese kreisförmige Impaktstruktur vom El'gygytgyn See gefüllt, der von den letzten 2.8 Million Jahren eine kontinuierliche Abfolge lakustriner Sedimente beinhaltet (Melles et al. 2011). Aufgrund dieser Besonderheiten wurde El'gygytgyn im Jahr 2009 der Mittelpunkt des International Continental Scientific Drilling Programes (ICDP). Es wurde ein Bohrkernmaterial mit einer Gesamtlänge von 642.4 m an zwei Standorten, von vier Bohrlöchern geborgen, das Sedimente und Impaktgesteine enthält. Lithostratigraphisch umfassen die Bohrkerne Sequenzen der lakustrinen Sedimente, Impaktbreckzien, und deformierte Ausgangsgesteine. The Impaktit-Bohrkern wurde ab einer Tiefe von 316.08 bis 517.30 mblf (meters below lake floor) geborgen. Die Ausgangsgesteine sind ein Teil des Okhotsk-Chukotka Vulkangürtels (OCVB) und beinhalten Lava, Tuff, Ignimbrit mit rhyolitischer, dacitischer und andesitischer Zusammensetzung, und geringe Vorkommen von Basalt.

Im Zuge dieser Masterarbeit wurde die Übergangszone, von 311.467 bis 317.38 Metern unter dem Seeboden, petrographisch, sowie auch geochemisch, untersucht. Die Übergangszone findet sich zwischen den post-impakt lakustrinen Sedimenten und den Impaktsequenzen, und schließt etwa sechs Meter von losen sedimentären und vulkanischem Material mit gesonderten Klasten ein. Petrographische Untersuchgen wurden an 27 polierten Dünnschliffen aus 23 Proben mit Hilfe optischer Mikroskopie, Raman-Spektroskopie, und Rasterelektronenmikroskopie durchgeführt. Planare Brüche und planare Deformationsstrukturen konnten in einigen Quarzkörnern beobachtet werden. Überdies kann die Entdeckung von diaplektischen Quarzgläsern, Lechatelierit, Impaktgläsern, Sphärulen, und deformierte Glimmer und Amphibole, auf den Impakt zurückgeführt werden. Anschließend wurden ausgewählte Proben geochemischen Untersuchungen unterzogen. Diese beinhalteten Messungen mit Hilfe der Neutronenaktivierungsanalyse von Gesamtgesteinsproben und quantitative Analysen von Mineralen, Impaktgläsern und Sphärulen mittels der Elektronenstrahlmikrosonde (EPMA). Das Auftreten von Sphärulen, Impaktgläsern, diaplektischen Quarzgläsern mit Coesit, und Lechatelierite, schon etwa einem Meter unter dem Beginn der Übergangzone, kennzeichnet den Beginn des einheitlichen Impakt-Ejekta Sequenz. Die Ergebnisse von siderophilen interelement Verhältnissen in den Spherulen der Übergangszone zeigen, das mögliche Vorhandensein einer meteoritischen Komponente. Ähnliche Ergebnisse von Sphärulen des Impaktit-Bohrkernes wurden von Goderis et al. (2013) dokumentiert, welcher einen LL- Chondriten als wahrscheinliches Projektil vermutet.

Table of contents

CHAPTER 1

Introduction

1.1 Thesis Objectives

Within the framework of this master's thesis, entitled "Petrography and Geochemistry from the Impact to Post-Impact Transition Layer at the El'gygytgyn Impact Structure in Chukotka, Arctic Russia", the main objective was to determine the petrological as well as the geochemical characteristics of the transition layer, which has a thickness of about six meters, in a drill core within the El'gygytgyn impact structure in the northeast of Russia, Siberia. Scientific investigations in the course of this work were performed at the Department of Mineralogy and Petrography at the Natural History Museum in Vienna, at the Department of Lithospheric Research at the University of Vienna, and the Karl Franzens University in Graz.

Located in the far north-eastern part of Russia (67°30'N, 172°05'E, Fig.1), on the Chukotka peninsula, the El'gygytgyn impact crater represents a 3.6 million year old structure that was formed mostly in acidic volcanic rocks. The 18-km-diameter circular depression is filled mostly by Lake El'gygytgyn (with a diameter of 12 kilometers), which serves as an ideal sediment trap containing important paleoclimatic information. Today, the lake reaches a depth of roughly 170 meters.

Historically, the El'gygytgyn structure was first described as a massive volcanic crater in 1933 (Obruchev 1957). Many years later, in 1963, it was first suggested by Nekrasov and Raudonis

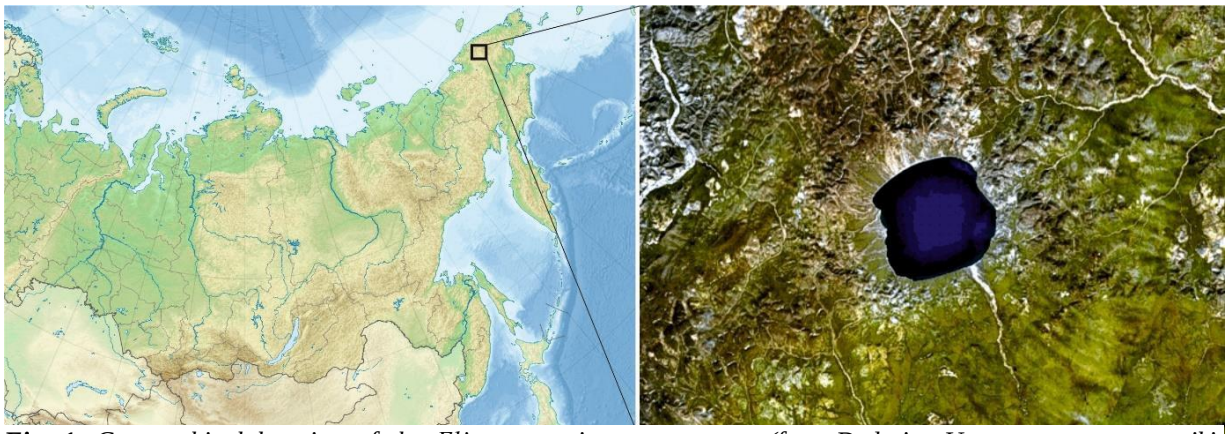

Fig. 1. *Geographical location of the El'gygytgyn impact structure (from Dedering Uwe, www.commons.wikimedia.org), including a satellite image (Landsat) of the area (from NASA, www.earthobservatory.nasa.gov). It is located in northeastern Siberia, on the Chukotka peninsula. The lake reaches a depth of roughly 170 m and a diameter of about 12 km. The impact structure itself is 18 km in diameter.*

that this particular structure could be of impact origin. The fruitless search for coesite in thin sections from samples from the volcanic rocks at the crater rim led to the conclusion that it must reflect a structure that was formed tectonically and volcanically. Studies of satellite imagery by Dietz and McHone (1976), led to the conclusion that El'gygytgyn was probably the largest Quaternary impact crater preserved on Earth. In 1977, Gurov and workers visited the structure and finally confirmed its impact origin. The discoveries of shock metamorphosed rocks and impact melt rocks was responsible for this interpretation. The investigations by this group continued until the 1980s and 1990s. Feldman et al. (1981) provided a short geological description of the crater and its target. In the course of the work from Feldman et al. (1981), the main types of impact melt rocks and highly shocked volcanic rocks were characterized. Geochemical studies of volcanic rock pebbles from eleven different sites on the beach of Lake El'gygytgyn had also been executed. The first geophysical investigations were carried out by Dabizha and Feldman (1982). Despite the confirmation of El'gygytgyn's impact origin, an endogenic origin was once again proposed by Belyi (1982).

Concerning age determinations, early results were obtained by Storzer and Wagner (1979) by fission track dating and yielded ages of 4.52 ± 0.11 Ma. Additionally, K-Ar dating by Gurov et al. (1979) led to ages of 3.50 ± 0.50 Ma. Later fission track ages indicated an age for the crater of 3.45 ± 0.15 Ma (Komarov et al. 1983). Layer (2000) used the ^{40}Ar-^{39}Ar- dating method and found an age of 3.58 ± 0.04 Ma for the impact glasses. This is still the best available age of the impact event at El'gygytgyn.

CHAPTER 2

Impact Cratering

Impact craters are the most common features on various objects with solid surfaces in the solar system such as planets and satellites. Active tectonics, as well as erosion and atmospheric processes on Earth, give these landforms a very short lifespan. In contrast, the Moon is covered with numerous craters reflecting the absence of active tectonics and an atmosphere. So far, 190 impact craters have been confirmed on Earth (e.g., Fig. 2), although, these are just the ones that are preserved in its history. It is certain that the Earth has endured more bashing that one might expect. About one third of these known craters are not exposed on the surface (e.g., Koeberl and Milkereit 2007). These craters can only be studied by geophysics and drilling. The oldest known impact structure dates to 2.02 Ga (billion years), but there are only few craters that are older than 700 Ma (million years) (Bailer- Jones 2011).

Fig. 2. *The Barringer crater in Arizona's desert (from Seip Stefan, www.faz.net), east of Flagstaff, which is about 50 000 years old. Its good preservation is caused by the local arid climatic conditions.*

The process of impact cratering represents the excavation of a crater on a planet's or satellite's surface, after it is struck by a meteoroid. Such an incident requires large meteorites that are hundreds of meters in diameter, containing a large amount of kinetic energy. These large bodies can pass through the Earth's atmosphere and explode on impact with the Earth, resulting in massive circular depressions that are more than ten times larger than the diameters of the impactors. On a global scale, the release of dust and smoke as well as a vast amount of energy causes environmental damage and a drastic change in climate. Such events led to several global extinction events in the geologic past.

2.1. Formation of Impact Craters

The formation of impact craters is linked to a sudden release of a huge amount of energy, wherefore the study of such events is set to limitations. Even reconstructing these processes in the laboratory is impossible. For those reasons, all the knowledge about large impact structures is indirect and is strongly dependent on connecting several areas of research (e.g., experimental production of shock waves, experimental production of small craters, geological studies of larger terrestrial impact craters). Based on the results of these studies, meteorite impact craters form in three stages (e.g., French 1998):

1. Compression stage
2. Excavation stage
3. Post-formation Modification stage.

The compression stage begins when the kinetic energy of the projectile is instantly transferred into the target rocks. This happens via two compressional waves. The first wave travels from the projectile's front to the back through the meteorite. The second one moves downward to the target rocks. The compressional wave will generate a pressure of several million bars in the target rocks, if the meteorite's velocity is about 10 km/s. These instantaneous generated pressures cause the target rocks to pulverize, melt, and even vaporize. Furthermore, even textural and crystallographic changes within the target rocks and its minerals occur. Such shock metamorphic features include, e.g., shatter cones, planar deformation features, diaplectic glass, and spherules. The duration of the compression stage only lasts from one thousandth to one tenth of a second, depending on the impactor's diameter. The larger the meteorite, the "longer" the compression stage (Melosh 1989).

Decompression of the rocks generates a relaxation wave that is characteristic for the excavation stage. All the fragments of the crushed rocks are thrown out of the crater, forming the ejecta blanket which surrounds the crater. This ejected material can be described as a symmetric excavation flow around the center of the developing structure that reflects a cone-shaped curtain forming rays on the ground. Some of the ejected material may even fall back into the crater, creating a deposit of fallback breccia, which is exposed to a residual heat within the crater. This heat causes the fallback breccia to melt and subsequently to crystallize forming a rock called impactite (Faure and Mensing 2007). The crater size is strongly dependent on the mass and velocity of the meteorite as well as on the mechanical properties of the target rocks. There is a relation between the diameter of the crater and the kinetic energy of the impactor. The diameter increases exponentially with increasing kinetic energy of the impacting meteoroid.

After the crater reaches its maximum size, the excavation stage ends and grades into the post-forming modification stage. By this stage, the shock waves degrade into low-pressure elastic stress waves beyond the crater rim. The crater is immediately modified by gravity and rock mechanics (Faure and Mensing 2007). There is no clearly marked ending for the modification stage. These processes merge gradually into the normal processes of erosion, sedimentation, mass movement, and isostatic uplift.

2.2. Classification of Craters

The transient crater will be altered during the modification stage. The extent of these alterations depend on the crater size and the structure, and properties of the target rock. Alteration of small craters includes the collapse of the upper walls. As a result, the shape of the final crater exhibits slight changes from that of the original transient crater. Major modifications in larger craters contain uplift of the central part of the floor and peripheral collapse around the rim. Three types of craters can be distinguished, depending on the extent of the modifications of the transient crater (e.g., French 1998):

- Simple craters
- Complex craters
- Multiring basins.

Simple craters occur as bowl-shaped depressions which are less than a few kilometers in diameter (Fig. 3). The transient crater is modified only by minor collapse of the steep upper walls into the crater cavity. Little ejected material is redeposited in the crater as well. The resulting crater may exhibit an increase of 20% in diameter, however, the original transient crater depth remains mainly unaffected (e.g., French 1998). Redeposited (fallback) ejecta and debris from the walls and rim may fill the crater to half of its original depth. This crater fill-breccia represents a mixture of fragmented rocks hosting shocked and non-shocked particles and fragments of impact melt (shock melted rock).

Complex craters form in larger impact events and are marked by a centrally uplifted region, a flat floor, and extensive inward collapse around the rim (Fig. 4) (French 1998). The transition between simple and complex craters on Earth occurs at a diameter of 4 km in massive crystalline rocks, and only at 2 km in sedimentary rocks. The fact that the formation of larger impact craters is linked to the release of a vast amount of energy results in complex interactions between shock-wave effects, gravity, and strength and structure of the target rocks (French 1998). Detailed knowledge about these complex interactions is uncertain. However, the main result is that

the original bowl-shaped transient crater immediately forms a central uplift. Deep-seated rocks beneath the crater center rise as rocks at the periphery of the transient crater collapse downward and inward along concentric faults, forming depressed rings (ring grabens) and several terraces at the outer margins of the final structure (Melosh 1989). Theoretical as well as field studies revealed that central uplifts form within only a few minutes, even in large structures. The exact processes behind the formation of central uplifts are still uncertain and of active debate. It can be noted that at larger crater diameters, the structures of the centrally uplifted area becomes more complicated. An increase in crater size yields a central uplift that replaces the central peak by a more complex series of concentric rings and basins.

Multiring basins are restricted to impact craters that have diameters of a few hundred kilometers to more than 1000 km. At an early period in the solar system such massive objects and collisions were more abundant, wherefore these impact structures are restricted to ages of ≥ 3.9 Ga (French 1998). As a result, the preserved multiring basins are to find on well-preserved ancient surfaces such as the Moon, Mercury, or part of Mars.

There are just a few impact craters on Earth that are of these sizes, but most of them are deeply eroded, or even buried, resulting that it is strongly debated whether or not multiring basins exist on Earth. Possible multiring basins would be the Chicxulub impact structure, which is buried underneath the Yucatán Peninsula, or even the Vredefort impact structure in South Africa.

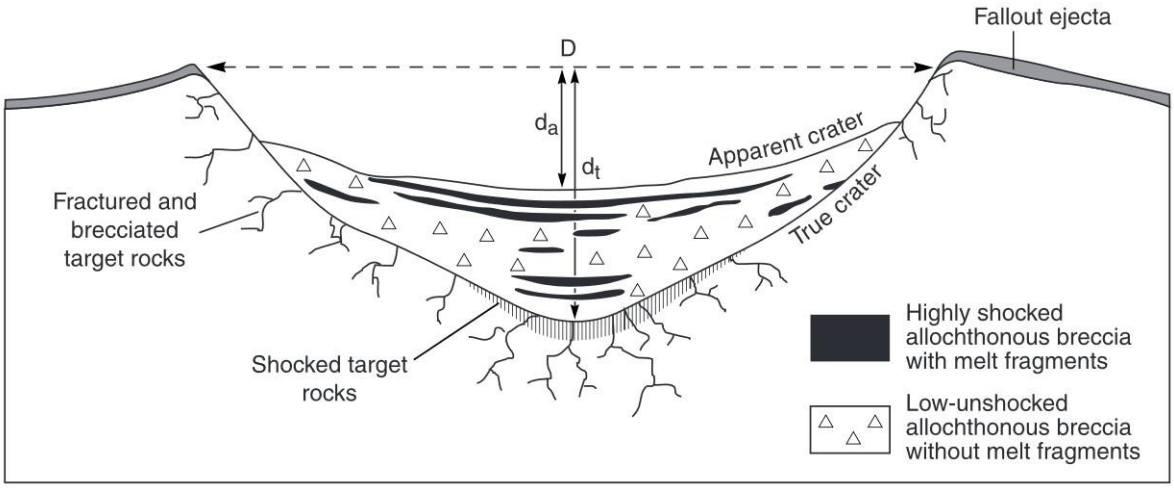

Fig. 3. *Schematic cross section of a bowl-shaped simple impact crater and the various locations of impactites from French (1998). D represents the final crater diameter which is about 20% greater than the diameter of the original transient crater. d_a=apparent depth of the crater; d_t=true depth of the final crater.*

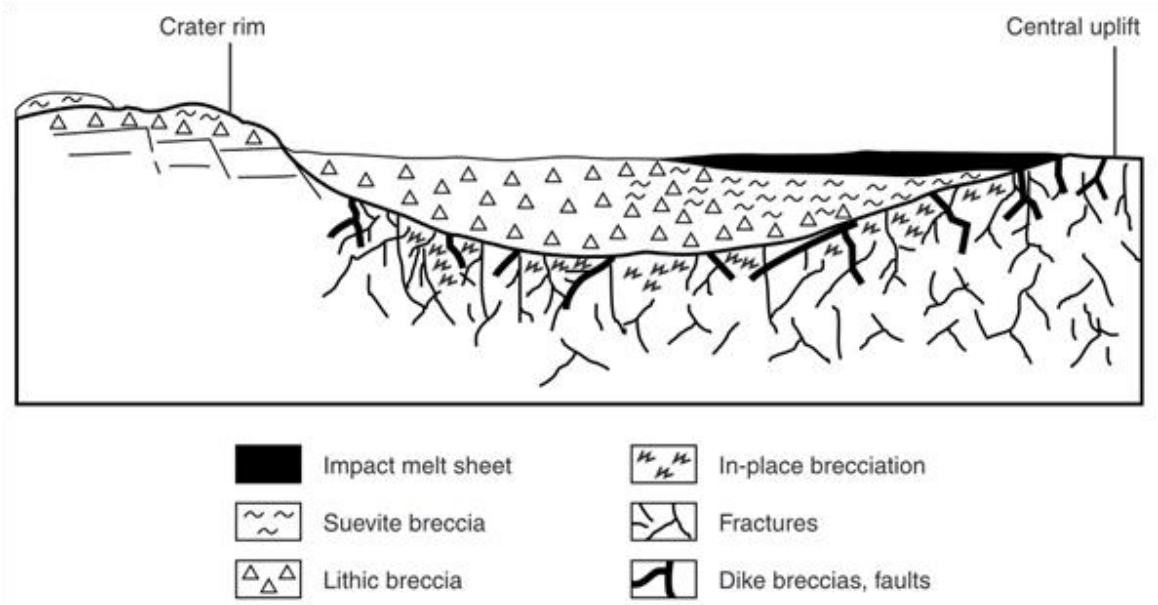

Fig. 4. *Schematic radial cross section of a complex impact crater from French (1998) displaying the section from the central uplift (right) to the outer, downfaulted rim (left).*

2.3 Impactites

"Impactites represent rocks that have been affected by one or more hypervelocity impact(s) resulting from collision(s) of planetary bodies" based on the classification by Stöffler and Grieve (2007). Basically, impactites are classified by texture, degree of shock metamorphism, and lithological components. Impactites that were formed from a single impact are classified in three major groups (Fig. 5):

(1) Shocked rocks
(2) Impact melt rocks
(3) Impact breccias.

Shocked rocks (1) are non-brecciated rocks which exhibit explicit effects of shock metamorphism. These can be subclassified into progressive stages of shock metamorphism. Impact melt rocks (2) can be divided into three subgroups, based on the content of clasts. Furthermore, the degree of crystallinity into glassy, hypocrystalline, and holocrystalline may also be used for subclassifying within the three subgroups. Impact breccias (3) can be divided into three subgroups. In this case the degree of mixing of various target lithologies and the content of melt particles are taken into account (Stöffler and Grieve 2007).

Impactites can be roughly classified also in proximal and distal impactites. The ones that are deposited within a distance of less than 2.5 crater diameters are called proximal, whereas distal impactites are found in greater distances.

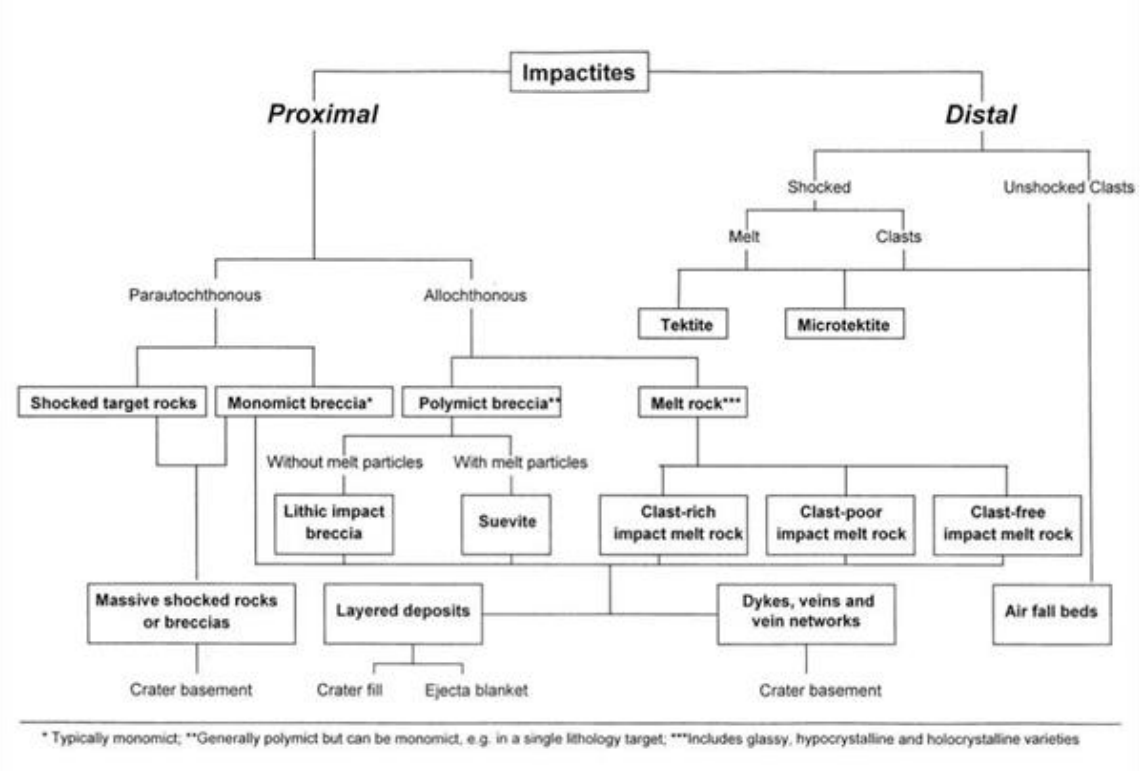

Fig. 5. *Classification of impactites based on single impacts, from Stöffler and Grieve (2007).*

2.4 Shock Metamorphism

Shock metamorphism describes the impact related transformation of rocks, including their minerals under extreme temperature and pressure conditions. Peak-shock pressures that are reached in an impact event range from ≤ 2 GPa to >100 GPa, near the final crater rim and near the impact point, respectively. Such pressures as well as extreme shock-deformation effects cannot be compared to normal geologic processes. Shock waves travel many kilometers per second and cause the volume of a mineral grain or rock sample to change in microseconds. Therefore shock deformation characteristics reflect transient stress conditions, high strain rates, and rapid quenching. They also deposit energy in the passing material producing post-shock temperatures, which are dependent on the material of the target rocks. Post-shock temperatures increase with increasing shock pressure. These temperatures can get so high, causing the target rocks to melt or even vaporize. The changes expressed within the target rocks due to shock are dependent on the shock pressures. Low shock pressures ranging from ~2-10 GPa produce macroscopically visible shatter cones. Pressures from 10 to 45 GPa produce high-pressure mineral polymorphs and microscopic deformation features in minerals such as quartz or feldspar. Pressures

greater than 50 GPa, result in partial to complete melting as well as vaporization (>100 GPa) of vast amounts of target rocks. Figure 6 displays the effects resulting from increasing shock pressures, after French (1998). There have been a wide variety of shock-produced microscopic deformation features identified so far, including kink bands in micas and rarely in olivine and pyroxene, different types of planar microstructures in quartz, feldspar, and other minerals, isotropic mineral glasses (diaplectic or thetomorphic glasses) most commonly in quartz and feldspar, and selective melting of individual minerals. Kink bands however, can also form within normal tectonic environments and are therefore not diagnostic of shock.

Approximate Shock Pressure (GPa)	Estimated Postshock Temperature (°C)*	Effects
2–6	<100	Rock fracturing; breccia formation
		Shatter cones
5–7	100	Mineral fracturing: (0001) and {10$\bar{1}$1} in quartz
8–10	100	Basal Brazil twins (0001)
10	100*	
		Quartz with PDFs {10$\bar{1}$3}
12–15	150	Quartz → stishovite
13	150	Graphite → cubic diamond
20	170*	
		Quartz with PDFs {10$\bar{1}$2}, etc. Quartz, feldspar with reduced refractive indexes, lowered birefringence
>30	275	Quartz → coesite
35	300	
		Diaplectic quartz, feldspar glasses
45	900	Normal (melted) feldspar glass (vesiculated)
60	>1500	Rock glasses, crystallized melt rocks (quenched from liquids)
80–100	>2500	Rock glasses (condensed from vapor)

Fig. 6. *Shock pressures and effects from French (1998). *For dense non-porous rocks. For porous rocks (e.g. sandstones): post-shock temperatures = 700°C (P = 10 GPa) and 1560 °C (P = 20 GPa). Data from Stöffler (1984), Melosh (1989) and Stöffler and Langenhorst (1994).*

CHAPTER 3

Geological Setting

The 18 km in diameter and 3.58 ± 0.04 million years old (Layer 2000) El'gygytgyn impact structure is located in the northeast of Russia, Siberia, on the Chukotka peninsula (67°30'N and 172°34'E). Geologically, this impact structure is situated in the Okhotsk-Chukotka Volcanic Belt (OCVB), which extends from the western coast of the sea of Okhotsk to the Chaplino settlement east of Chukchi Peninsula, and reaches a length up to approximately 3250 km (Fig. 7). Currently, the outcrop area constitutes about 450 000 km^2 and the total volume of erupted material was estimated as more than 1 x 106 km^3 (Belyi 1977, 1994). The OCVB represents a considerable part of the Mesozoic arc system of the Circum-Pacific (Tikhomirov et al. 2012). Compared to other subduction related volcanic belts the OCVB contains an unusual high amount of silicic rocks (from 80 to 85%). Geological studies of this area started in the early 1930s due to occurrences of economic mineral resources, such as gold, silver, tin, and mercury.

3.1 Geology of the Okhotsk-Chukotka Volcanic Belt (OCVB)

As a result of subduction along an Andean-type convergent margin, the OCVB formed in the late Cretaceous followed by extension (Newberry et al. 1998). Part of the ancestral Pacific oceanic plate was subducted preserving forearc basins in the West Kamchatka, Ekonay, and Yanranay accretionary-wedge terranes (Akinin et al. 2014) The OCVB can be divided into three structural elements: (a) the main arc, (b) the West-Okhotsk, and the (c) East Chukotka flank zones (Sidorov et al. 2009).

The main arc (a) extends from the mouth of the Ul'ya River to the coast of the East Siberian Sea which is known as the Taui-Chaun Arcoline. These three independent structural elements were formed simultaneously in geologic time.

Volcanism at the OCVB had a discontinuous pulsed nature, wherefore several peaks of volcanic activity are distinguishable with modes at approximately 105, 100, 96, 92-93, 87, 82, and 77 Ma (Akinin and Miller 2011). The peaks at 87 and 82 Ma are the strongest in all segments and coincide with the most voluminous stages of middle and late cycles of the felsic ignimbrite

volcanism. At 76-78 Ma the cycles were terminated by aluminous basalts which formed volcanic plateaus. The main stage volcanics are typically calc-alkaline, but differ in alkalinity and exhibit high SiO_2 contents at low Fe/Mg ratios (Akinin et al. 2014).

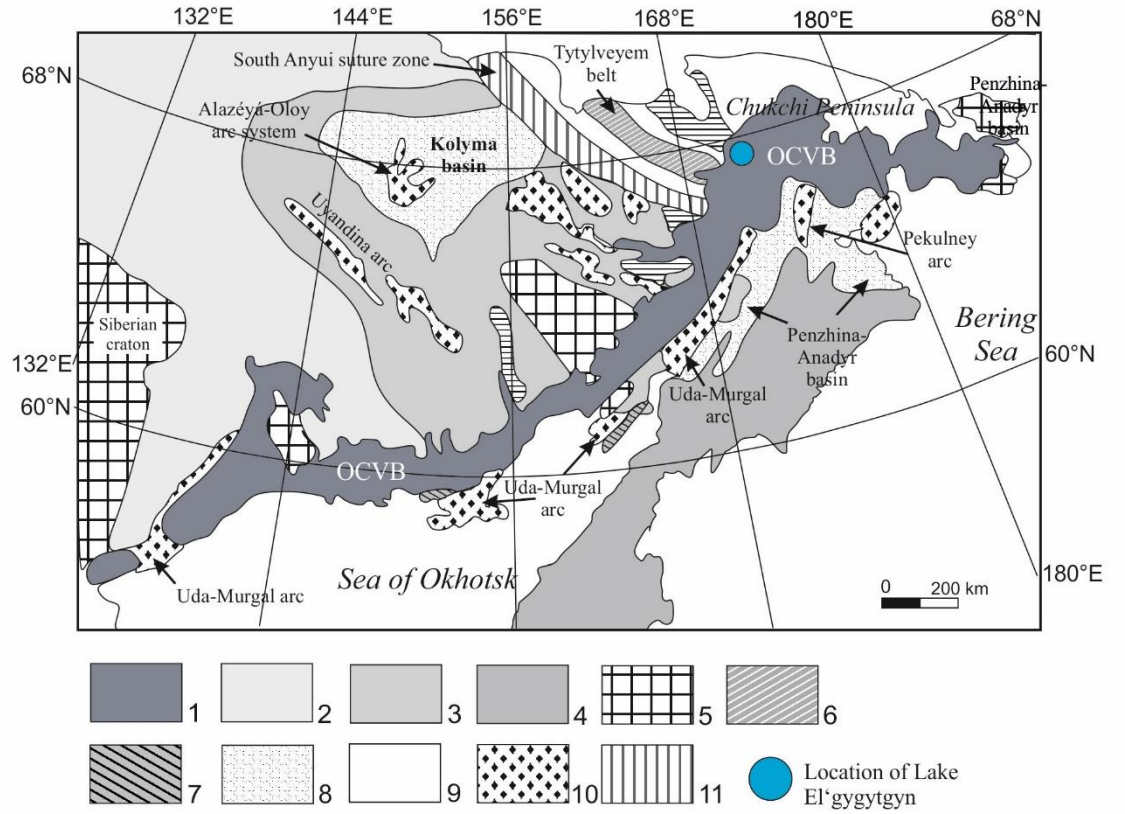

Fig. 7. *Location of the Okhotsk-Chukotka Volcanic Belt in the tectonic frame of northeast Asia, modified after Tilman and Bogdanov (1992), Nokleberg et al. (2001), and Tikhomirov et al. (2012). 1- The Okhotsk-Chukotka Volcanic Belt (OCVB); 2- complexes of the Paleozoic to early Mesozoic passive margin of the Siberian continent; 3- the Kolyma –Omolon superterrane: A tectonic collage of terranes of different nature; 4- the Koryak- Kamchatka tectonic province (various terranes, related mainly to the Late Cretaceous to Cenozoic island arcs, accreted during the Cenozoic era); 5- Siberian craton and minor cratonal blocks; 6- the late orogenic Tytylveyem volcanic belt that is partially eroded; 7- Magadan and South Taigonos batholiths of granitic rocks; 8- Cenozoic continental basin filled with clastic sediments; 9- syn-collisional basins filled by clastic sediments of Late Jurassic to Early Cretaceous; 10- remnants of the Late Jurassic to Early Cretaceous volcanic arcs; 11- South Anyui suture zone.*

The Basement of the OCVB includes various cratonic blocks and several complexes of passive and active continental margins containing rare fragments of ophiolitic sections (Nockleberg et al. 2001 and Sokolov et al. 2002). After Belyi (1994), Filatova (1988) and Sidorov et al. (2009), the OCVB includes two major zones. The inner zone which represents the frontal side of the OCVB (ocean-side) and unconformably overlies the residues of older volcanic arcs of the ancestral Pacific. This zone is composed of andesites and basaltic andesites and evolved from the Late Paleozoic to the Early Albian (Sidorov et al. 2009). The volcanic section of this area comprises a thickness reaching from 4 to 6 km, with a maximum of 7.5 km (Sidorov et al. 2009).

The outer zone, which lies at the margin of the continental side of the OCVB, appears strongly discordant to the major fold axes. It is superimposed on the terranes of the passive continental margin, volcanic arcs, and cratonic terranes. It comprises a greater proportion of silicic rocks, but the volcanic pile is thinner and extends from 2 to 5 km. Stratigraphically, the OCVB can be divided in three main components: The "lower" andesites (1), formations dominated by silicic rocks (2) and the "upper" basalts (3) (Tikhomirov et al. 2012). It should be mentioned that all units formed in a continental environment which is confirmed by the absence of any marine fauna and fossil flora (Tikhomirov et al. 2012). The "lower" andesites (1) comprise basalts, basaltic andesites and andesites, minor dacites, rhyolites and epiclastic interlayers. Lavas are less abundant. After Filatova (1988) the OCVB in the first stages of its formation exhibited stratovolcanoes as the most common type of volcanic objects. The basalts and andesites of the "lower" andesites (1) can be described as porphyritic with phenocrysts of plagioclase (Plag), clinopyroxene (Cpx), orthopyroxene (Opx), Ti-magnetite, amphibole (Amph), and apatite (Ap) (Tikhomirov et al. 2012). Furthermore, Chromium-bearing spinel and olivine may be present in the basalts. The "middle part" (2) is composed of dacites and rhyolites mainly represented as ignimbrites and tuffs. It should be noted that the abundance of ignimbrites generally tends to decrease upwards. Intensely welded ignimbrites, which are composed to thick sequences (1 to 3 km in thickness) are confined to calderas. The silicic volcanics' mineralogy consists of plagioclase (An_{65-10}), amphibole, Na-K-feldspar, biotite (Bt), quartz (Qtz), and both ortho- and clinopyroxene. Accessory minerals are represented by Ti-magnetite, ilmenite (Ilm), apatite, zircon (Zr), allanite (all) and sometimes even garnet (Grt), monazite (Mon), xenotime (Xe), and thorite (Th). The glassy matrix can be described as devitrified. The "upper" part (3) is basaltic with basalts, trachybasalts, basaltic andesites, and basaltic trachyandesites. Some rhyolitic ash-fall tuffs and ignimbrites locally intercalate with mafic tuffs (~10 vol.%). Petrographically, the "upper" basalts (3) exhibit some differences compared to the older mafic rocks of the OCVB. There is a greater percentage of olivine phenocrysts in the "upper" basalts. Titanoferrous augite and/or analcime may also occur.

The geochemical consideration of the "lower" andesites (1) show a well pronounced negative Nb-Ta anomaly and a high LILE/HFSE ratio (Polin and Moll-Stalcup 1999, Kalinina et al. 2008, Akinin and Miller 2011). The "upper" basalts (3) exhibit similar features. However, they are enriched and show characteristics of intraplate-basalts (Filatova 1988, Kalinina et al. 2008). The variations in trace and major element data in the basalts and andesites indicate competing processes of assimilation/mixing and fractional crystallization, during the evolution of the pa-

rental basaltic magma (Akinin and Miller 2011). Furthermore, measurements of initial radiogenic isotope ratios of Sr, Nd, and Pb from volcanics of several segments point to significant lateral heterogeneity of mantle sources of the calc-alkaline magmas (Akinin and Miller 2011).

3.2 The Okhotsk-Chukotka Volcanic Belt at Lake El'gygytgyn

The OCVB at Lake El'gygytgyn is made of subaerial calc-alkaline volcanic rocks including andesites, rhyolites, andesite-basalts sequences (Zonenstrain et al. 1990), diorites, tonalities, granodiorites, quartz-monzonites, and granites (Belyi 1994, Belyi and Belyaa 1998). It is excavated in the outer zone of the OCVB, mainly involving the Pykarvaam series (88 ±1.7 Ma; Stone et al. 2009). Three recognized basic-acidic sequences of volcanic rocks are present on the northern flanks of the OCVB. After Belyi (1994) the first cycle is formed by the lower Chaun series which is exposed in the same region as the Kalen'muvaam unit and in the north of the Enmyvaamsk basin. The second sequence from bottom to top comprises the Pykarvaam, Voronin, and Koekvun sequences (Belyi 1994, 1988). Figure 8 displays the geological map of the El'gygytgyn impact structure, which was modified after Raschke et al. (2014). These sequences form the upper components of volcanic rocks of the Chaun series. The Chaun series is also divided by a major fault from the overlying volcanic rocks which involve the late stage development of the OCVB. Ispolatov et al. 2004 chronicled ages from the first cycle, for the lower Chaun group, of 87.1 – 87.9 Ma. These results imply post Albian ages for the Chaun group (Conacian to Santonian). The third volcanic sequence is made of the Ergyvaam, Emuneret, and Emmyvaam suites. A complete sequence of the second and third cycle is preserved at the area of Lake El'gygytgyn (Stone et al. 2009).

A schematic impact stratigraphy was made by field investigations by E. Gurov and E. Gurova in the 1990s (Gurov and Gurova 1991). From top to bottom this sequence starts with 250 m rhyolitic ignimbrites, followed by 200 m of rhyolitic tuffs and lavas, 70 m of andesitic tuff and lavas, and 100 m of rhyolitic to dacitic ash- and welded tuffs. The northern, southern, and western parts exhibit this sequence. However, in the southeastern and eastern parts of the crater dacites as well as dacitic and andesitic tuffs are dominant (Gurov et al. 2005). An approximately 110 m thick basalt plateau covers the rhyolites and ignimbrites in the northeastern part of the crater rim (Gurov and Koeberl 2004). These basalts are part of the Koekvun volcanic suite which lies above the Pykavaam series (83.1 ± 0.4 Ma; Stone et al. 2009). The most common lithology is represented by pyroclastic deposits of rhyolitic-dacitic composition which approaches 89% in volume. Hence, rhyolitic-dacitic ignimbrites and tuffs represent the general

composition of the target. Mineralogically, the rhyolitic-dacitic ignimbrite consists of quartz grains and clasts, orthoclase (Or_{60-80}), plagioclase (An_{20-30}), biotite, and rare amphibole. All these clasts and/or grains are embedded in a fine-grained clastic matrix mainly consisting of quartz- and feldspar-fragments. Andesites and andesitic tuffs are limited, but if present they contain fragments and clasts of andesine (An_{45} to An_{40}), clinopyroxene, and amphibole (Gurov and Koeberl 2004). The groundmass can be described as fluidal-glassy to fine-grained granular with crystallization of spherulites in margins of mineral grains (Gurov et al. 2005). Chemical compositions of the main type of target rocks are given in Table 1 after Gurov et al. (2005). Dating of unshocked volcanic rocks at the crater area with $^{40}Ar/^{39}Ar$ yielded ages from 89.3-83.2 Ma (Layer 2000). Rocks at the crater rim do not show any characteristic shock metamorphic effects. Shock metamorphosed rocks only occur as redeposited material inside the crater in the lacustrine terraces.

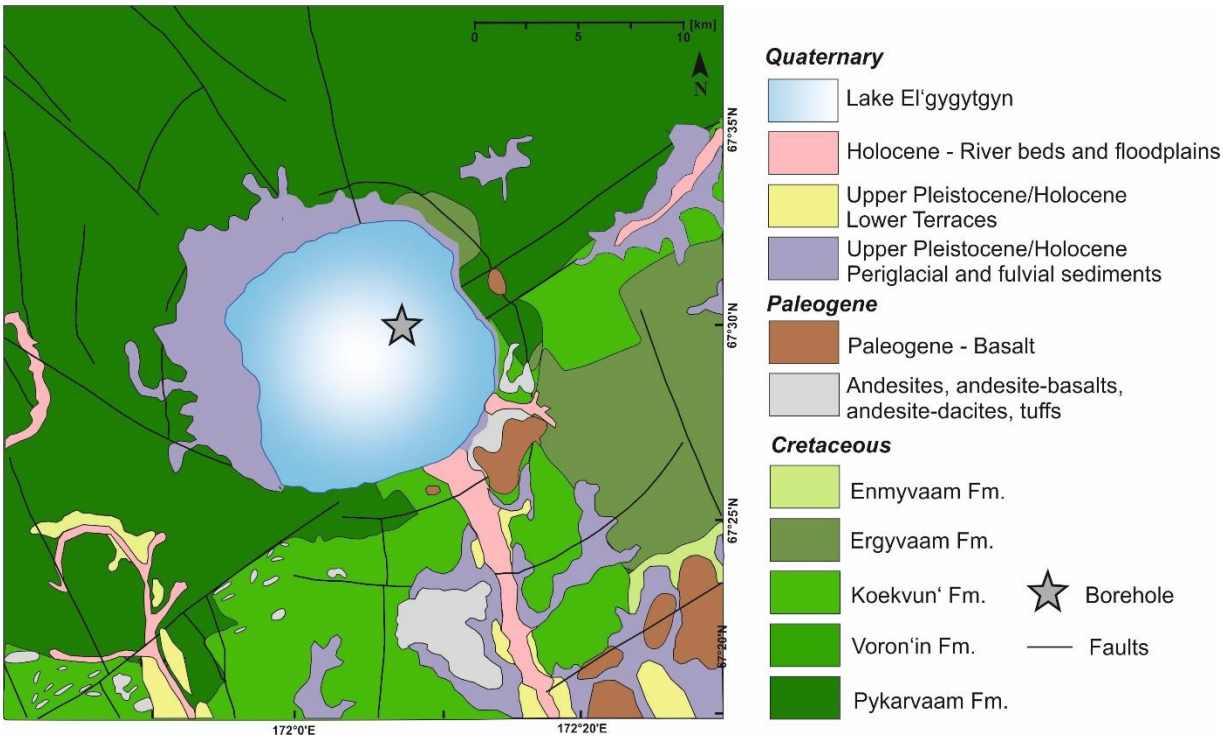

***Fig. 8**. Geological map of the El'gygytgyn impact crater, slightly modified after Raschke et al. (2014).*

Table 1. *Compositions of target rocks from the El'gygytgyn impact crater after Gurov et al. (2005). Major elements in weight percent (wt%). Number in parentheses indicates number of samples. 1- rhyolitic ignimbrite; 2- rhyolitic tuff; 3- rhyolite; 4- andesite, andesitic tuff; 5- rhyolitic ash tuff (lower horizon); 6- regional composition , based on the respective thickness of the various rock types in the target region. The average composition was calculated on the basis of relative proportions of rock types that likely contributed to the target volume.*

	1 (8)	**2 (11)**	**3 (5)**	**4 (5)**	**5 (3)**	**6**
SiO_2	69.94	72.05	72.98	63	73.37	70.72
Al_2O_3	14.52	13.09	12.49	16.57	12.30	13.90
Fe_2O_3	1.9	1.33	1.28	3.4	1.26	1.76
FeO	1	0.76	0.75	1.37	0.49	0.86
MnO	0.08	0.05	0.05	1.12	0.07	0.06
MgO	0.73	0.5	0.48	1.59	0.61	0.72
CaO	2.25	1.37	0.95	3.73	1.66	2.01
Na_2O	2.95	1.97	2.44	3.29	2.3	2.57
K_2O	3.95	4.93	5.79	3.08	5.5	4.48
Li_2O (ppm)	84	91	83	65	82	86
Rb_2O (ppm)	168	176	240	134	238	186
Cs_2O (ppm)	7	10	3	5	2	7
P_2O_5	0.07	0.09	0.04	0.14	0.24	0.1
CO_2	0.65	0.38	0.98	0.91	0.29	0.56
H_2O^-	0.38	0.52	0.31	0.56	0.29	0.39
LOI	1.29	2.24	1.08	1.54	1.47	1.58
Total	100.3	99.8	100.33	101.06	100.32	100.28
Fe_2O_3/FeO	1.9	1.75	1.71	2.48	2.57	2.05

CHAPTER 4

The International Continental Drilling Program (ICDP)

From October 2008 to May 2009 (Brigham-Grette et al. 2007 and Melles et al. 2011), El'gygytgyn was the subject of an International Continental Scientific Drilling Program (ICDP) in which a total of 642.3 meters of drill core was recovered at two sites, from four holes. The objectives of this program were to investigate the lacustrine sedimentary crater fill to reconstruct the Arctic paleoclimatic evolution during the past 3.6 Ma, including permafrost research, and to explore shock metamorphism in siliceous volcanic rocks. Currently, El'gygytgyn in the only known impact crater formed in such lithologies. Impactites on the surface have almost been totally removed by erosion wherefore the deep drilling project yielded a great opportunity to investigate the crater-fill impactites in situ (Koeberl et al. 2013).

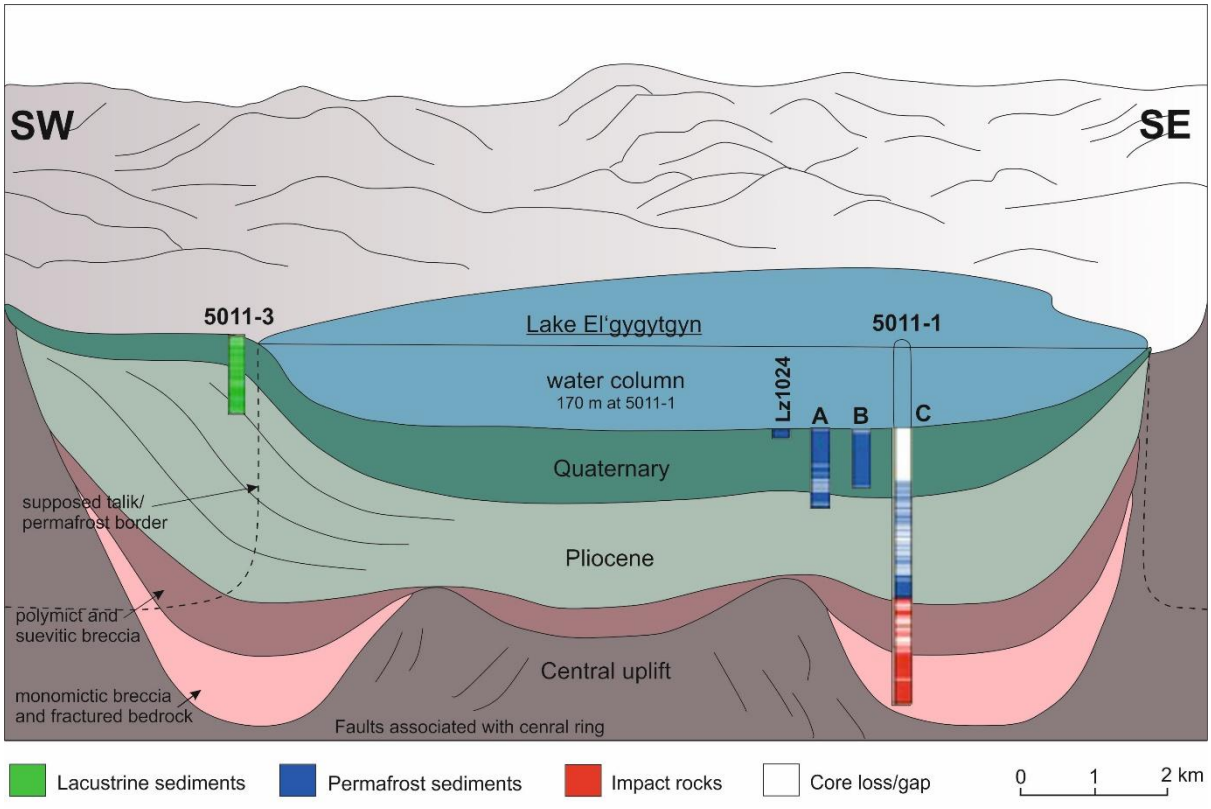

Fig. 9. *Cross-section of the El'gygytgyn impact crater determined by seismic profiles in a predrilling survey, modified after Melles et al. (2011).*

The following description is based on Koeberl et al. (2013). The project resulted in completing one hole into permafrost deposits (ICDP Site 5011-3) in the western lake catchment, and three holes in the center of the lake (ICDP Site 5011-1). The drilling into the permafrost deposits took from November 23 to December 21, 2008 using a mining rig (SIF- 650M). The drill core reached a depth of 141.5 m with a core recovery of 91%. At Site 5011-1 drilling was completed from February 16 to April 26, 2009.

Holes 1A and 1B had to be terminated due to twist-offs at 147 and 112 meters below lake floor, respectively. Drill hole 1C was drilled down to the depth of the impact lithologies which underlie the lacustrine sediments.

The lake sediments were penetrated with an alien bit corer achieving a recovery rate of 52%. The recovery increased to almost 100% at a depth of 265 m due to the change to a hardrock bit corer (HBC). At 315 mblf, the boundary between the lake sediments and the underlain impactites was attained. The drilling continued into the bedrock until reaching a depth of 517 mblf with an average core recovery of 76%, using the hardrock bit corer (HBC). The location of borehole 1C was northeast of the lake center, on the flank of the central uplift. Figure 9 shows the depths, locations, and schematic lithologies of the obtained drill cores.

Drill core 1Dc contains the impactite core which was recovered from 316.75 mblf to a depth of 517.09 mblf. The core boxes were moved from Pevek to St. Petersburg, and on to Germany. In late 2009, the impactite core boxes were transported to the Natural History Museum in Berlin. Research teams around the world were subsequently, provided with several hundred prepared core samples. The transition of the core D1c between the lake sediments and impact rocks was achieved at 315 mblf, as mentioned above.

4.1 Impactite Drill Core Stratigraphy

The impactite and bedrock drill core 1Dc represents a sequence that is about 202 m long, exhibiting a variety of macroscopically discernable properties and strong alterations. Based on studies after Pittarello et al. (2013) the core can be divided into three main parts: (1) about 75 m of suevite and polymict breccia, (2) about 30 m of various volcanic rocks and (3) about 100 m of fractured, welded, rhyolitic-dacitic ignimbrite hosting so-called fiamme of pumice. Based on Stöffler and Grieve (2007) a suevite represents a “polymict impact breccia with clastic material containing lithic and mineral clasts in all stages of shock metamorphism including cogenetic impact melt particles, which are in a glassy or crystallized state.” The suevite and the polymict breccia (1) are intercalated with lacustrine sediments especially in the upper 10 m.

Locally, randomly distributed large blocks of melt rocks, up to 40 cm in size, can be discovered. Volcanic rocks (2), ranging from rhyolitic to basaltic lavas and tuffs as well as ignimbrites, are highly altered. At a depth of 471.40 mblf, the ignimbrites (3) are crosscut by 50 cm thick suevite dyke.

CHAPTER 5

Analytical Methods

The core interval from 311,467 to 317,38 mblf from drill core 1C of ICDP Site 5011-1 arrived at the Natural History Museum in Vienna in June 2016. About a month later, twenty three samples were selected and were studied petrographically and geochemically. To avoid confusion, the depths that were used for this work are consistent with the depths from other impact scientists and correspond to the depths of the drilling report. The depths that were used by the paleoclimatic scientists have been shifted downwards by about three meters. These changes resulted from a correlation with an earlier, shallow drill core (Raschke et al. 2013). The selected samples comprise regular sections from 311.467 to 317.38 mblf from the drill core in order to cover all lithological changes, as well as to gain a statistically meaningful analysis.

5.1 Petrography

5.1.1 Optical Microscopy and Scanning Electron Microscopy (SEM)

All of the selected samples were used for petrographic studies, which were conducted by optical and electron microscopy at the Natural History Museum of Vienna, and partially at the Karl Franzens University of Graz. Altogether, twenty seven polished and oriented thin sections were produced at the Department of Mineralogy at the Natural History Museum of Vienna and the Department of Lithospheric Research at the University of Vienna. The thin sections were mixed with Aradite AY103-1 and puttied with the hardener HY951. For determining the optical properties an Olympus BX 51 (Model BX51 RFT) microscope was used at the Department of Mineralogy and Petrology of the Karl Franzens University in Graz. The same optical microscope was used for imaging. The carbon-coated samples were examined with JEOL JSM 6410-LV

scanning electron microscope (SEM) at the Department of Mineralogy, Natural History Museum of Vienna in Austria (15 mm working distance, 15 kV, variable spot size depending on the magnification and the required analysis).

5.1.2 Raman Spectroscopy

Raman spectra were obtained with a Renishaw RM1000 confocal edge filter-based micro Raman spectrometer with a 20 mW, 488 nm laser excitation system and a thermoelectrically cooled CCD array detector at the Institute of Mineralogy and Crystallography at the University of Vienna (Vienna, Austria). Spectra were obtained in the range from approximately 40 to 1000 cm, with a 60 s acquisition time.

5.2 Geochemistry

5.2.1 Electron Probe Micro Analysis (EPMA)

Table 2. *The standard materials, crystals, measuring times and detection limits of the EPMA analysis used in this study*

	Crystal	Standard	Counting time [s]		Detection limit [ppm]
			peak	background	
Si	TAP	SiO_2	10	5	139
Al	TAP	Al_2O_3	10	5	120
Cr	LIF	Cr_2O_3	10	5	316
Ti	LIF	TiO_2	10	5	474
K	PETH	KCl	10	5	73
Ca	PETH	Wollastonite	10	5	95
Fe	LIFH	Troilit	10	5	194
Mn	LIFH	Tephroit	10	5	177
Na	TAP	NaCl	10	5	95
Mg	TAP	MgO	10	5	90
Ni	LIFH	NiO	10	5	265

Electron microscopy, including mineral analysis by energy-dispersive spectrometry (EDS) and by wavelength-dispersive spectrometry (WDS), was performed at the Natural History Museum of Vienna using a JEOL JXA 8530-F electron microprobe (EMP) equipped with an EDS and WDS detectors (11.5 mm working distance, 15-20 kV). Spot sizes varied between 10 and 20 µm depending on the magnification and the required analysis. Table 2 displays the used standards, counting times (peak and background), and the spectrometer crystals for calibrations and measurements.

5.2.2 Instrumental Neutron Activation Analysis (INAA)

The abundances of major (Na, K, and Fe) and the majority of the trace elements (including rare earth elements, REEs) were determined by Instrumental Neutron Activation Analysis (INAA) at the Department of Lithospheric Research at the University of Vienna (Mader and Koeberl 2009). The first analyses started in June 2016 on 15 samples that have also been used for petrographical investigations. The drill core samples were powdered with a vibrating swing mill (RS200) with a milling set made of agate. Between 120 and 140 mg of these samples and about 60 mg of three international standards (the carbonaceous chondrite Allende, Smithsonian Institution, Washington DC, USA, Jarosewich et al. 1987; the Ailsa Craig Granite AC-E, Centre de Recherche Petrographique et Geochimique, Nancy, France; Govindaraju 1989; and the Devonian Ohio Shale SDO-1, United States Geological Survey; Govindaraju 1989) were sealed in polyethylene capsules, and subsequently, irradiated in the 250 kW Triga Mark-II reactor at the Atomic Institute of the Austrian Universities. After an about five day cooling period, the measurements were started, and subsequently, conducted in three cycles. The measurement of the short-lived isotopes, were carried out in the first cycle (L1) starting about five days after the irradiation. In this cycle, every sample is measured for about 40 to 60 minutes. In the second cycle (L2), which starts about 10 days after irradiation, the samples are measured for 3 hours. When the majority of the short-lived isotopes have decayed, the third and last cycle (L3) starts. This is about 5 weeks after the irradiation. In this cycle, the samples are analyzed for about 24 hours. Subsequently, the resulting spectra are calibrated and then calculated based on the comparison between the samples and the standards. The peaks from each element that resulted from different cycles, are eventually compared and corrected. Element concentrations are calculated as a mean value of the fitting peaks.

CHAPTER 6

Results

6.1. General Description of the Drill Core Section

The studied drill core section ranges in depth from 311.467 to 317.38 mblf (meters below lake floor). This particular drill core section contains a total of 98 samples that were originally recovered in 2009 and subsequently stored at the LacCore Facility at the University of Minnesota. Raschke et al. (2013) classified the zone between 313.73 and 316.77 mblf as the transition zone which varies slightly from the core sections that have been investigated in this work. Here, we consider the drill core section between 311.467 and 317.38 mblf as the transition zone. The Transition Zone lies between the lowermost true lake sediment and the uppermost reworked suevite. The first macroscopic observations were conducted in October 2015 at the Natural History Museum in Vienna. Based on this first macroscopic analysis, 15 samples were selected as representative of the whole section for further scientific investigations. The El'gygytgyn transition zone comprises a mixture of about six meters of loose sedimentary and volcanic material from the target rock hosting isolated clasts between the lowermost lacustrine lake sediments and uppermost reworked suevite. The first macroscopic observations of this section yielded isolated clasts embedded in lacustrine sediment on top, underlain by a greywacke-like sediment with fine- to coarse-grained sand clasts (middle of the 97Q-1 core section). A small fine-grained laminated silt to sand zone separates the greywacke-like sediment from a coarser-grained sediment hosting lithic clasts up to 1 cm in size (end of 97Q-1). Below, a large clast of possible impact breccia which is embedded in fine-grained sand layers was recovered (top of 97Q-2) (Raschke et al. 2013). The clasts are embedded in fine- to coarse-grained sand layers clast size and frequency of clasts increase downwards. Overall the samples are heavily altered. Visible off-white, needle-like crystals partially coat the surface and fill cavities and gaps.

6.2. Petrography

All samples are of low coherence and, therefore, had to be embedded in epoxy in order to produce thin sections. At first 17 polished thin sections were prepared at the Natural History Museum in Vienna. These comprise 15 samples of the drill core (Fig. 10 and Fig. 11). There have been two samples where additional thin sections were prepared. After a superficial overview of

the already existing thin sections some were selected to produce ten further polished thin sections that were prepared at the Department of Lithospheric Research at the University of Vienna. Due to the difficulties in preparation, these were prepared as coverslips and used just for optical observations.

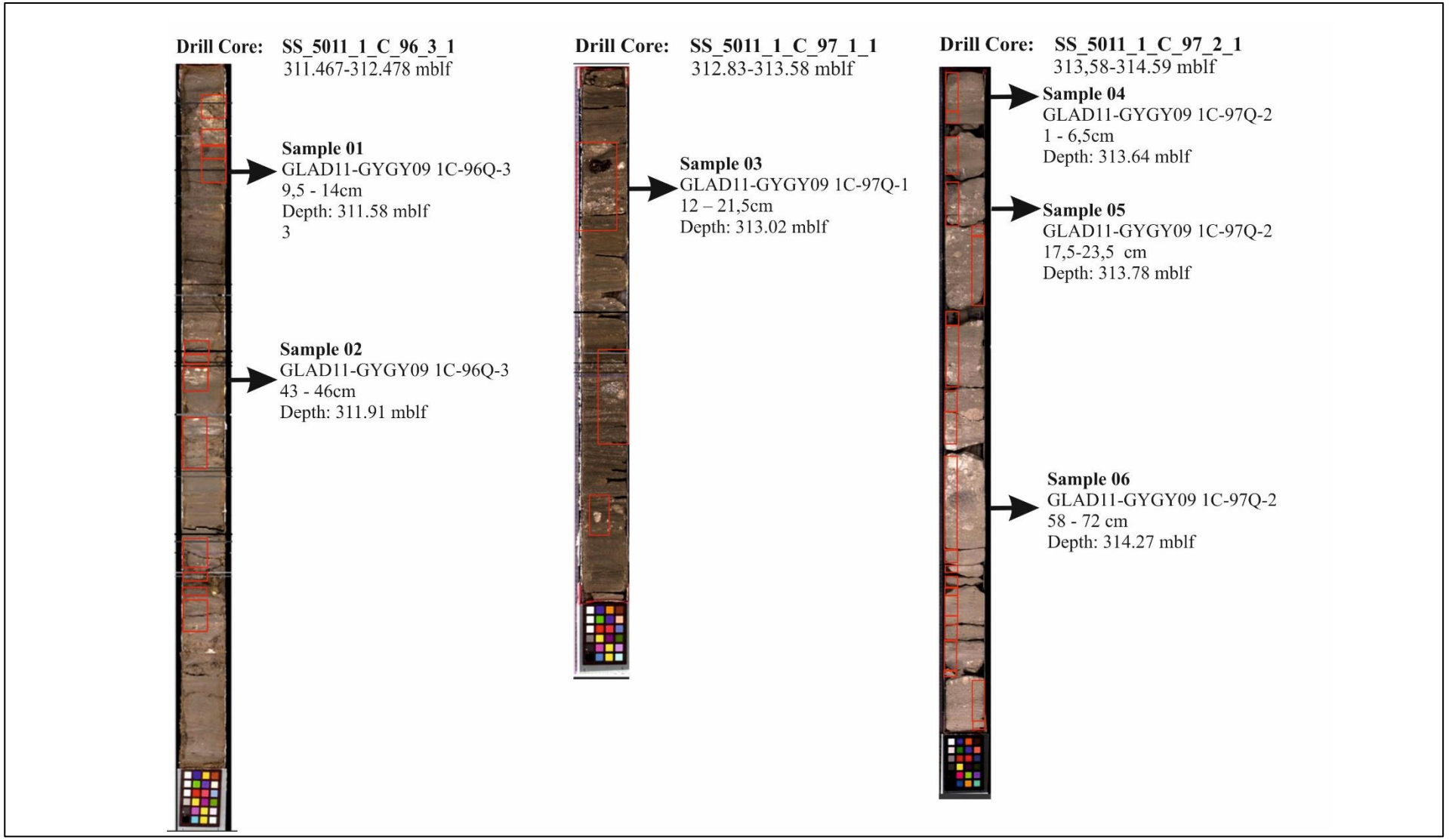

Fig. 10. *Photographs of the drill core sections from 311.467 to 314.59 meters below lake floor (mblf) where representative samples for thin section preparation have been selected. The red squares represent all the extracted rock samples.*

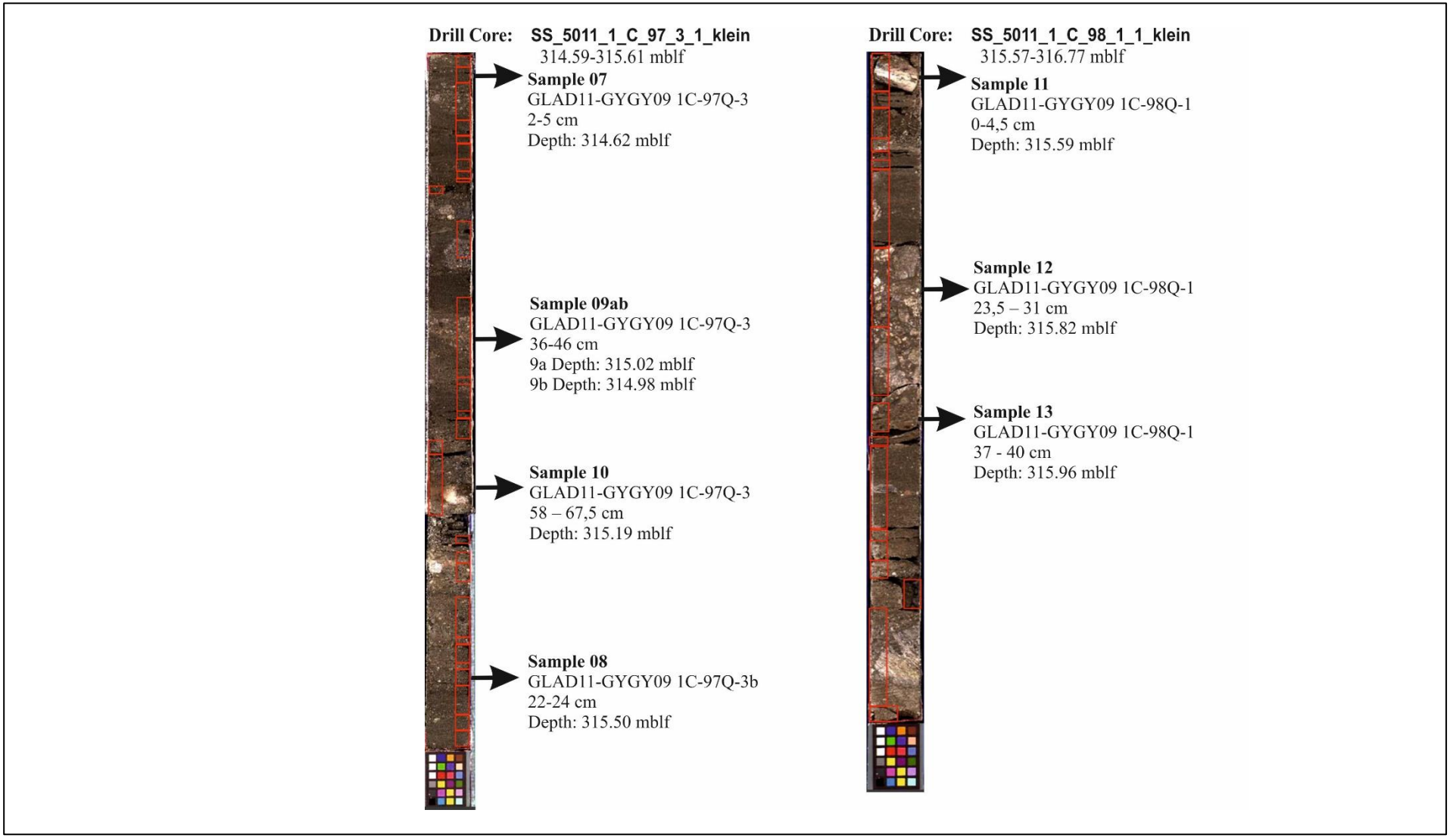

Fig. 11. *The drill core sections from 314.59 to 316.77 meters below lake floor (mblf). Thin sections were prepared of samples 07 to 13 for petrographic investigations. Samples 14 (316.93 mblf) and 15a and b (317 and 317.07, respectively) are part of Drill Core GLAD-GYGY-1C-98Q-2 (from 316.77 to 317.38 mblf), which is not in this photo-documentation.*

6.2.1. Petrography of the Rocks from the Drill Core Section

Under the optical microscope in transmitted light, all samples exhibit an agglomeration of non-shocked and shocked particles and can be classified as suevites, with intercalations of fine-grained lacustrine sediments. Shocked minerals, that are 50-100 μm in size, occur in every sample and mostly consist of individual quartz clasts containing planar features (PFs) and planar deformation features (PDFs). There is no section of the drill core that exhibits an accumulation of shocked quartz grains with PDFs. Other impact related features include silica diaplectic glass, hosting coesite, kinked micas and amphibole, lechatelierite and microtektite-like spherules. Numerous glass shards and different melt fragments whose distinction from volcanic and impact origin represents a major challenge can be observed. The size and number of the melt fragments increase as well downwards in the core. PDFs in quartz grains occur in samples near the lacustrine sediments. Spherules, silica diaplectic glass, and lechatelierite, however, appear about one meter below the top of the onset of the transition zone, marking the possible beginning of the more coherent impact ejecta deposits.

At the beginning of the transition zone at 313.73 mblf the impact breccia appears fine-grained and matrix supported. The first centimeters exhibit a layering caused by a difference in grain sizes. Clasts within this sequence show no preferential orientation. Hence, fine-grained layers alternate with coarser-grained ones. Further down in the drill core (about 15-20 cm) the fine-grained sections host irregular centimeter-sized tuff fragments varying in color from white to dark grey/black (NHM thin section 3). These clasts exhibit a highly vesicular texture. These vesicles are filled with secondary OH-bearing phases rich in Si, Al, K, Na, and Ca which exhibit spherulitic growth. These secondary phases are most likely phillispsite and/or chabazite (Chipera and Apps 2011) and occur all over the samples being dominant in matrix voids. Below, at about 313.64 mblf, a dominant centimeter-sized volcanic clast separates the sequence described above from a sequence that is clast-supported and significantly coarser-grained (NHM thin section 4). This highly vesicular clast hosts altered pyroxene crystals displaying a dominant dark greenish intrinsic color under the optical microscope. Further down the drill core, grain size and the abundance of tuff and/or volcanic fragments remain constant. There is no significant change in grain size, frequency of melt and lithic fragments, or mineralogy.

The general mineralogy of all samples under the optical microscope in transmitted light consists of feldspar, quartz, carbonate, biotite, amphibole, pyroxene (Ca-Mg pyroxene – augite), chlorite, apatite, rutile, zircon, sphene, and opaque phases such as pyrite and Fe-oxide. Rutile and zircon appear rarely and, therefore, are accessory minerals. Secondary minerals which represent mainly alteration products are distributed in small quantities all over the sections. These comprise chlorite, glauconite, carbonate, and a Si-Al-OH-rich phase that mostly fills the voids that might be zeolite. Generally, an advanced sericitization (especially on feldspar grains) and a moderate carbonatization can be observed.

6.2.1.1 Matrix

Depending on the depth of the transition layer, the matrix varies slightly in abundance and grain-size, but the composition remains constant. In general, the matrix constitutes most of the rock and exhibits a hypocrystalline texture (Fig. 12a). Quartz, feldspar, and glass constitute the groundmass appearing as crushed material. Also secondary alteration products such as carbonate, clay minerals, and Na-K-Ca aluminosilicates occur frequently. Individual grains of quartz and feldspar that are subhedral to anhedral reach sizes from 10 to 20 µm.

Fe-oxide, rutile, apatite, calcite, and chlorite occur to a lesser extent. Calcite forms single, mostly euhedral, phases evenly distributed in the matrix and occurs also as alterations products. The latter form of calcite is recrystallized forming small granular aggregates replacing parts of feldspar grains and filling previous voids. Matrix material also occurs as vesicle filling (Fig. 12b).

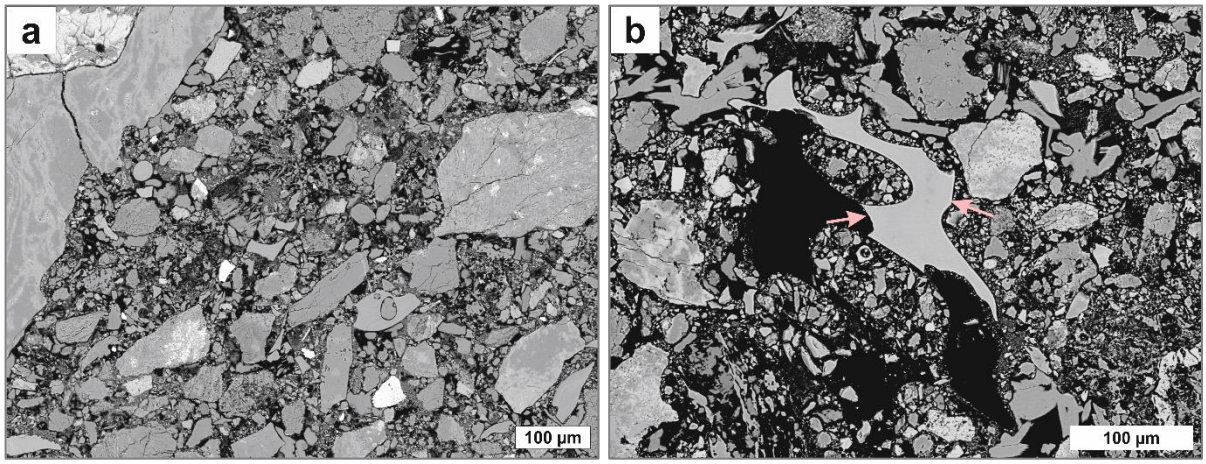

Fig. 12 a) *Suevite showing matrix and mineral as well as melt clasts of different size (Sample 15b, BSE-EM image).* ***b)*** *Section of the suevite that exhibits matrix material in vesicles associated with melt and mineral clasts. Note the melt shard in the middle (pink arrows). (Sample 15b, 317.07 mblf, BSE-EM image).*

6.2.1.2 Mineral Clasts

6.2.1.2.1 Quartz

Quartz clasts vary in size from about 100 to 200 µm and are common in the suevite. They exhibit various stages of shock metamorphism. Most quartz grains which are sub- to anhedral in shape and show no signs of shock (Fig 13a). Some of those are associated with feldspar. Most of those grains show indications of a flow fabric or exhibit a patchy appearance with varying compositions sometimes even hosting crystallized areas that show definite feldspar or quartz chemistries. The quartz grain in Figs. 13b and 13c seems to have been locally vesiculated. Quartz grains are generally fractured and are filled with clay minerals. The light areas in the BSE-image (SEM) in Fig. 13c and d, are of different chemistry and could be the original groundmass of an ignimbrite containing this large quartz phenocryst.

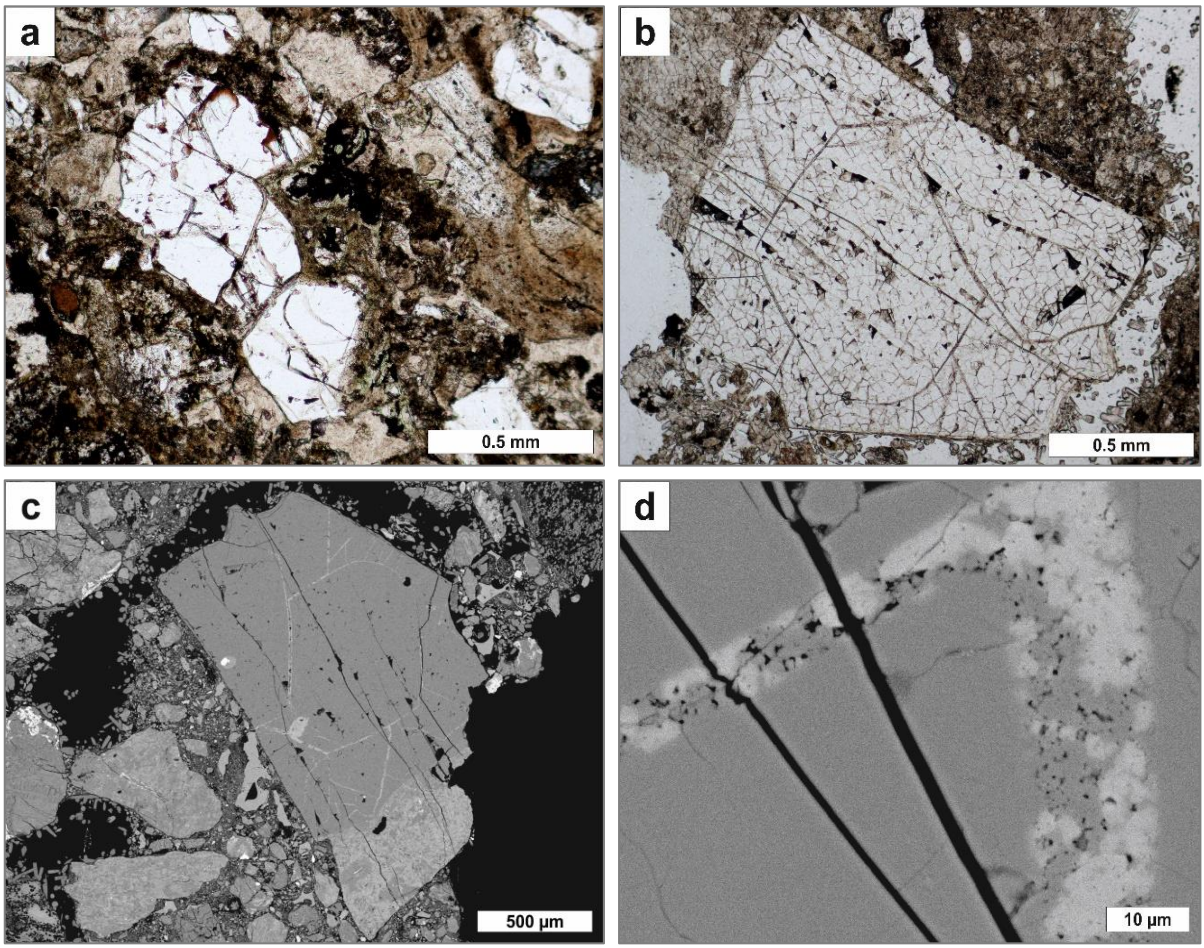

Fig. 13. a) *Fractured quartz grain under plane-polarized light. Sample 11 09, 315.59 mblf.* ***b)*** *Large quartz grain that seems to have been vesiculated. Optical microscopy, plane-polarized light. Sample 14 01, 316.93 mblf.* ***c)*** *The same grain rotated in an about 180° angle. Note the difference in chemistries in the cracks and on the bottom right. These areas are hydrated and enriched in K and Si leading to the assumption that these bright spots are clay mineral alterations. BSE-SEM image* ***d)*** *The same grain at higher magnification. BSE-SEM image.*

Sporadically, quartz grains with PF and PDF occur (Figs. 14). They show at least 4 and a maximum of 6 sets of PDF orientations. All of the observed PDFs are non-decorated. Most of those shocked grains range from 100 to 200 µm in size. Some grains exhibit special PDF characteristics. The PDFs seem to have been deformed locally forming about 1 to10 µm broad open lamellae along shear zones in the crystal. The rest of the grain contains fewer PDFs (Figs. 14c and 14e). Shocked quartz grains exhibiting PDFs can be observed throughout the whole section of the transition layer.

Besides PDFs further shock features in quartz grains include silica diaplectic glass (Figs. 15a-f). These features have been observed just twice over all prepared thin sections of the transition layer. Both of those silica diaplectic glass clasts are about 500 µm long and wide yielding intergrowths of coesite and quartz (Figs. 15). The coesite segregations exhibit vermicular shapes, and are surrounded by quartz glass. The quartz grains within the diaplectic glass in comparison, show a higher relief and also occur in vemicular and granular shapes.

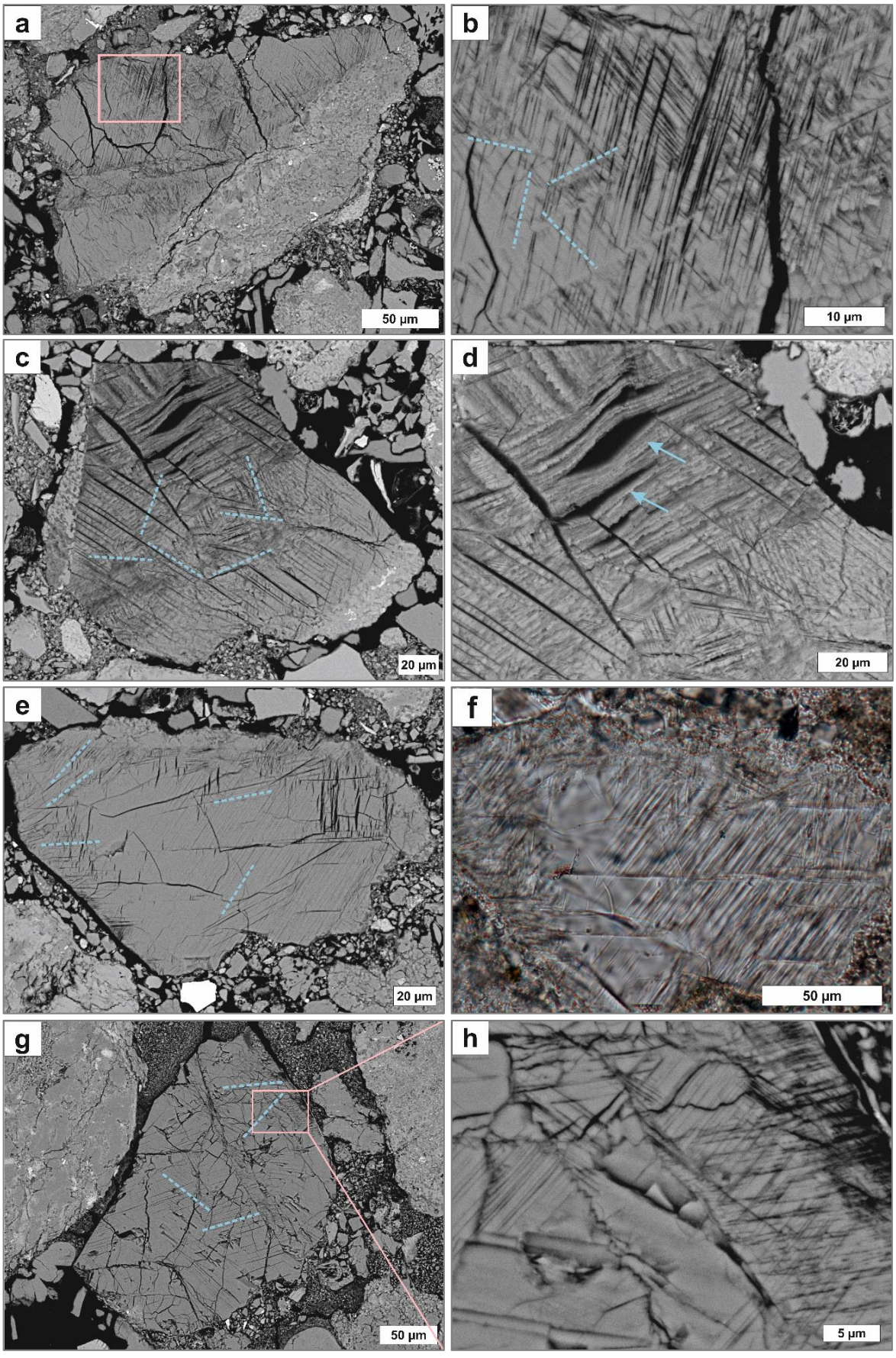
a
50 µm
b
10 µm
c
20 µm
d
20 µm
e
20 µm
f
50 µm
g
50 µm
h
5 µm

← ***Fig. 14. a)*** *Quartz grain with 4 sets of PDFs (dashed blue lines at b). Sample 15b 18, 317.07 mblf. BSE-SEM image.* ***b)*** *The same grain at higher magnification. BSE-SEM image.* ***c)*** *Highly shocked quartz grain with pervasive development of PDFs. There are at least 6 locally deformed sets of PDFs (dashed blue lines). Sample 14 12, 316.93 mblf. BSE-SEM image.* ***d)*** *The same grain at higher magnification. Note the open shear fractures (blue arrows). BSE-SEM image.* ***e)*** *Quartz grain with at least 5 sets of PDFs (dashed blue lines) that are locally deformed showing open shear fractures. Sample 14 07, 316.93 mblf. BSE-SEM image.* ***f)*** *The same grain under plane-polarized light, optical microscopy.* ***g)*** *Shocked quartz grain exhibiting at least 4 sets of PDFs (dashed blue lines). Sample 9a 11, 315.02 mblf. BSE-SEM image.* ***h)*** *The same grain at larger magnification. BSE-SEM image.*

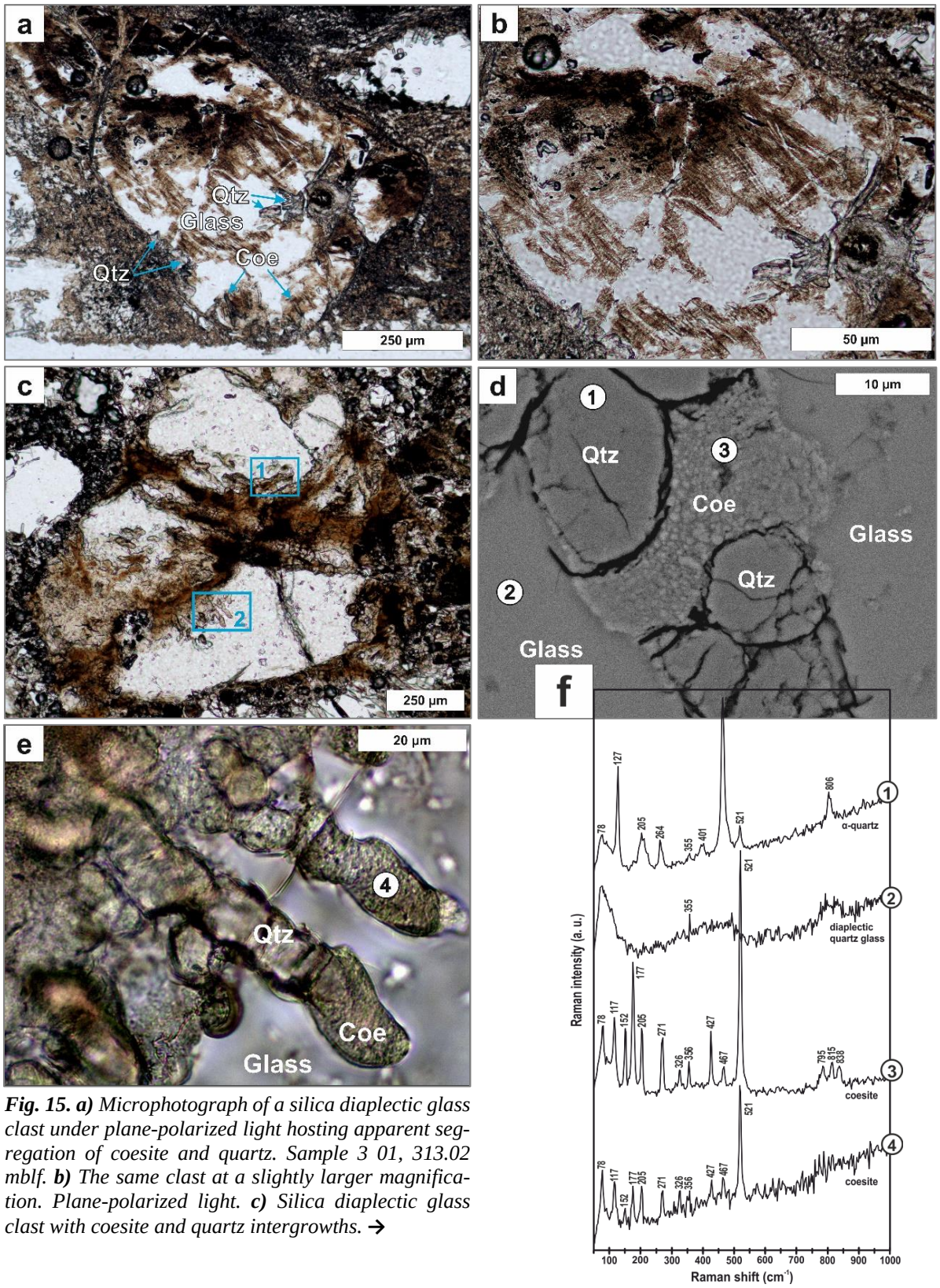

Fig. 15. a) *Microphotograph of a silica diaplectic glass clast under plane-polarized light hosting apparent segregation of coesite and quartz. Sample 3 01, 313.02 mblf.* ***b)*** *The same clast at a slightly larger magnification. Plane-polarized light.* ***c)*** *Silica diaplectic glass clast with coesite and quartz intergrowths.* →

→ *Frame 1 refers to d) and Frame 2 refers to e). Sample 9a 08, 315.02 mblf.* ***d)*** *BSE-SEM image of the same grain which refers to frame 1 at c). It clearly displays the coesite and quartz segregations.* ***e)*** *Microphotograph under plane-polarized light showing coesite and quartz intergrowths at a higher magnification.* ***f)*** *Raman spectra of the 4 measured spots in d) and e).*

6.2.1.2.2 Feldspar

Feldspar is by far the most common mineral and appears in various sizes and shapes, alteration stages, and compositions. It occurs as single, 10 to 20 µm small, grains as part of the matrix as well as phenocrysts and/or xenocrysts in different lithic/volcanic and melt fragments and as individual clasts in the rock.

The majority of the feldspars have sizes ranging from 100 to 200 µm and are strongly altered, showing replacement by Ca-carbonate and clay minerals. Altered feldspar grains mostly exhibit irregular anhedral to subhedral shapes (Fig. 16a-2), whereas seemingly fresh feldspar shows mostly subhedral, rarely euhedral crystal shapes (Fig. 16a-3). Regardless of their alteration, the most common type of feldspar is untwinned. However, there are clasts of twinned plagioclase that seem to have been fragmented (Figs. 16e and f).

Chemically, the most abundant feldspar is alkali-feldspar (Table 3). The majority of the feldspar clasts are pure Na- and K-feldspar endmembers, as well as their solid solutions (Fig. 17). Alkali-feldspar compositions range from Ab_{02} to Ab_{99}. Feldspar compositions have been calculated based on 8 oxygens and 5 cations. Fe_2O_3 was recalculated based on stoichiometry and charge balance.

In most cases feldspar clasts that occur in lithic/volcanic fragments are anhedral to subhedral in grain shape. Fragments host clearly discernible plagioclase laths (10-100 µm in length) that are twinned and composite most of the fragment exhibiting a subophitic texture (Figs. 28 a-e). Some lithic fragments host strongly altered feldspar clasts wherefore their original chemistry and grain shape is difficult to determine. Rarely, fragments that exhibit partially molten textures occur. In such fragments feldspar has already been molten and encloses grains that are still intact. This melt structures show segregations that resulted in a flow fabric with schlieren (Figs. 28 f-h) Chemical analyses yield K-feldspar compositions for the leucosomes and Na-feldspar compositions for the melanosomes.

Shock effects in feldspar, such as PF and PDFs, have been documented from other researches from the El'gygytgyn samples, especially in alkali feldspar. For the investigated samples from the transition layer, no such effects have been observed.

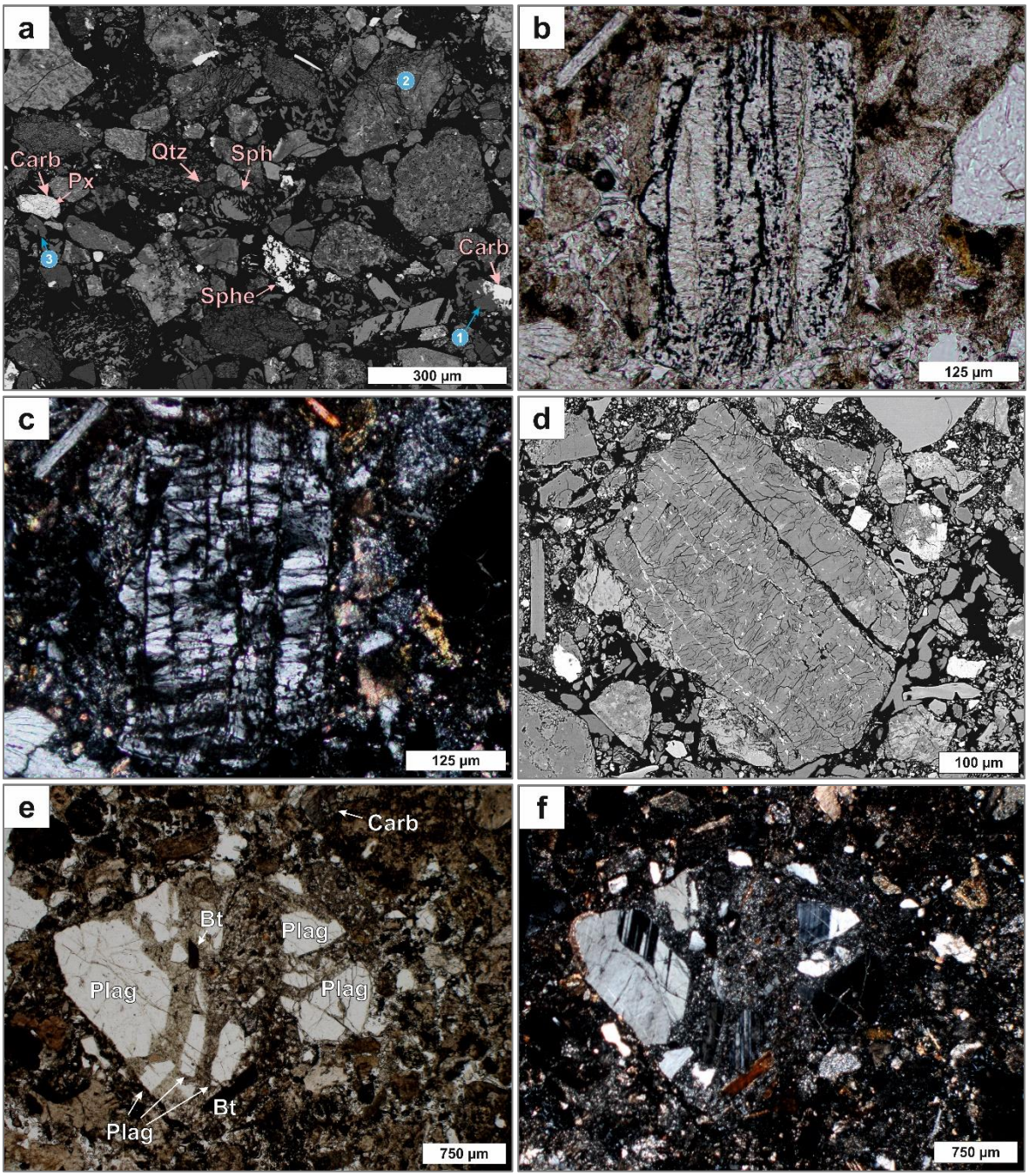

Fig. 16. a) *BSE-EM overview of the suevite including different feldspar clasts which compositions had been determined. Circle (C) 1 describes a grain that is half Na-feldspar and half Ca-Carbonate (bright area). C 2 shows an altered feldspar grain. Seemingly unaltered spots reveal Na-feldspar compositions. C 3 represents an unaltered subhedral alkali-feldspar clast that also yields Na-feldspar compositions. These feldspar clasts that have also been chemically analyzed (Table 1., C1:9a_10_09, C2:9a_10_8, C3:9a_10_04). Sample 9a_10, 315.02 mblf. Sphe = sphene, Sph = spherule, Px = pyroxene, Carb = Ca-carbonate.* ***b)*** *Microphotograph under plane-polarized light (optical microscopy) of a fractured Na-feldspar clast that exhibits massive alterations. Sample 14 02, 316.93 mblf.* ***c)*** *The same clast under crossed-polarized light.* ***d)*** *BSE-EM image of the same grain. Light areas within the clast represent clay mineral alterations Note the fracture pattern.* ***e)*** *Microphotograph of a possible fractured large plagioclase crystal that currently consists of various plagioclase clasts. The interstices are filled with material that are probably derived from the matrix. Note the biotite (Bt) sheets. Plane-polarized light, optical microscopy. Sample 8 14, 315.50 mblf.* ***f)*** *The same image under crossed-polarized light illustrating the twinned plagioclase fragments. The twins that are not separated.*

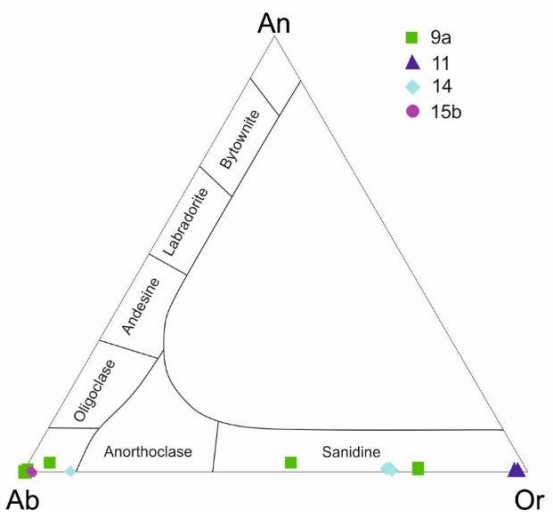

← ***Fig. 17.*** *Ternary classification diagram Ab-An-Or for feldspars displaying the chemical variability of the feldspar clasts in the suevite. Note that all measured clasts can be classified as alkali-feldspars.*

Table 3. *Major element analyses (in wt%) of selected alkali-feldspar clasts. The depth is expressed as meters below lake floor (mblf). Fe_2O_3 was recalculated based on stoichiometry and charge balance. An= Anorthite, An = Albite, Or = Orthoclase.*

Sample	***9a***	***9a***	***9a***	***9a***	***11***	***11***	***14***	***15b***
Point	3_08	10_04	10_08	10_09	9_04	9_05	20_03	2_06
Classification	Albite	Albite	Albite	Albite	Ortho-clase	Ortho-clase	Sanidine	Albite
Grain size [µm]	50	120	250	150	>250	>250	200	100
Depth [mblf]	315.02	315.02	315.02	315.02	315.59	315.59	316.93	317.07
SiO_2	68.97	67.89	68.89	68.61	63.79	65.02	66.10	69.33
TiO_2	<0.08	<0.08	<0.08	<0.08	<0.08	<0.08	<0.08	<0.08
Al_2O_3	18.95	20.28	19.46	19.25	19.34	18.49	18.23	19.32
Cr_2O_3	<0.02	<0.02	<0.02	<0.02	0.09	0.04	0.03	<0.02
Fe_2O_3	<0.006	0.17	<0.006	<0.006	<0.006	<0.006	<0.006	<0.006
FeO	0.22	<0.02	0.03	0.13	<0.02	0.04	0.11	0.09
CaO	0.15	0.40	0.18	0.22	<0.01	<0.01	0.12	0.03
Na_2O	11.66	11.15	11.64	11.63	0.20	0.28	3.12	11.31
K_2O	0.12	0.72	0.08	0.09	15.83	15.90	11.66	0.26
Total	100.13	100.60	100.35	99.93	99.28	99.76	99.38	100.33
Calculations based on 8 oxygens and 5 cations								
Si	3.01	2.95	3.00	3.00	2.97	3.02	3.04	3.03
Ti	0.00	0.00	0.002	0.00	0.00	0.00	0.00	0.00
Al	0.98	1.04	1.00	0.99	1.06	1.01	0.99	0.99
Cr	0.00	0.00	0.00	0.00	0.00	0.00	0.00	0.00
Fe^{3+}	0.00	0.01	0.00	0.00	0.00	0.00	0.00	0.00
Fe^{2+}	0.01	0.00	0.00	0.00	0.00	0.00	0.00	0.00
Ca	0.01	0.02	0.01	0.01	0.00	0.00	0.01	0.00
Na	0.99	0.94	0.98	0.99	0.02	0.02	0.28	0.96
K	0.01	0.04	0.00	0.00	0.94	0.94	0.68	0.01
Total	5.00	5.00	5.00	5.00	5.00	5.00	5.00	5.00
An	0.71	1.86	0.85	1.02	0.00	0.00	0.62	0.14
Ab	98.65	94.14	98.71	98.48	1.84	2.58	28.70	98.39
Or	0.64	4.00	0.44	0.50	98.16	97.42	70.68	1.47

6.2.1.2.3 Carbonate

Carbonate is represented as Ca-carbonate, most likely calcite, and occurs as two different types. The first type forms individual clasts in the suevite that appear mostly subhedral in shape (Fig. 18a). The second population is represented by secondary alteration. Many alkali-feldspar grains and pyroxene grains are partially replaced by Ca-carbonate (see Fig. 16a C1). Figures 19a and b show a mineral structure that has been partially replaced by granular Ca-carbonate grains (Carb), associated with rutile (Ru) and apatite. Some voids and vesicles show fillings consisting of the same aggregate. These secondary Ca-carbonates are strongly anhedral and appear in a granular texture. Chemically, all analyzed carbonates yield CaO contents ranging from 51.46 to 55.60 wt% which suggests that the Ca-carbonate present in this sample exclusively consists of calcite.

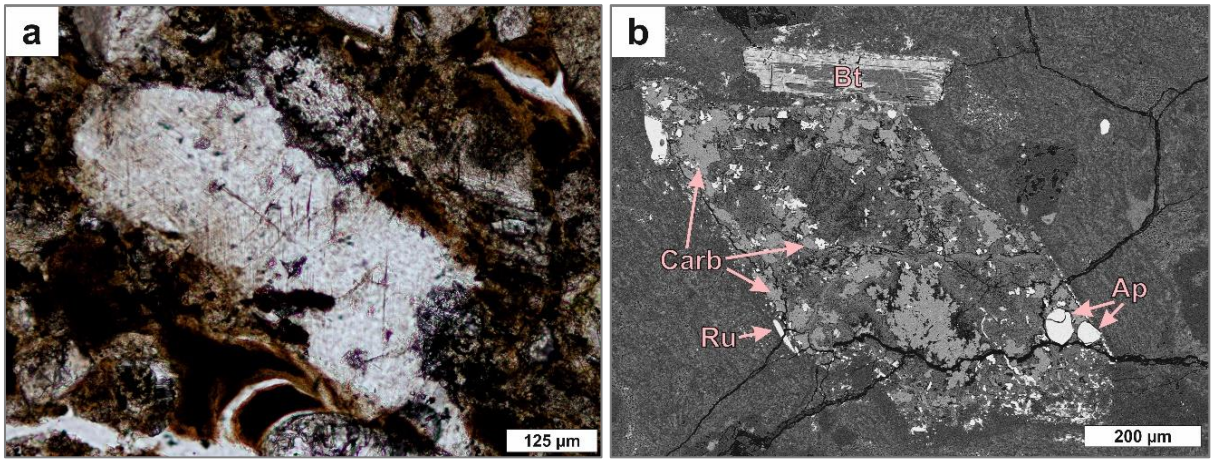

Fig. 18. a) *Microphotograph under plane-polarized light of a Ca-carbonate, calcite, clast within the suevite. Optical microscopy. Sample 11 04, 315.59 mblf.* ***b)*** *BSE-SEM image showing a replacement by granular Ca-carbonate. Note the large altered biotite (Bt) above. Ru = rutile, Ap = apatite. Sample 11 03, 315.59 mblf.*

6.2.1.2.4 Pyroxene

All analyzed pyroxene clasts can be classified as augite. Figure 20 displays the nomenclature, after Morimoto (1988), which is used to describe the analyzed pyroxenes. The compositions are spread between the augite and the diopside domains. Most of the augites are a 100 µm in size and occur as single mostly euhedral crystals within the suevite (Figs. 20 a-d). Sporadically, they are a part of volcanic fragments, but these grains show strong alterations especially at their edges (Figs. 20e and f) and are bigger in size (≤ 750 µm). The volcanic fragment, more specifically, a tuff fragment, in Figs. 20e and f hosting the augite pheno- or xenocrysts is strongly vesicular. However, the alterations are not just restricted to pyroxenes within volcanic fragments. There are also altered single pyroxene clasts within the suevite. Such grains are mostly dominated by Ca-carbonate replacement. So far, no shock effects in these pyroxenes have been discovered.

The structural formula can be expressed as $M2M1T_2O_6$ or including the charge of the cations as $M2(R^{2+})$ $M1(R^{3+})$ $T(2\ R^{4+})$ O_6, where M2 and M1 refer to the cations in octahedral coordination and T to tetrahedrally coordinated cations.

Representative pyroxene analyses are given in Table 4. These are calculated on the basis of 6 oxygens and 4 cations. Due to the fact that microprobe analyses consider all iron initially as Fe^{2+}, Fe^{3+} had to be calculated using the Droop-Method. Fe_2O_3 in the pyroxene was then calculated as follows $Fe^{3+} = Al^{IV} + Na - Al^{VI} - Cr - 2*Ti$.

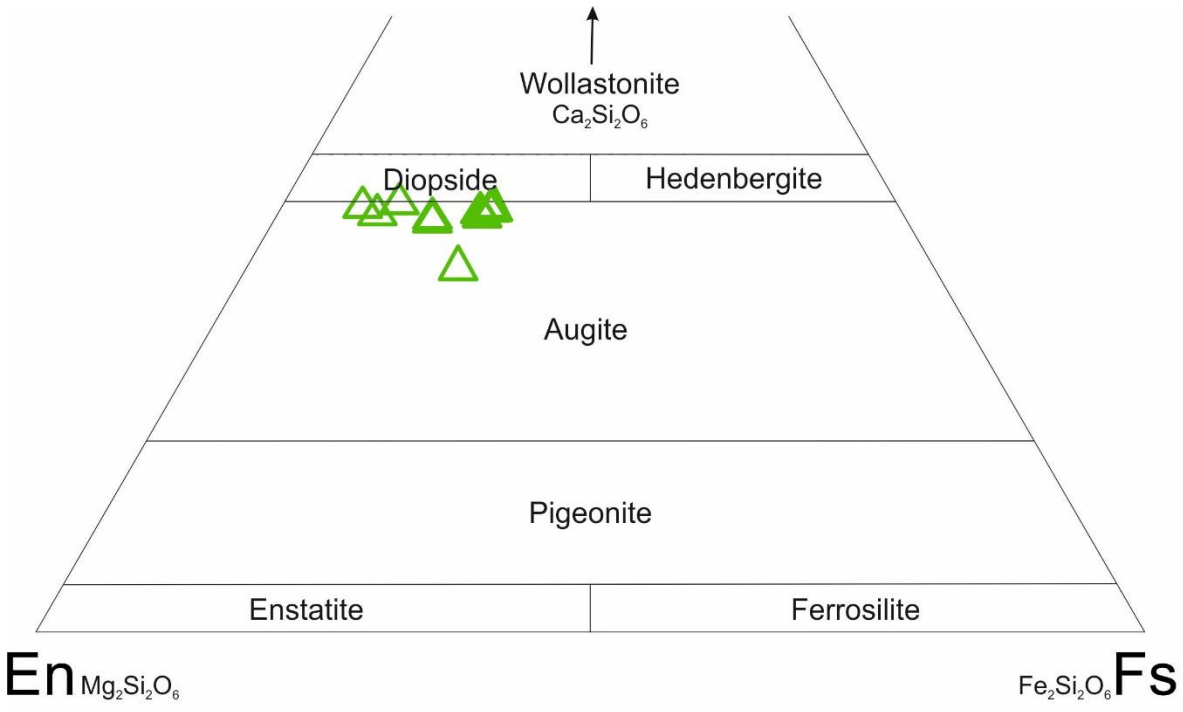

Fig. 19. *Nomenclature describing the analyzed pyroxenes after Morimoto (1988). All measured clasts plot in the augite field with the tendency to approach the diopside section.*

Table 4. *Representative chemical compositions of pyroxene in wt%. Crystal chemical calculations are based on 6 oxygens and 4 cations. Fe^{2+} and Fe^{3+} were calculated using the Droop-Method. Fe_2O_3 respectively was calculated as follows: $Fe^{3+} = Al^{IV} + Na - Al^{VI} - Cr - 2*Ti$.*

Sample	***9a***	***9a***	***9a***	***9a***	***15b***	***15b***	***15b***
Point	3_02	10_03	Px8	Px9	14_01	14_03	23_02
Grain size [µm]	210	200	120	120	140	140	240
Depth [mblf]	315.02	315.02	315.02	315.02	317.07	317.07	317.07
SiO_2	52.46	50.42	51.21	50.66	53.12	52.85	53.14
TiO_2	<0.08	0.77	0.45	0.70	0.19	0.17	0.10
Al_2O_3	0.87	5.22	2.66	2.19	0.81	0.90	0.91
Cr_2O_3	0.03	0.70	0.91	<0.02	<0.02	0.10	0.05
MnO	0.50	0.13	0.11	0.45	0.43	0.54	0.49
MgO	12.62	15.25	17.30	15.09	13.07	12.82	13.18
CaO	21.29	21.12	22.03	21.29	21.34	21.23	21.26
Na_2O	0.31	0.26	0.25	0.39	0.26	0.26	0.29
FeO	11.05	5.39	1.93	5.67	10.65	10.97	10.78
Fe_2O_3	0.11	0.79	2.97	3.02	n.m.	n.m.	n.m.
Total	99.29	100.05	99.81	99.45	99.87	99.83	100.20
Calculations based on 6 oxygens and 4 cations							
Si	1.99	1.85	1.88	1.89	1.99	1.99	1.99
Ti	0.00	0.02	0.01	0.02	0.00	0.00	0.00
Al	0.04	0.23	0.12	0.10	0.04	0.04	0.04
Cr	0.00	0.02	0.03	0.00	0.00	0.00	0.00
Mn	0.01	0.00	0.00	0.01	0.01	0.01	0.01
Mg	0.71	0.84	0.95	0.84	0.73	0.72	0.74
Ca	0.86	0.83	0.87	0.85	0.86	0.86	0.85
Na	0.02	0.02	0.02	0.03	0.02	0.02	0.02
Fe^{3+}	0.00	0.02	0.08	0.08	n.m.	n.m.	n.m.
Fe^{2+}	0.35	0.17	0.06	0.18	0.33	0.35	0.34
Total	4.00	4.00	4.01	4.01	3.99	3.99	4.00
X_{Fe}^{2+}	0.33	0.17	0.06	0.17	0.31	0.32	0.31
Al^{IV}	0.01	0.14	0.11	0.09	0.00	0.01	0.01
Al^{VI}	0.03	0.08	0.00	0.00	0.03	0.03	0.03
Tetr	2.00	2.00	1.99	1.99	2.00	2.00	2.00
Octa	1.11	1.15	1.13	1.14	1.11	1.12	1.12
M2 site	1.00	1.00	1.01	1.02	0.99	0.99	1.00

n.m. = not measured; Oxides in wt%; All samples analyzed by EPMA; $X_{Fe}^{2+} = Fe^{2+}/Fe^{2+}+Mg$; Al^{IV} = tetrahedrally coordinated aluminium; Al^{VI} = octahedrally coordinated aluminium; Tetr = tetrahedral sites, Octa = octahedral sites; M2 site = cations (2+) in octahedral coordination.

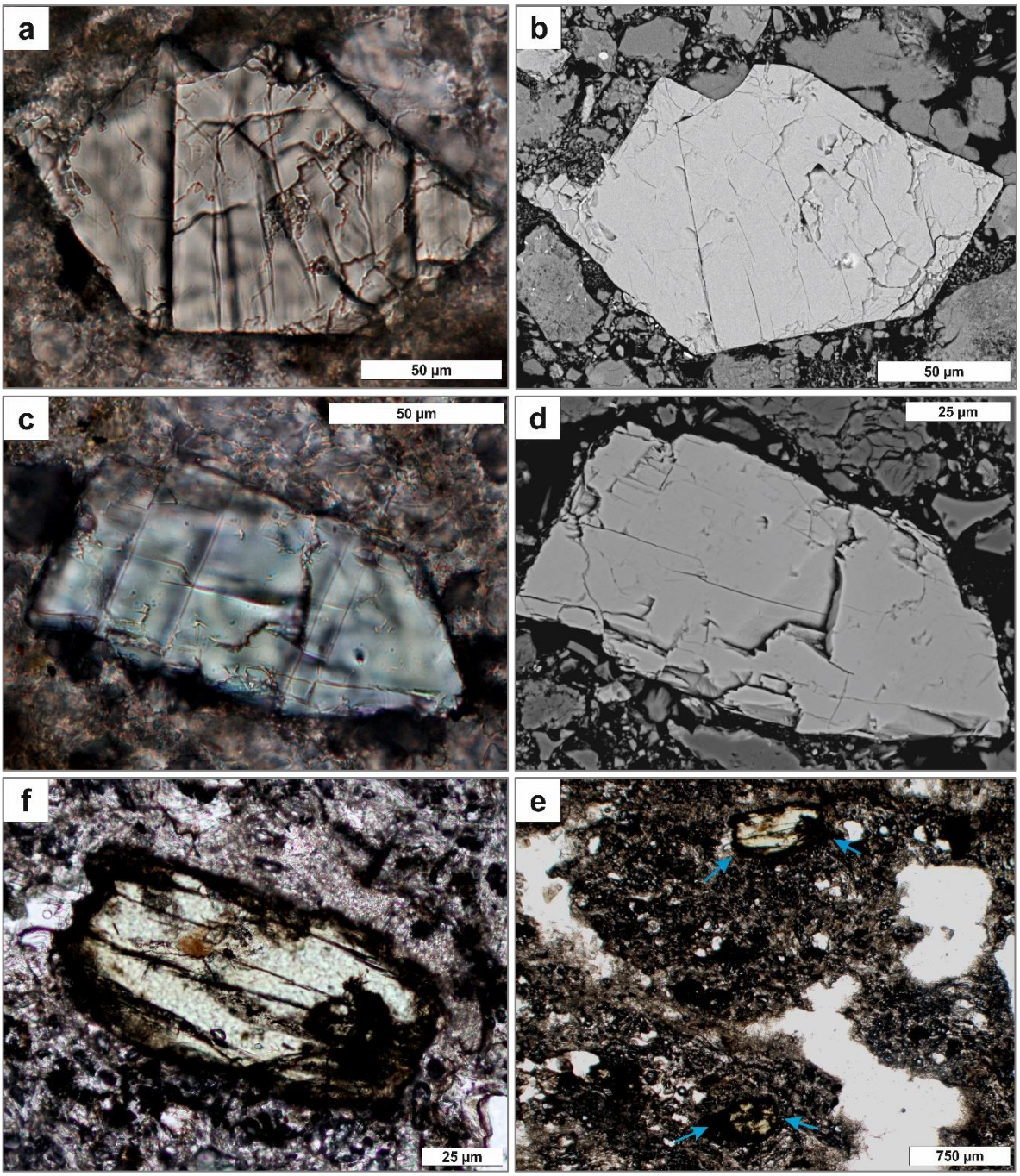

Fig. 20. a) *Microphotograph of an augite crystal under plane-polarized light. Sample 9a 04, 315.02 mblf.* ***b)*** *BSE-SEM image of the same crystal.* ***c)*** *Augite grain with a visible greenish to blueish intrinsic color. Plane-polarized light, optical microscopy. Sample 15b 14, 317.07 mblf.* ***d)*** *The same grain. BSE-EM image.* ***e)*** *Tuff fragment with pheno- or xenocrysts of augite (blue arrows). Note the significant greenish intrinsic color. Plane-polarized light, optical microscopy. Sample 5 07, 313.78 mblf.* ***f)*** *The same image under higher magnification displaying the augite grain above. Note the peripheral alteration to Fe-oxides.*

6.2.1.2.5 Amphibole

Amphibole occurs infrequently as single clasts within the suevite and as resorbed residuals within lithic fragments. They are clearly recognizable due to their greenish intrinsic color and their specific intersecting cleavage planes (124° and 56°) (Figs. 21a and 21b). The large an- to subhedral clasts reach sizes up to 1 mm illustrating their rhombic basal section (Fig. 21c). Under the optical microscope, using crossed-polarized light, they also exhibit a strong pleochroism from orange to pink (Fig. 21b). Most amphibole clasts are significantly altered at their edges, mostly to Fe-oxide. Some grains show replacement by biotite and chlorite. Occasionally, kinked amphibole occurs (Fig. 21d). Enclaves of Ca-carbonate, which is most likely calcite (about 50 µm in length), and apatite (Fig. 21c) are conspicuous.

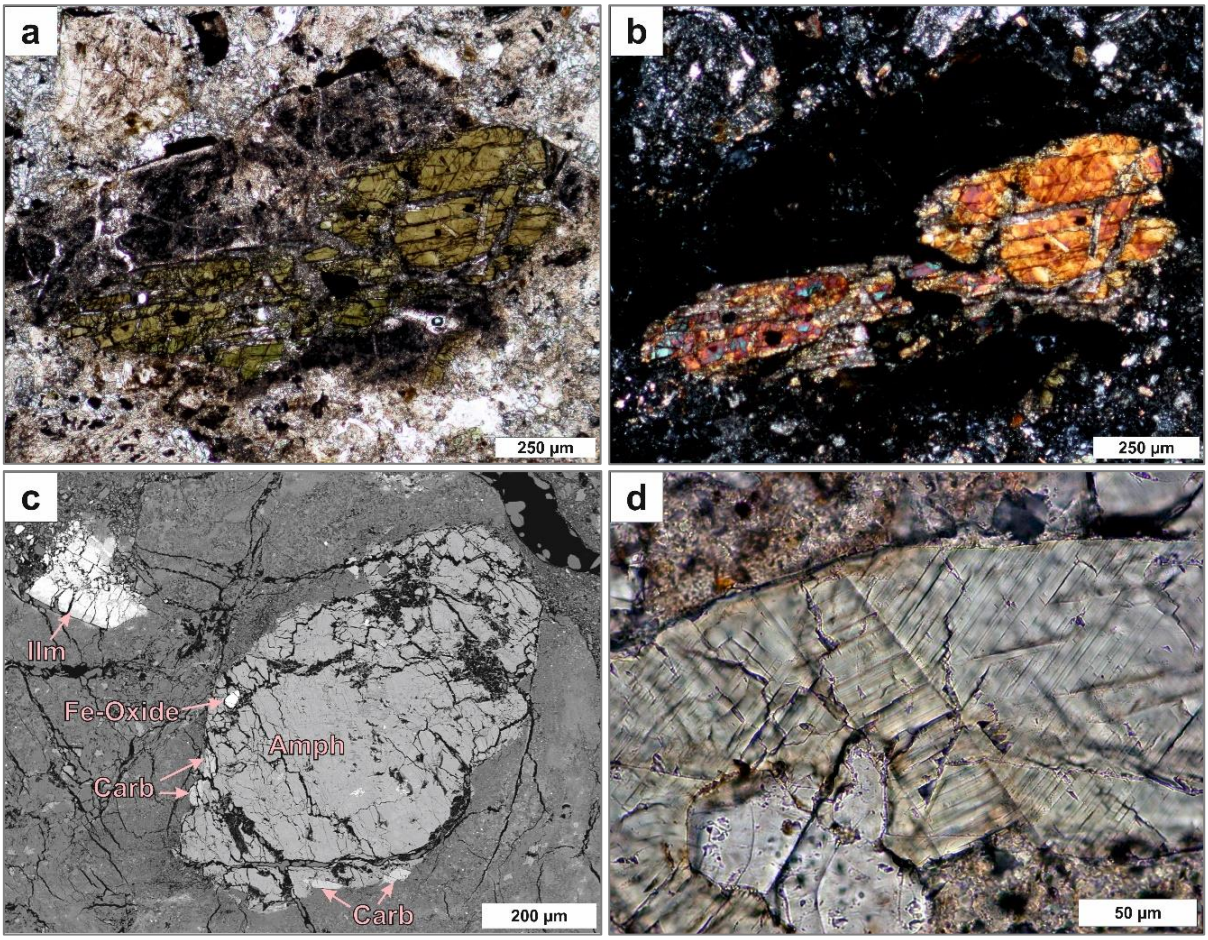

Fig. 21. a) *Microphotograph under plane-polarized light of an altered amphibole clast. Note the strong greenish intrinsic color. Optical microscopy. Sample 12 06, 315.82 mblf.* ***b)*** *The same grain under crossed-polarized light where the orange-pink pleochroic colors emerge. Optical microscopy.* ***c)*** *BSE-EM image of an amphibole clast (Amph) associated with Ca-carbonate crystals (Carb). Note the large ilmenite fragment in the left upper corner (Ilm). Sample 14 19, 316.93 mblf. Carb = Ca-carbonate, Ilm = ilmenite, Amph = amphibole.* ***d)*** *Section of an amphibole clast exhibiting kink bands. Plane-polarized light, optical microscopy. Sample 15b, 317.07 mblf.*

All analyzed amphibole clasts can be classified as calcic amphiboles. Plots of Si (in formula) and Al^{IV} (in formula) versus X_{Mg} after Leake et al. (1997) characterizes all amphiboles as ferro-tschermakites (Fig. 22 and Fig. 23). Amphibole analyses are shown in Table 5. These were calculated on the basis of 23 oxygens with estimation of Fe^{2+}/Fe^{3+} assuming 13 cations.

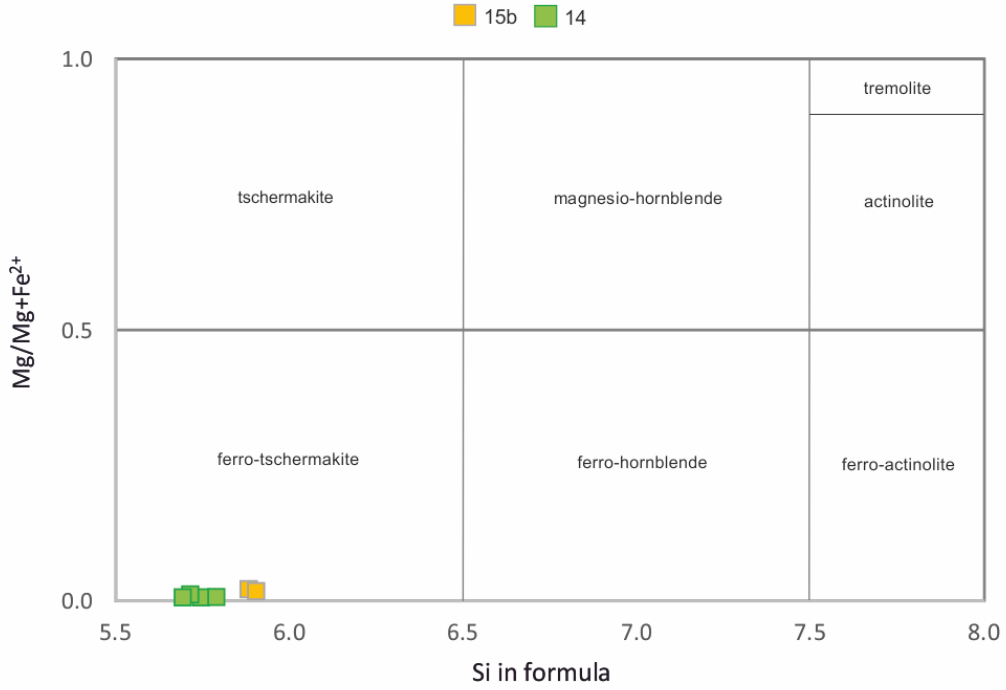

Fig. 22. *Amphibole classification diagram after Leake et al. (1997) in which Si in formula is plotted against X_{Mg} ($Mg/Mg+Fe^{2+}$). All amphibole can be classified as ferro-tschermakites, which belong to the group of calcic amphiboles.*

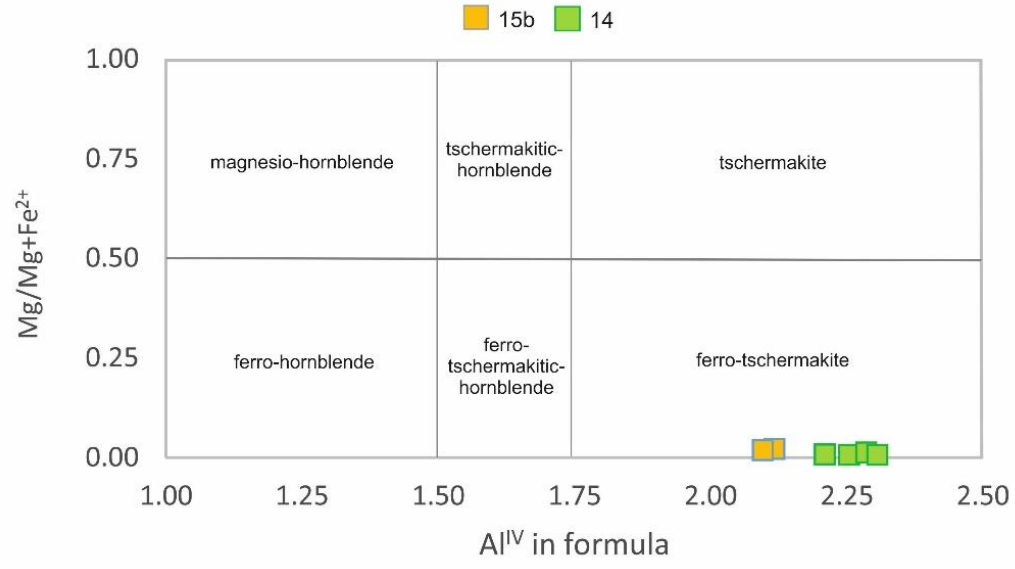

Fig. 23. *Plot of Al in formula in tetrahedral coordination versus X_{Mg} ($Mg/Mg+Fe^{2+}$) after Leake et al. (1997). All analyzed amphiboles can be classified as ferro-tschermakites.*

Table 5. *Major element analyses (in wt%) of amphiboles. Crystal chemical calculations are based on 23 oxygens with estimation of the Fe^{2+}/Fe^{3+} ratio assuming 13 cations. Sample 15b 23 represent granular amphibole relicts.*

Sample	***14***	***14***	***14***	***14***	***15b***	***15b***
Point	19_01	19_02	19_03	19_04	23_09	23_11
Classification	ferro-tschermakite	ferro-tschermakite	ferro-tschermakite	ferro-tschermakite	ferro-tschermakite	ferro-tschermakite
Grain size [µm]	800	800	800	800	<100	<100
Depth [mblf]	316.93	316.93	316.93	316.93	317.07	317.07
SiO_2	38.01	37.91	37.06	37.72	37.35	37.59
TiO_2	0.22	0.28	0.23	<0.08	0.23	0.09
Al_2O_3	23.79	24.18	20.57	24.55	19.67	19.78
Cr_2O_3	0.03	0.10	<0.02	0.05	0.02	<0.02
Fe_2O_3	-	-	-	-	-	-
FeO	9.96	10.02	13.76	9.72	13.97	14.00
MnO	0.30	0.23	0.15	0.45	0.09	0.09
MgO	0.03	0.07	0.05	0.03	0.17	0.14
CaO	23.40	23.14	23.03	23.23	22.49	22.47
Na_2O	0.01	<0.006	0.02	0.02	0.09	0.02
K_2O	0.01	0.01	<0.004	<0.004	0.06	0.09
H_2O*	1.98	1.99	1.92	1.99	1.90	1.91
Total	97.73	97.94	96.79	97.76	96.02	96.18
Calculations based on 23 oxygens with estimation of the Fe^{2+}/Fe^{3+} ratio assuming 13 cations						
Si	5.74	5.71	5.79	5.69	5.88	5.90
Al^{IV}	2.26	2.29	2.21	2.31	2.12	2.10
Al^{VI}	1.98	2.01	1.58	2.06	1.53	1.56
Ti	0.03	0.03	0.03	0.00	0.03	0.01
Cr	0.00	0.01	0.00	0.01	0.00	0.00
Fe^{3+}	-	-	-	-	-	-
Fe^{2+}	1.26	1.26	1.80	1.23	1.84	1.84
Mn	0.04	0.03	0.02	0.06	0.01	0.01
Mg	0.01	0.01	0.01	0.01	0.04	0.03
Ca	3.79	3.74	3.85	3.76	3.79	3.78
Na	0.00	0.00	0.01	0.01	0.03	0.01
K	0.00	0.00	0.00	0.00	0.01	0.02
OH*	2.00	2.00	2.00	2.00	2.00	2.00
Total	17.11	17.10	17.29	17.12	17.28	17.26
$(Ca+Na)_{(B)}$	3.79	3.74	3.85	3.76	3.79	3.78
$(Na+K)_{(A)}$	0.00	0.00	0.01	0.01	0.04	0.02
X_{Mg} (Fe^{2+})	0.01	0.01	0.01	0.01	0.02	0.02
Sum of S2	11.32	11.36	11.43	11.36	11.45	11.46

„-„= no result after Fe^{3+} calculation; Oxides in wt%; All samples analyzed by EPMA; The following abbreviations are based on the general amphibole structural formula A B_2 C_5 T_8 O_{22} $(OH)_2$: $(Ca+Na)_{(B)}$ = the sum of the cations Ca and Na in the octahedral B-site, $(Na+K)_{(A)}$ = the sum of the cations Na and K in the large A-site, X_{Mg} (Fe^{2+}) = $Mg/Mg+Fe^{2+}$, Sum of S2 = the sum of remaining cations in the C- and T-sites.

6.2.1.2.6 Phyllosilicates

Phyllosilicates are represented by biotite, white mica, and chlorite. Biotite, as single crystal in the suevite, has sizes up to 350 µm. To a lesser extent it occurs within volcanic clasts. Most biotite crystals are subhedral and partially replaced by chlorite or Fe-oxide. Large biotite (200 to 350 µm) clasts within the suevite frequently show kink bands (Figs. 24 a-d). The ternary classification diagram after Foster (1960) or Trochim (1966) in Tröger (1982) shows that nearly all analyzed biotites plot in the annite domain close to the border of the field of lepidomelane (Fig. 25). There is just one grain that can be classified as lepidomelane. Representative biotite analyses are given in Table 6. Li_2O and H_2O were calculated after Tindle and Webb (1990) and O, OH, F, Cl were calculated on the basis of 24 oxygens.

White mica is represented by muscovite and occurs quite rarely as single clasts within the suevite. Compared to biotite, muscovite sheets are smaller reaching sizes up to 150 µm. Under the optical microscope it was difficult to identify single muscovite grains. One could only assume whether or not it is muscovite. SEM- and EM-analyses however, revealed that muscovite clasts occur scarcer than presumed. It became obvious that many muscovite clasts are strongly carbonated (Fig. 24e) which is why its determination under the optical microscope was quite challenging. Some of the few major element analyses of muscovite are shown in Table 6. H_2O was calculated after Tindle and Webb (1990) and O, OH, F, and Cl were calculated on the basis of 24 oxygens.

Chlorite is represented in every single thin section. It occurs as single clasts in the suevite and as well as alteration products of biotite. It also acts as filling material of fractures within various clasts, even melt clasts (Fig. 24e). Chlorite clasts within the suevite are clearly discernible due to their greenish intrinsic color. They form flakes that are about 200 µm in size and sometimes even exhibit kink bands (Fig. 24f). Representative major element analyses are given in Table 6. Calculations are based on 28 oxygens with Fe^{2+}/Fe^{3+} and OH assuming full site capacity. Chlorite minerals show differences in chemical composition based on continuous cation substitution wherefore there are a variety of names. Plotting Si (in formula) versus X_{Mg} ($Mg/Mg+Fe^{tot}$) after Bailey (1988) shows that the analyzed chlorites can be classified as both, chamosites as well as clinochlores (Fig. 26). Especially those of sample 15b increasingly tend to plot in the chamosite section. Another more precise classification diagram after Hey (1954) plots Si (in formula) against Fe^{tot} (Fe^{2+} + Fe^{3+} in formula) as shown in Fig. 27. Accordingly, the analyzed chlorites can be classified as brunsvingites and pycnochlorites.

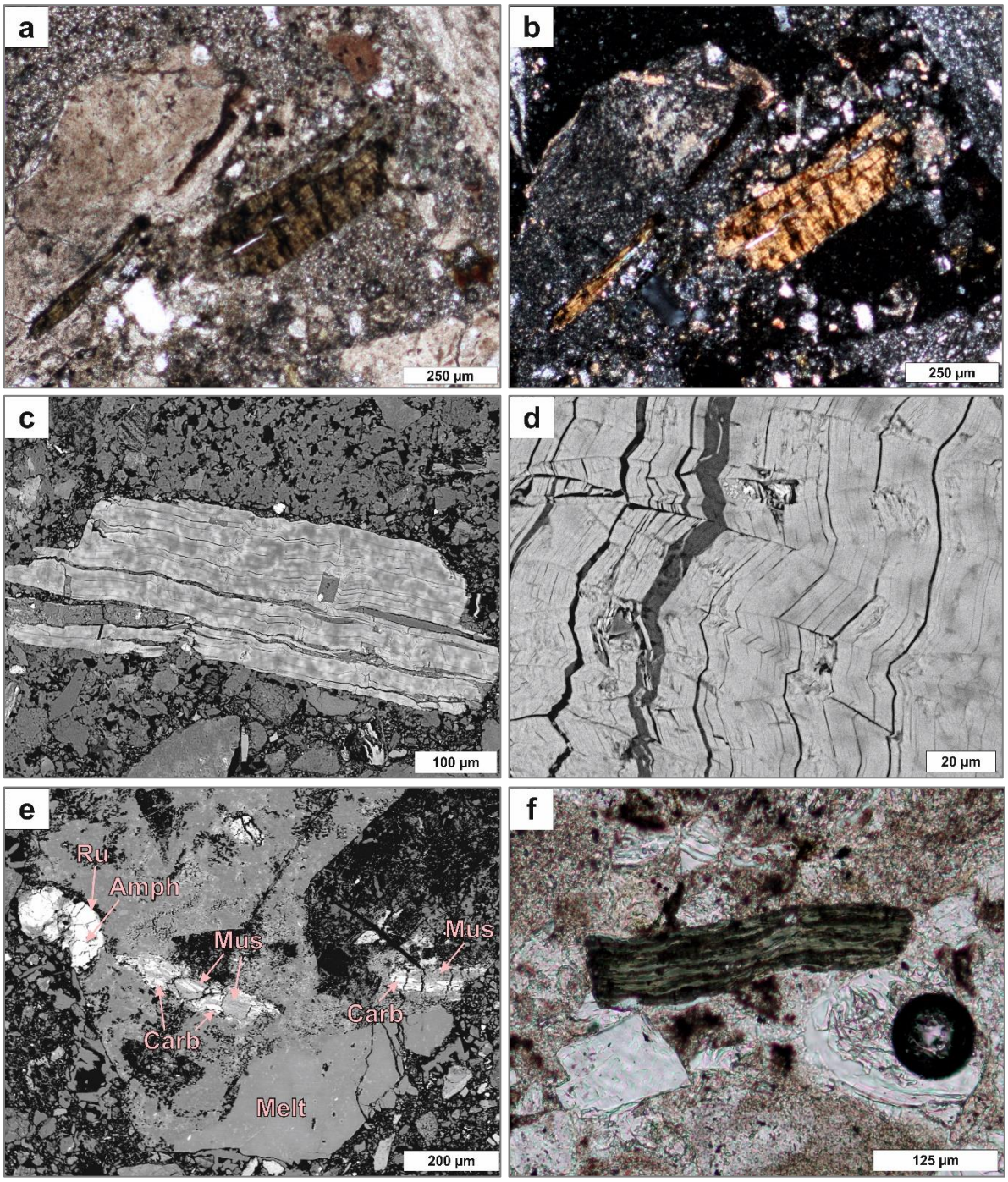

Fig. 24. a) *Microphotograph under plane-polarized light of a kinked biotite clast. Optical microscopy. Sample 6 05, 314.27 mblf.* ***b)*** *The same biotite clast under crossed polarized light. Optical microscopy.* ***c)*** *BSE-EM image displaying a kinked biotite clast. The light areas within the grain represent biotite compositions whereas the dark spots exhibit a clay mineral composition. Sample 11 02, 315.59 mblf.* ***d)*** *The same grain under higher magnification highlighting details of the kink bands. BSE-SEM image.* ***e)*** *Melt fragment hosting carbonated (Carb) muscovite (Mus) and amphibole (Amph) associated with rutile (Ru). Fractures of this melt fragment are filled with chlorite. Sample 15b 05, 317.07 mblf. BSE-EM image.* ***f)*** *Microphotograph of a kinked chlorite clast. Sample 6 16, 314.27 mblf. Plane-polarized light, optical microscopy.*

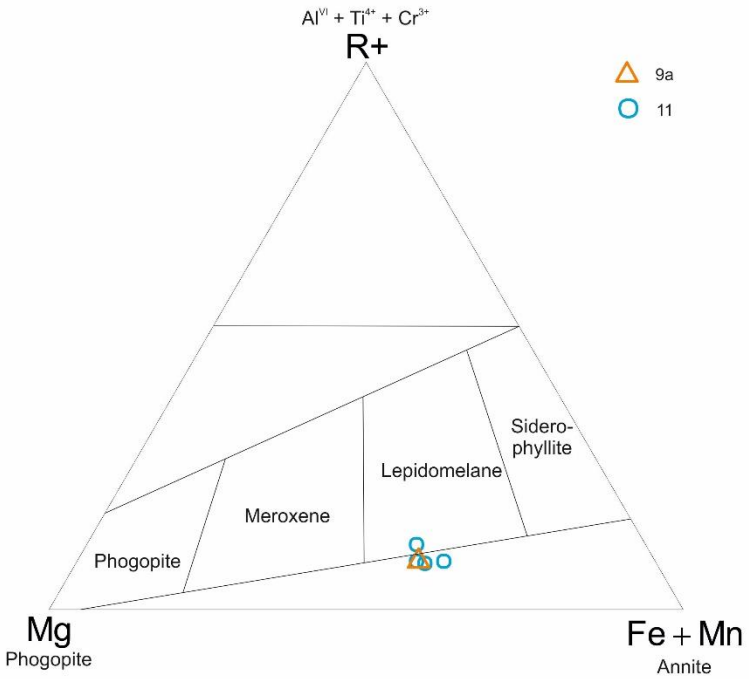

← ***Fig. 25.*** *Ternary biotite classification diagram after Foster (1960) or Trochim (1966) in Tröger (1982). Nearly all analyzed biotites plot in the annite section close to the border of the field of lepidomelane. The lower right corner represents $Fe^{2+}+Mn$ and $R^{+}= Al^{VI}+Ti^{4+}+Cr^{3+}$.*

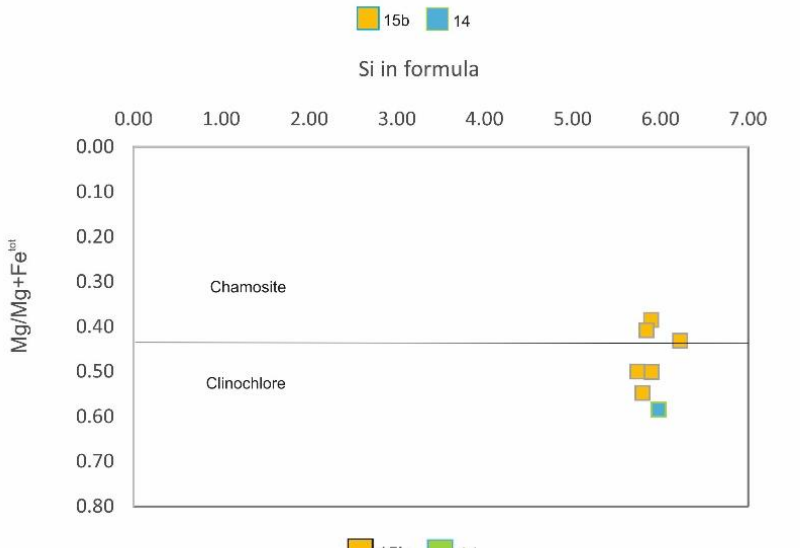

← ***Fig. 26.*** *Chlorite classification after Bailey (1988) based on plotting Si in formula against X_{Mg} = (Mg/Mg+Fe^{tot}). All analyzed chlorites can be classified as both clinochlores and chamosites.*

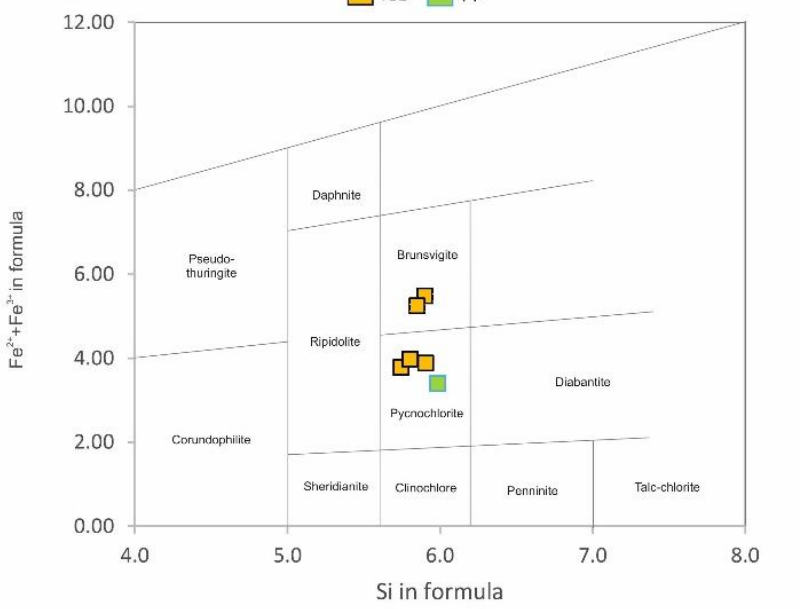

← ***Fig. 27.*** *Classification diagram after Hey (1954) for chlorites. Analyzed chlorites are brunsvingites and pycnochlorites.*

***Table 6**. Representative major element analyses (in wt%) of biotite, muscovite, and chlorite. Crystal chemical calculations for biotite and muscovite are based on 24 oxygens, and on 28 oxygens for chlorite. Fe_2O_3 has only been calculated for chlorite. LiO_2 and H_2O have been calculated after Tindle and Webb (1990).*

Sample	***9a***	***11***	***11***	***11***	***11***	***15b***	***15b***	***14***	***15b***	***15b***
Point	16_12	02_02	12_01	12_02	12_04	2_03	05_06	2_05	2_07	2_02
Classifi-cation	bt	bt	bt	bt	mus	mus	mus	chl	chl	chl
Grain size [µm]	250	550	600	600	150	<250	250	50	250	250
Depth [mblf]	315.02	315.59	315.59	315.59	315.59	317.07	317.07	316.93	317.07	317.07
SiO_2	35.53	34.94	35.90	35.65	49.46	48.62	49.27	28.84	26.74	28.01
TiO_2	4.22	3.60	3.75	3.99	0.30	0.18	0.14	0.12	0.27	2.73
Al_2O_3	12.91	15.37	13.28	13.13	28.72	27.63	24.16	20.09	17.75	20.70
Fe_2O_3	n.m.	n.m.	n.m.	n.m.	n.m.	n.m.	n.m.	3.13	1.63	4.62
FeO	22.59	22.20	22.99	24.27	4.45	5.43	6.34	16.77	28.24	17.90
MnO	0.22	0.33	0.28	0.22	0.02	0.06	0.02	0.13	0.27	0.25
MgO	8.87	8.78	8.72	7.94	1.17	2.36	3.10	15.50	10.44	12.37
CaO	<0.01	<0.01	<0.01	<0.01	<0.01	0.34	0.19	0.15	0.11	0.20
Na_2O	0.46	0.52	0.55	0.42	0.01	0.22	0.12	0.07	0.05	0.06
K_2O	8.64	8.42	8.69	8.78	10.08	7.74	9.64	0.35	0.12	0.51
Li_2O	0.65	0.48	0.75	0.68	n.m.	n.m.	n.m.	n.m.	n.m.	n.m.
H_2O	3.81	3.85	3.84	3.82	4.42	4.36	4.30	11.43	10.81	11.51
Total	97.89	98.49	98.74	98.92	98.63	96.93	97.27	96.58	96.42	98.85
Si	5.59	5.44	5.60	5.59	6.71	6.69	6.86	5.99	5.90	5.74
Al^{IV}	2.39	2.56	2.40	2.41	1.29	1.31	1.14	2.01	2.10	2.26
Al^{VI}	0.00	0.26	0.05	0.02	3.31	3.16	2.83	2.95	2.54	2.83
Ti	0.50	0.42	0.44	0.47	0.03	0.02	0.01	0.02	0.04	0.42
Fe^{3+}	n.m.	n.m.	n.m.	n.m.	n.m.	n.m.	n.m.	0.49	0.27	0.71
Fe^{2+}	2.97	2.89	3.00	3.18	0.51	0.62	0.74	2.91	5.21	3.07
Mn	0.03	0.04	0.04	0.03	0.00	0.01	0.00	0.02	0.05	0.04
Mg	2.08	2.04	2.03	1.86	0.24	0.48	0.64	4.79	3.43	3.78
Li	0.41	0.30	0.47	0.43	n.m.	n.m.	n.m.	n.m.	n.m.	n.m.
Ca	0.00	0.00	0.00	0.00.	0.00	0.05	0.03	0.03	0.03	0.04
Na	0.14	0.16	0.17	0.13	0.00	0.06	0.03	0.06	0.05	0.05
K	1.73	1.67	1.73	1.76	1.75	1.36	1.71	0.19	0.07	0.27
OH	4.00	4.00	4.00	4.00	4.00	4.00	4.00	16.00	16.00	16.00
Total	19.85	19.79	19.92	19.88	17.83	17.76	18.01	35.47	35.70	35.21
Y_{total}	5.99	5.96	6.02	5.99	4.08	4.30	4.23	-	-	-
X_{total}	1.87	1.83	1.90	1.89	1.75	1.46	1.77	-	-	-
Al_{total}	2.39	2.82	2.44	2.43	4.59	4.48	3.97	-	-	-
X_{Fe}	0.59	0.59	0.60	0.63	0.68	0.56	0.53	0.41	0.61	0.50
X_{Mg}	0.41	0.41	0.40	0.37	0.32	0.44	0.47	0.59	0.39	0.50

n.m. = not measured; Oxides in wt%; All samples analyzed by EPMA; The abbreviations X and Y are based on the general formula for minerals of the mica group $XY_{2-3}Z_4O_{10}(OH, F)_2$; X_{Fe} = Fe/Fe+Mg; X_{Mg} = Mg/Mg+Fe.

6.2.1.3 Lithic Clasts

Numerous lithic fragments occur in various sizes and compositions. Even different stages of partial melting can be documented. In general, it can be reported that there are two main types: (1) altered lithic fragments of possible volcanic origin (Figs. 28 a-e) and (2) partially molten clasts mostly of feldspathic composition (Figs. 28 f-h). Lithic volcanic fragments (1) exhibit strong variations in mineralogy, color, and alteration stages. There are basaltic- to andesitic-looking fragments and opaque ones that are highly altered, probably oxidized, which is why it is difficult to determine their current mineralogy and therefore their original one. Volcanic fragments containing identifiable minerals such as laths of plagioclase and pyroxene grains exhibit irregular clast shapes with rare sharp edges at some places. Their alteration is not as advanced wherefore most of their phenocrystals are still recognizable under the optical microscope. Partially molten fragments (2) host mostly still crystallized rutile, Fe-oxide, and apatite (Figs. 28 f-h). They are embedded within a flow texture that resembles schlieren (Fig. 28h). These flow textures can be divided in leuco- and melanosomes. The lighter areas (leucosome) exhibit Na-feldspar chemistries whereas the darker regions (melanosome) display K-feldspar compositions.

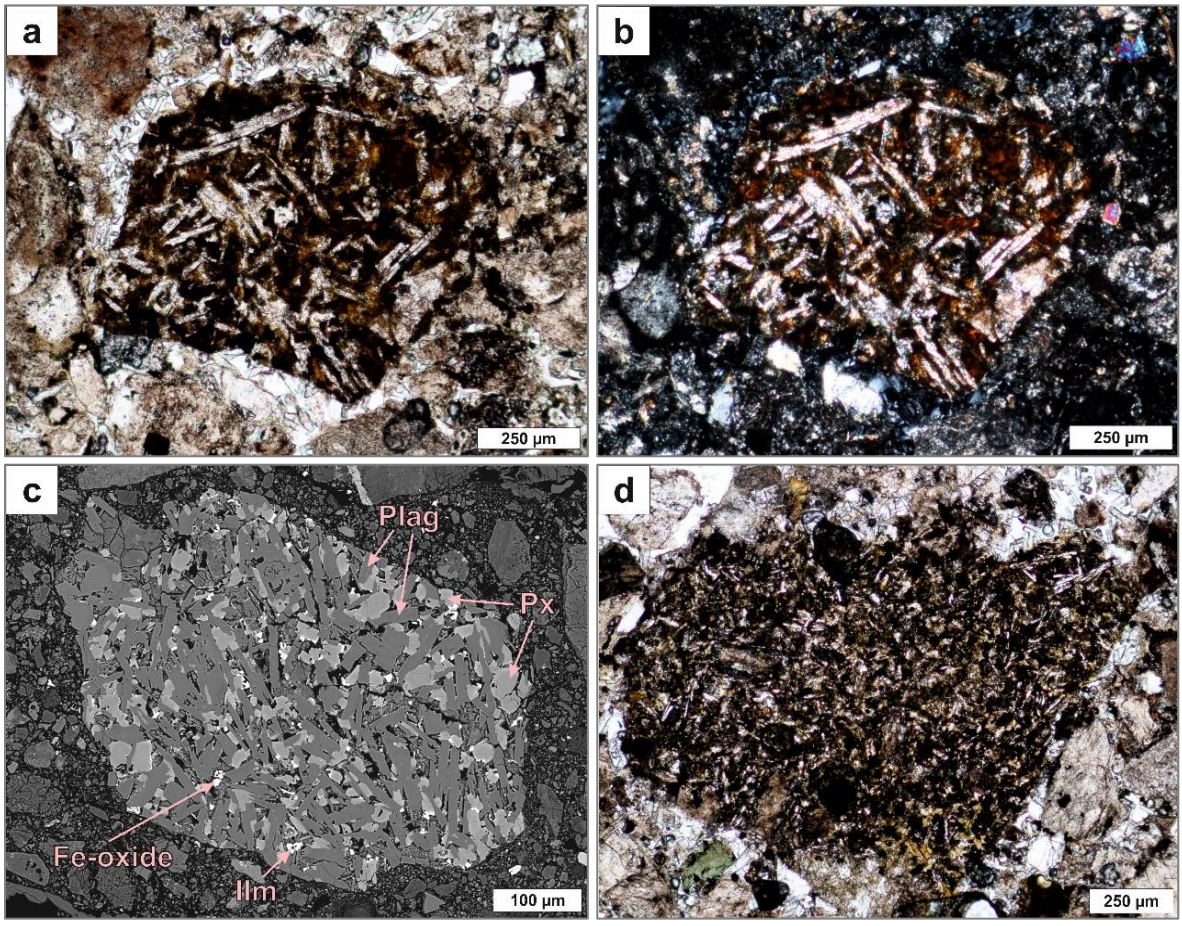

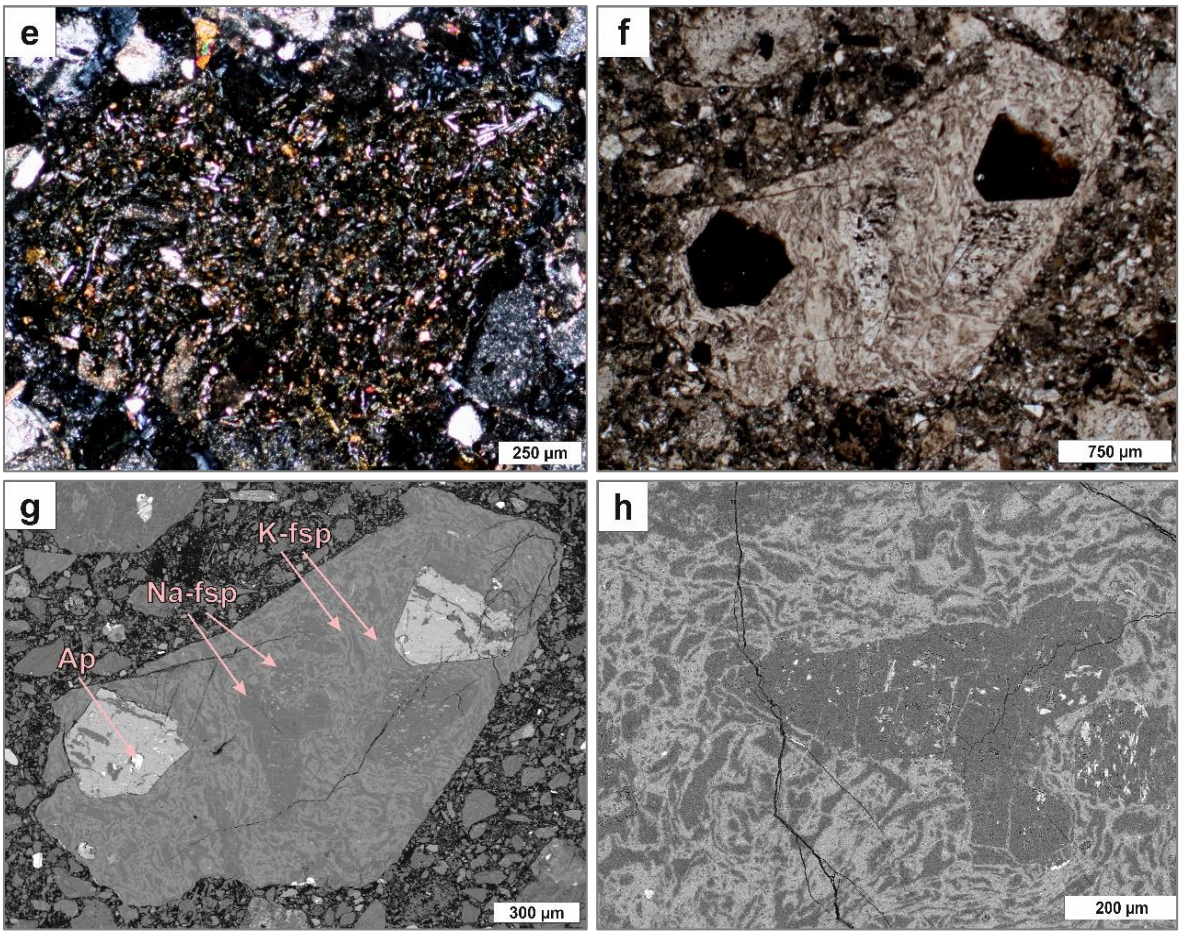

Fig. 28. a) *Microphotograph under plane-polarized light of an altered volcanic fragment yielding smooth, but sharp boundaries to the surrounding rock. Optical microscopy. Sample 14 18, 316.93 mblf.* ***b)*** *The same image under crossed-polarized light. Optical microscopy.* ***c)*** *BSE-EM image of the same fragment displaying an intergranular texture. The laths within the clast represent plagioclase (Plag) crystals, which are partially enclosed by smaller pyroxene (augite) grains (Px). The fragment also contains small grains of Fe-oxide and ilmenite (Ilm).* ***d)*** *Volcanic fragment under plane-polarized light. There are laths of plagioclase enclosed by probably pyroxene grains. Optical microscopy. Sample 8 06, 315.50 mblf.* ***e)*** *The same clast under crossed-polarized light. Optical microscopy.* ***f)*** *Partially molten fragment hosting two large eu- to subhedral rutile (Ru) crystals. Note the flow texture within the clast. Sample 15b 02, 317.07 mblf. Plane-polarized light, optical microscopy.* ***g)*** *BSE-EM image of the same fragment. The rutile (Ru) crystals also contain apatite (Ap), quartz (Qtz), and chlorite (Chl). The flow textures enclosing the rutile crystals reveal different grey-scales indicating different chemical compositions. The darker flow bands show Na-feldspar (Na-fsp) compositions whereas the lighter ones have the compositions of K-feldspar (K-fsp).* ***h)*** *The central part of the same fragment at higher magnification. Note the relicts of feldspar still exhibiting a crystal structure. BSE-SEM image.*

6.2.1.4 Melt Clasts

The strong variability of melt fragments in size, color, porosity, and abundance represents a major challenge for their classification. The selected samples also exhibit a large local variability wherefore it is quite difficult to give a rough estimation of occurrence. There are (1) strongly vesiculated whitish melt fragments, (2) blackish irregularly shaped, and (3) brown- to greenish fragments with internal flow textures.

The vesiculated whitish fragments (Fig. 29a) (1) occur all over the samples of the transition layer, but exhibit strong variations mostly in size and density. There are centimeter sized fragments (≤ 5 cm) with irregular edges incorporating surrounding rock material. They exhibit vesicles that are mostly filled with secondary K-Na-Ca aluminosilicates exhibiting spherulitic growth. The largest fragments of this kind reach sizes up to 5 centimeters. One of those cm-sized fragments (Sample 5) hosts sub- to anhedral augite crystals that show alterations to Fe-oxide at their edges (Fig. 20 e-f). The smaller whitish melt clasts, under the optical microscope, within the suevite reach sizes of about 0.5 mm and are as well of irregular shape with no definite edges. These melt vesicles exhibit a smooth contact to the adjoining matrix and mineral clasts. Most of the vesicles are filled with either mixed crushed material, probably derived from the matrix, granulates of Ca-carbonates or polishing material (Fig. 12). The space in between the vesicles is glass with perlitic textures. Interestingly, these interstices reveal extraordinary fracture patterns (Figs. 29 e-f). The vesicles can be described as circular to ellipsoidal in shape and are either randomly distributed within the melt clast or show alignment with existing flow structures (Fig. 29a left clast). There are as well denser whitish melt clasts that reach sizes up to 1 cm. Theses occur much scarcer and exhibit rounded shapes and sharp boundaries to the surrounding material. The vesicles within those clasts are always aligned along flow structures.

Blackish (2) fragments, under the optical microscope, occur all over the samples from the transition layer. Macroscopically, they appear denser and locally contain vesicles that occur within certain flow bands. They exhibit sharp, but smooth boundaries with the surrounding rock. Under the optical microscope, they also contain brownish material that resembles in bands alternating from blackish bands to form flow structures enhanced by the occurrence of schlieren. These color bands might reflect different chemical compositions. Locally, there are flow bands that host tiny crystals reflecting different stages of crystallization. Even vesicles can be incorporated in these flow bands. These fragments mostly reach sizes ranging from 1.5 mm to several centimeters.

The brown- to greenish melt clasts (3) reveal internal patterns that appear stained (Fig. 29c), but with no indications of flow. Relicts of former crystals can be discovered randomly distributed within those clasts. They completely lack of vesicles and show a greater density.

Representative electron microprobe analyses of major elements of diverse melt clasts are given in Table 7. Back-scattered electron (BSE) images reveal grey-scale differences within many melt clasts concluding to heterogeneous chemical compositions (Figs. 29 f-h). The complex flow patterns sometimes even resemble a schlieren texture (Fig. 29g). All analyzed melt clasts

are plotted in Fig. 31 in a total alkali versus silica diagram (TAS) after Le Bas et al. (1986). The majority of the clasts show dacitic to rhyolitic compositions. Except three analyses of sample 9b plot in the basalt domain. These represent the lighter areas under the grey-scale BSE-image (Fig. 29h pink arrows). Harker diagrams of major elements plotted against SiO_2 are represented in Fig. 31.

***Table 7**. Representative electron microprobe analyses of major elements of several melt fragments (in wt%). At the BSE -EM images different grey-scale colors have been observed, which represent different chemical compositions.*

Sample	***14***	***14***	***14***	***14***	***8***	***9b***	***9b***	***9b***	***9b***
Point	22 det1 m	22 det1 d	22 det2 h	22 det3 h	melt6	melt5 h	melt5 h	melt5 d	melt5d
BSE color	medium	dark	light	light	medium	light	light	dark	dark
Clast size [mm]	5	5	5	5	0.6	≤ 1.2	≤ 1.2	≤ 1.2	≤ 1.2
Depth [mblf]	316.93	316.93	316.93	316.93	315.50	314.98	314.98	314.98	314.98
SiO_2	70.23	72.54	63.36	67.26	67.58	51.14	49.56	69.84	69.16
Al_2O_3	14.60	14.54	15.17	14.93	14.07	15.43	15.66	13.60	13.63
Cr_2O_3	<0.02	<0.02	0.05	0.11	<0.02	0.02	0.05	0.03	0.03
TiO_2	0.28	0.11	0.60	0.44	0.24	0.62	0.69	0.11	0.25
K_2O	3.90	4.42	2.71	3.28	5.52	1.36	1.18	4.39	4.24
CaO	3.05	1.98	5.98	3.91	2.37	3.17	3.50	1.98	2.40
FeO	2.79	1.92	4.65	3.70	1.95	14.60	15.31	2.09	2.19
MnO	0.07	0.07	0.10	0.07	0.05	0.13	0.15	0.02	0.06
Na_2O	3.09	3.49	2.67	3.01	2.94	1.41	1.64	3.08	2.94
MgO	1.58	0.54	3.15	2.35	0.55	9.23	9.68	0.62	0.81
NiO	<0.01	<0.01	0.03	0.05	n.m.	n.m.	n.m.	n.m.	n.m.
Total	99.58	99.59	98.45	99.11	95.27	97.11	97.40	95.76	95.71

Oxides in wt%; n.m. = not measured; All samples analyzed by EPMA.

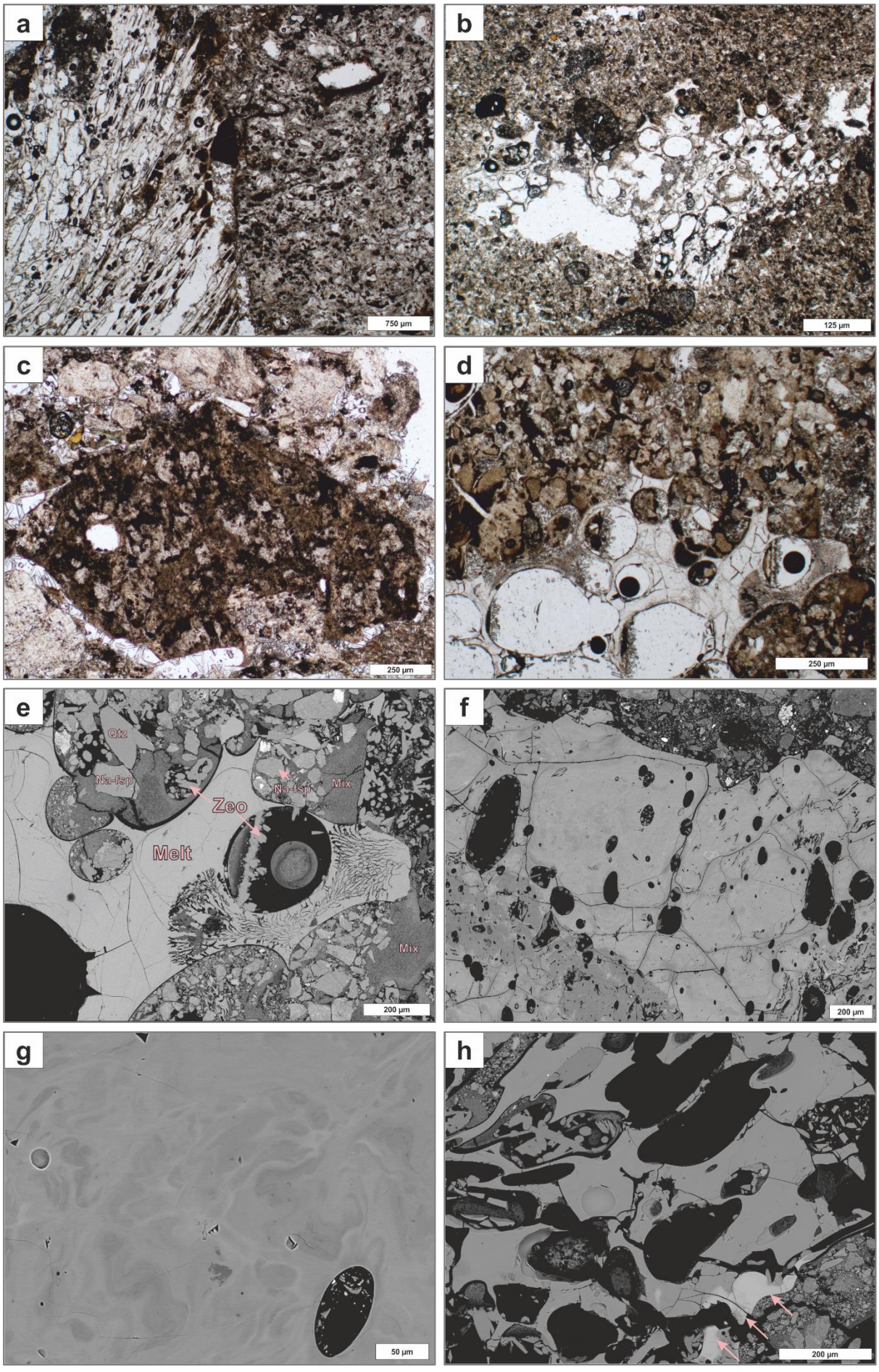
a
750 µm
b
125 µm
c
250 µm
d
250 µm
e
Qtz
Na-fsp
Na-fsp
Mix
Zeo
Melt
Mix
200 µm
f
200 µm
g
50 µm
h
200 µm

→ ***Fig. 29. a)*** *Two vesiculated melt fragments interacting with each other. Note that in both clasts the vesicles are aligned to the prevalent flow. Plane-polarized light, optical microscopy. Sample 9b 01, 314.98 mblf.* ***b)*** *Microphotograph under plane-polarized light of an irregularly shaped, strongly vesicular melt clast. The boundaries are indistinct and are incorporating surrounding rock material. Optical microscopy. Sample 5 04, 313.78 mblf.* ***c)*** *Brown- to greenish patchy melt clast with sharp, but smooth edges. This patchy texture might reflect relicts of former crystals. Plane-polarized light, optical microscopy. Sample 8 07, 315.50 mblf.* ***d)*** *Whitish vesiculated, irregularly shaped melt fragment with perlitic textures. Plane-polarized light, optical microscopy. Sample 9a 01, 315.02 mblf.* ***e)*** *BSE-SEM image of the same clast. The vesicles are partially filled with zeolites (Zeo) and the mixed crushed material (Mix) is probably derived from the matrix. Note the fracture patterns within the glass (Melt). Sodic feldspar = Na-fsp, quartz = Qtz.* ***f)*** *Large heterogeneous melt fragment with partially filled circular to ellipsoidal vesicles. The chemical heterogeneity is expressed by different grey-scales (see Table 7). BSE-EM image. Sample 14 22, 316.93 mblf.* ***g)*** *The same clast under higher magnification visualizing the compositional heterogeneity which is differentiated into a flow fabric with schlieren. BSE-EM image.* ***h)*** *BSE-EM image of a melt fragment with elongated vesicles that are consistent with the prevalent flow direction. Note the lighter areas (pink arrows) that yield basaltic compositions (see Fig. 30). Sample 9b melt5, 314.98 mblf.*

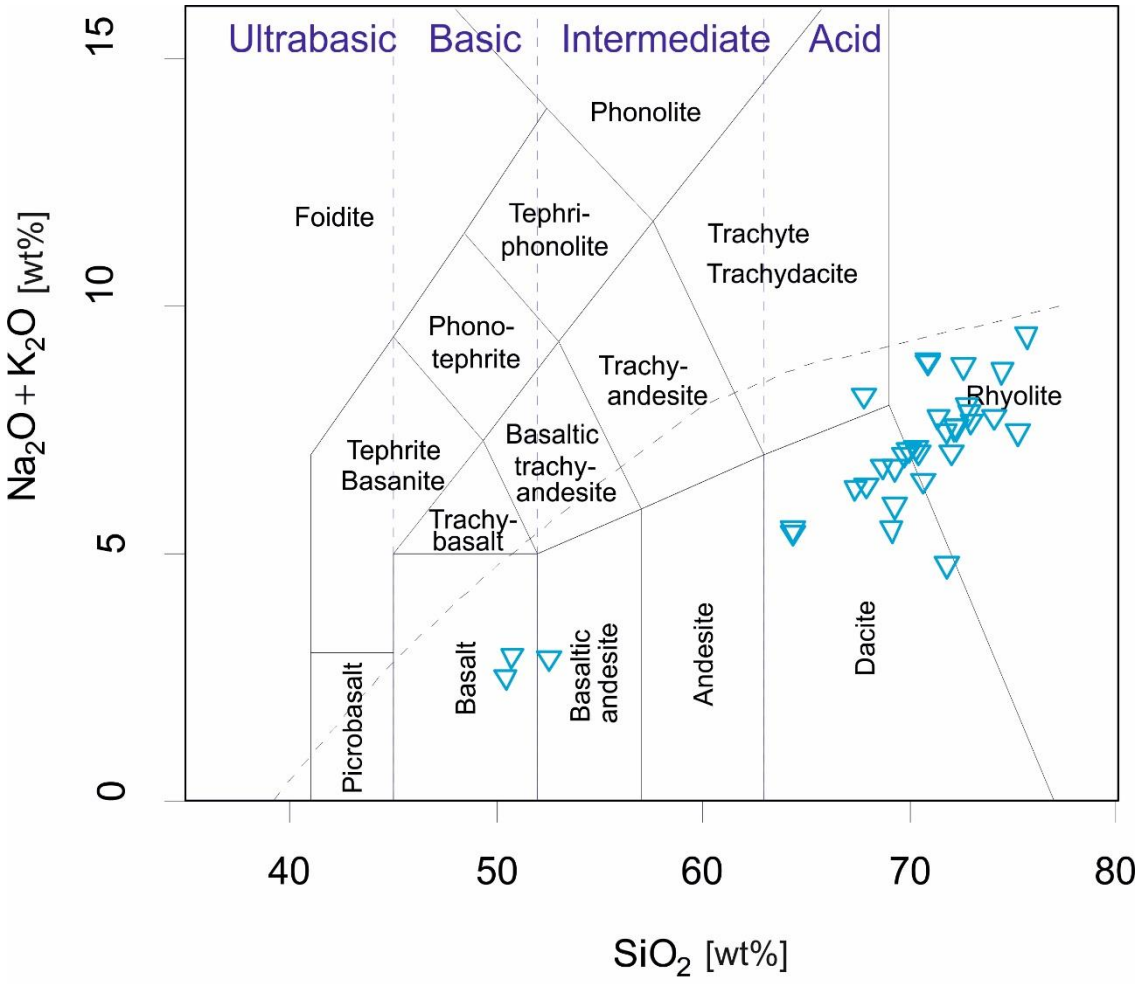

Fig. 30. *Total alkali versus silica (TAS) plot after Le Bas et al. (1986) of all analyzed melt fragments (point analyses) in wt%. The majority yields dacitic to rhyolitic compositions. Only three analyses of sample 8 plot in the basalt field. These represent areas within a heterogeneous melt clasts that are enriched in heavier elements (see Fig. 29 h (pink arrows)).*

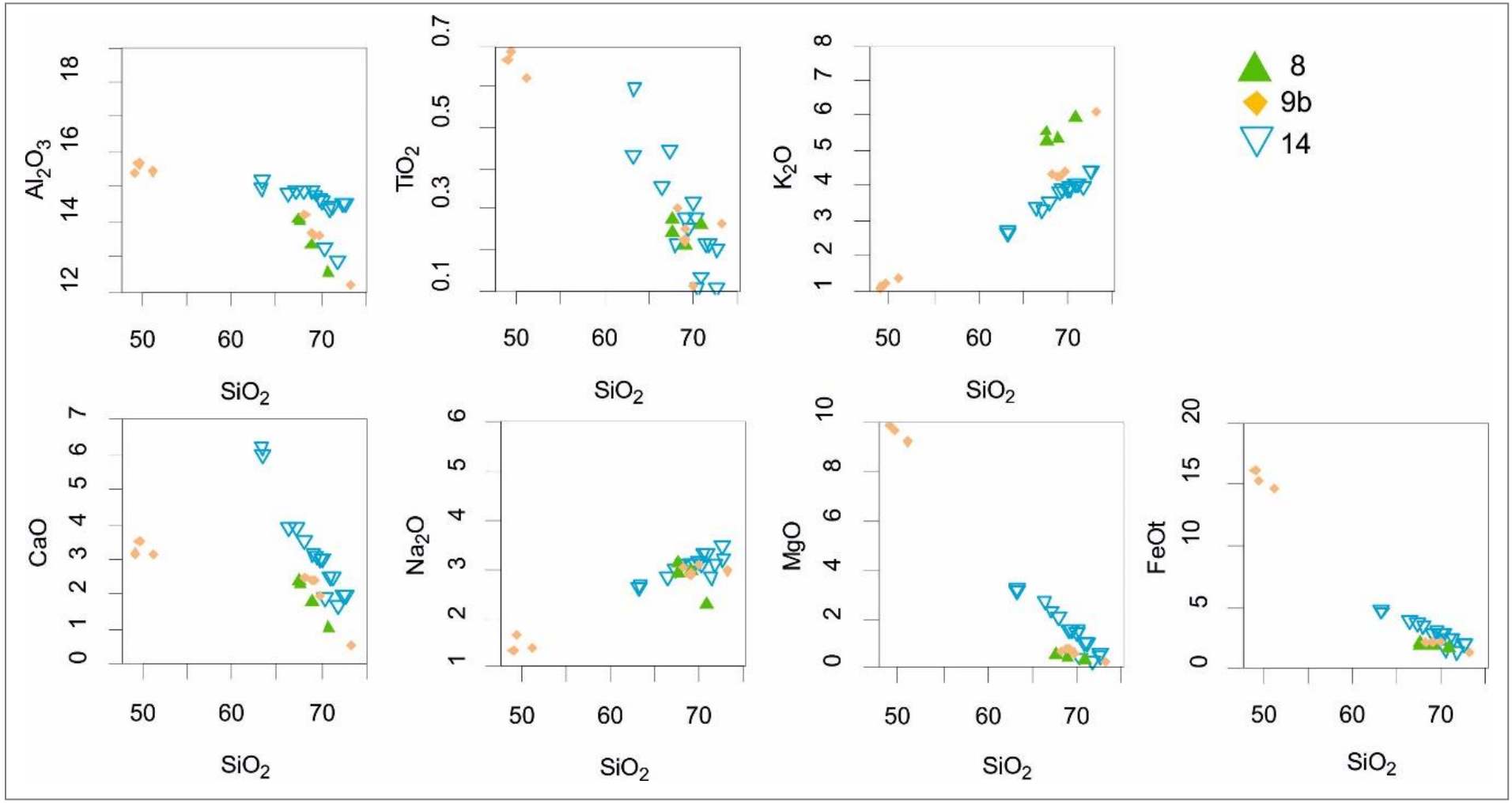

Fig. 31. *Multiple plots of major element contents versus SiO_2 (in wt%) of melt fragments.*

6.2.1.4.1 Glass Shards

Glass shards occur in every samples within the whole section of the transition layer. As indicated by their name, they exhibit shard-like shapes produced by airborne transport. In general, all melt shards are irregularly distributed within the suevite, sometimes even incorporating surrounding rock material (Figs. 32 e-h). They show sharp edges and an internal flow fabric that can even resemble schlieren (Figs. 32 a-e). Representative major element analyses of diverse melt shards are given in Table 8. Many melt shards are hydrated wherefore their total is lesser than 100 wt%. Homogenous melt shards show similar chemical compositions with SiO_2 contents ranging from 65 to 70 wt%. Heterogeneous melt shards however, yield varying chemistries. They contain flow fabrics that become apparent in grey-scale differences of BSE-images (Figs. 32 d-h). These grey-scale variations reflect chemical differences. Lighter areas are richer in FeO, MgO, and TiO_2 wherefore darker areas contain more SiO_2, K_2O, and Na_2O. Multiple plots based on SiO_2 against some major elements reveal such internal differences in composition (Fig. 34). There is even one melt shard that contains a dark grey rounded area that yields quartz chemistries with 99.46 wt% SiO_2 (Fig. 32g and Table 8 Sample 9b melt4).

Table 8. *Representative major element analyses (in wt%) of melt shards. There are chemical variations within some shards (MK 9b melt 4, MK 14 20, MK 15b 07).*

Sample	***MK 8***	***MK 9a***	***MK 9b***	***MK 9b***	***MK 14***	***MK 14***	***MK 14***	***MK 14***	***MK 14***	***MK 15b***	***MK 15b***	***MK 15b***
Point	melt 5	14_1_ 05	melt 4 d	melt 4 h	14p d-rim	14p m-core	20 h-rim	20 m	20 d	07 melt shard 01	07 melt shard 02	07 melt shard 03
Grey-scale (BSE)	-	-	dark	light	dark	me-dium	light	me-dium	dark	dark	grey	light
Depth [mblf]	315.50	315.02	314.98	314.98	316.93	316.93	316.93	316.93	316.93	317.07	317.07	317.07
Size [µm]	180	950	420	420	400	400	520	520	520	200	200	200
SiO_2	66.06	68.51	99.46	67.84	69.93	70.99	53.64	67.71	86.00	93.96	68.86	64.96
Al_2O_3	16.64	14.09	0.14	13.86	14.91	15.27	15.52	14.52	5.32	2.42	14.53	15.68
Cr_2O_3	<0.02	0.02	0.03	0.02	<0.02	<0.02	0.05	0.04	<0.02	0.02	0.05	<0.02
TiO_2	0.72	0.15	<0.07	0.40	0.38	0.30	2.23	0.41	0.09	<0.07	0.21	0.26
K_2O	3.27	4.30	0.11	3.71	3.65	3.68	2.01	3.97	2.66	1.43	4.75	4.24
CaO	4.19	2.32	0.02	3.37	2.88	2.83	5.83	2.48	0.47	0.10	1.87	3.11
FeO[a]	4.37	2.05	0.10	4.34	2.80	2.82	9.67	2.38	1.09	0.73	1.96	3.17
MnO	0.08	0.06	<0.02	0.07	0.11	0.08	0.21	<0.02	0.05	0.03	0.09	0.09
Na_2O	3.49	2.94	0.05	3.19	2.67	2.44	2.53	3.37	1.30	0.62	2.94	2.83
MgO	1.47	0.63	<0.01	2.93	0.95	0.96	4.79	0.87	0.40	0.23	0.81	1.68
NiO	n.m.	n.m.	n.m.	n.m.	n.m.	n.m.	n.m.	0.02	<0.01	0.02	<0.01	0.01
Total	100.3	95.08	99.96	99.73	98.29	99.36	96.48	95.77	97.38	99.58	96.06	96.03

[a] All iron as FeO; n.m. = not measured; All analyses in wt% and measured by EPMA.

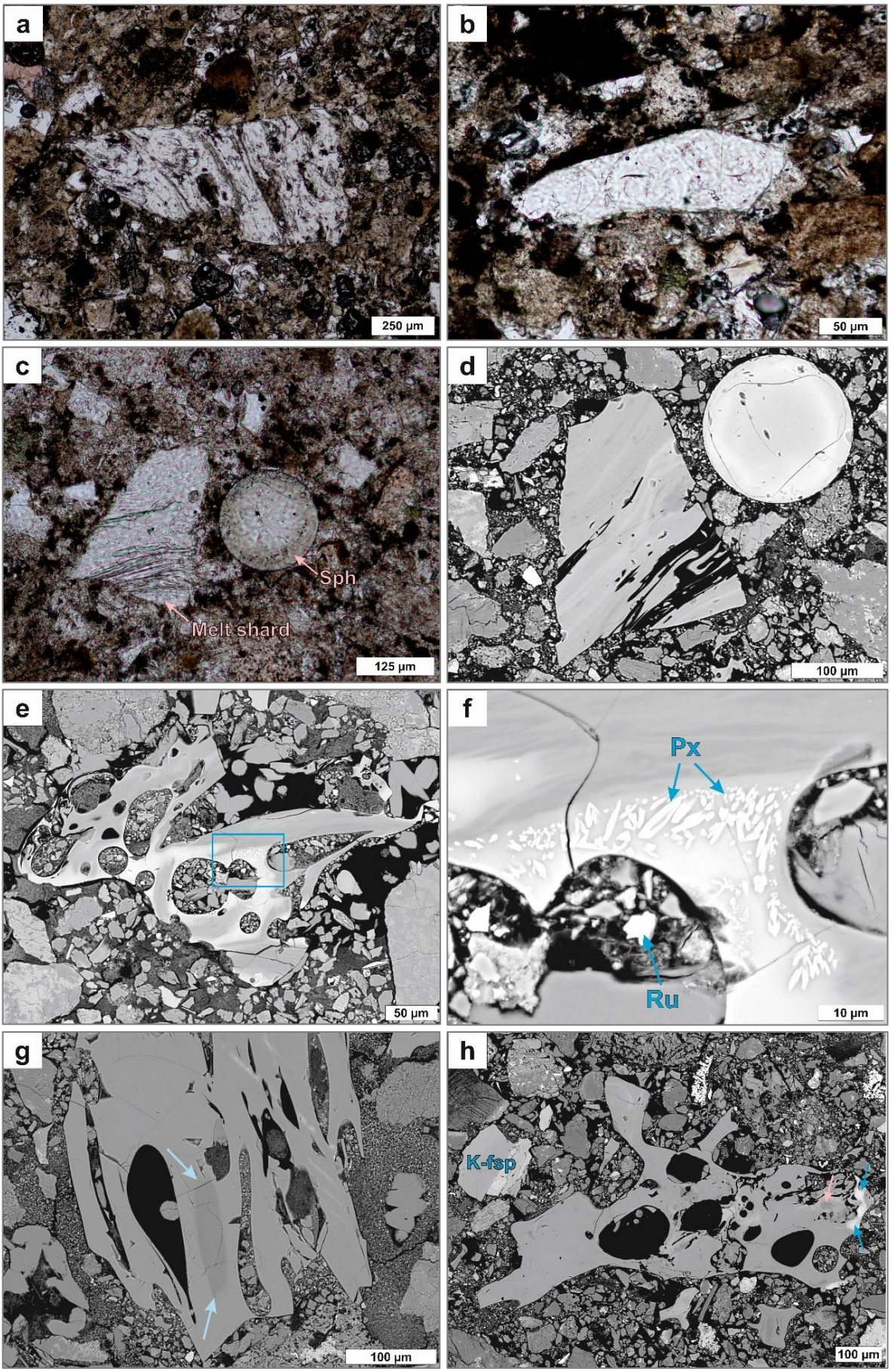
a
250 µm
b
50 µm
c
Sph
Melt shard
125 µm
d
100 µm
e
50 µm
f
Px
Ru
10 µm
g
100 µm
h
K-fsp
100 µm

← ***Fig. 32. a)*** *Microphotograph under plane-polarized light of a melt shard revealing an internal flow fabric. Optical microscopy. Sample 9a 07, 315.02 mblf.* ***b)*** *Melt shard showing perlitic textures. Plane-polarized light, optical microscopy. Sample 6 12, 314.27 mblf.* ***c)*** *Microphotograph of a melt shard next to a spherule. Plane-polarized light, optical microscopy. Sample 15b 07, 317.07 mblf.* ***d)*** *BSE-EM image of the same section. Note the heterogeneous composition of the melt shard that becomes apparent in grey-scale variations. The darkest spot within the melt shard yields SiO_2 contents of 93.96 wt% (see Table 8, MK 15b melt shard 01).* ***e)*** *Vesiculated melt shard exhibiting internal chemical variations and hosting pyroxene (Px) crystals (blue rectangle) that reach sizes from 5 to 20 µm. BSE-EM image. Sample 9b melt1, 314.98 mblf.* ***f)*** *The same shard under higher magnification (blue rectangle from e) revealing the pyroxene (Px) crystals. Note that their occurrence is restricted to the lighter areas (grey-scale) within the melt shard. BSE-EM image.* ***g)*** *BSE-EM image of a melt shard that contains a rounded darker area (blue arrows) that yields 99.46 wt% SiO_2 (see Table 8, MK 9b melt4 d). Sample 9b melt 4, 314.98 mblf.* ***h)*** *Vesiculated melt shard hosting areas (light grey) that show FeO contents of about 10 wt%, TiO_2 contents of about 2.5 wt%, and SiO_2 contents of about 50 to 53 wt% (blue arrows) (see Table 8 and Fig.34, MK 14 20h-rim). There are as well darker regions that exhibit 86 wt% SiO_2 (pink arrow) (see Table 8, MK 14 20d). BSE-EM image. Sample 14 20, 316.93 mblf.*

All analyzed melt shards are plotted in Fig. 33 in a total alkali versus silica diagram (TAS) after Le Bas et al. (1986) and reveal dacitic to rhyolitic compositions. The glass shards exhibit similar compositions to that of the melt clasts.

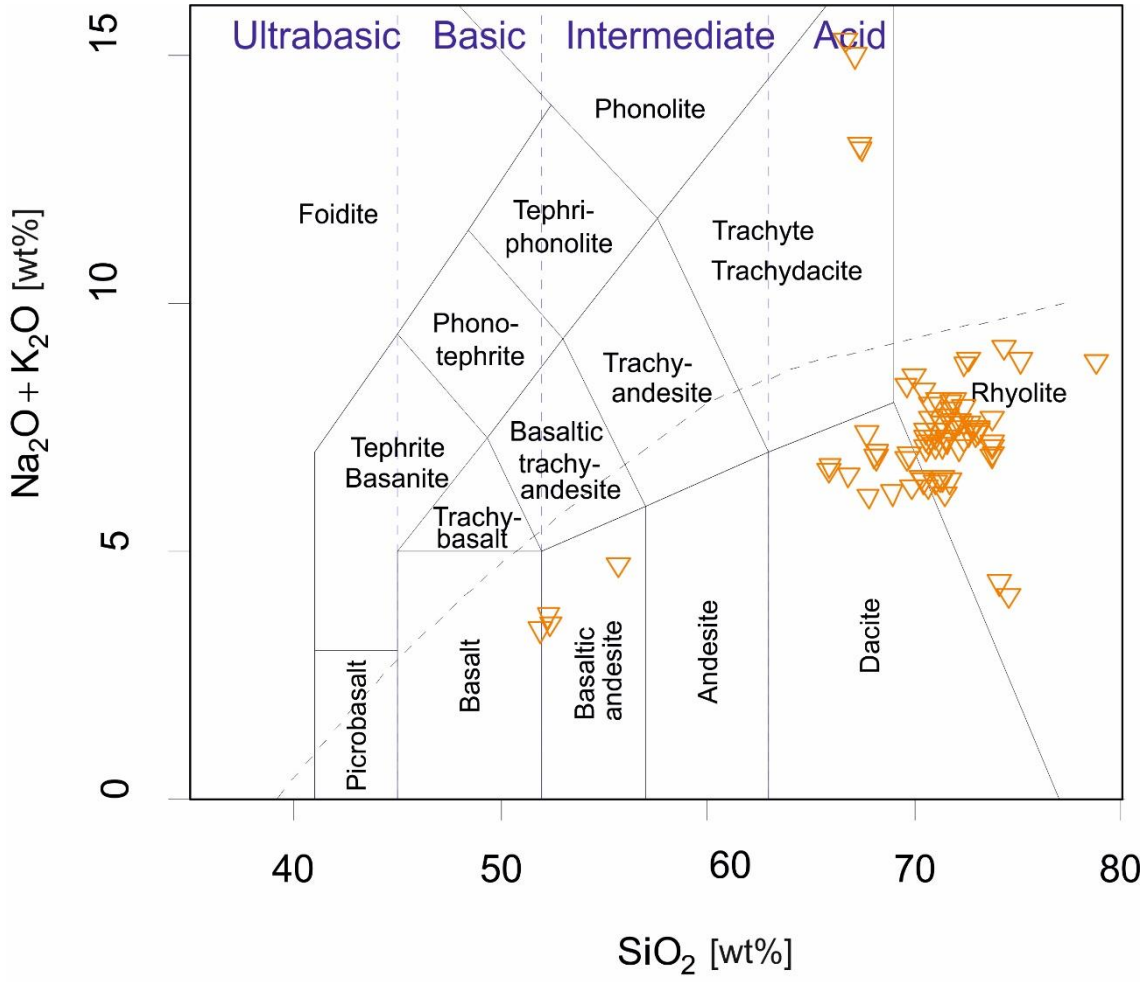

↑ ***Fig. 33.*** *Total alkali versus silica (TAS) plot after Le Bas et al. (1986) of all analyzed melt shards (point analyses). Generally, the majority yields dacitic to rhyolitic compositions. Some analyses of sample 14 show basaltic compositions (Sample 14 20 rim, Fig. 32h). Sample 9a 14 exhibits the highest compositions in K and Na (3.8-4.3 wt% and about 3 wt%, respectively; See Table 8). These measured glass shard plot in the trachyite section.*

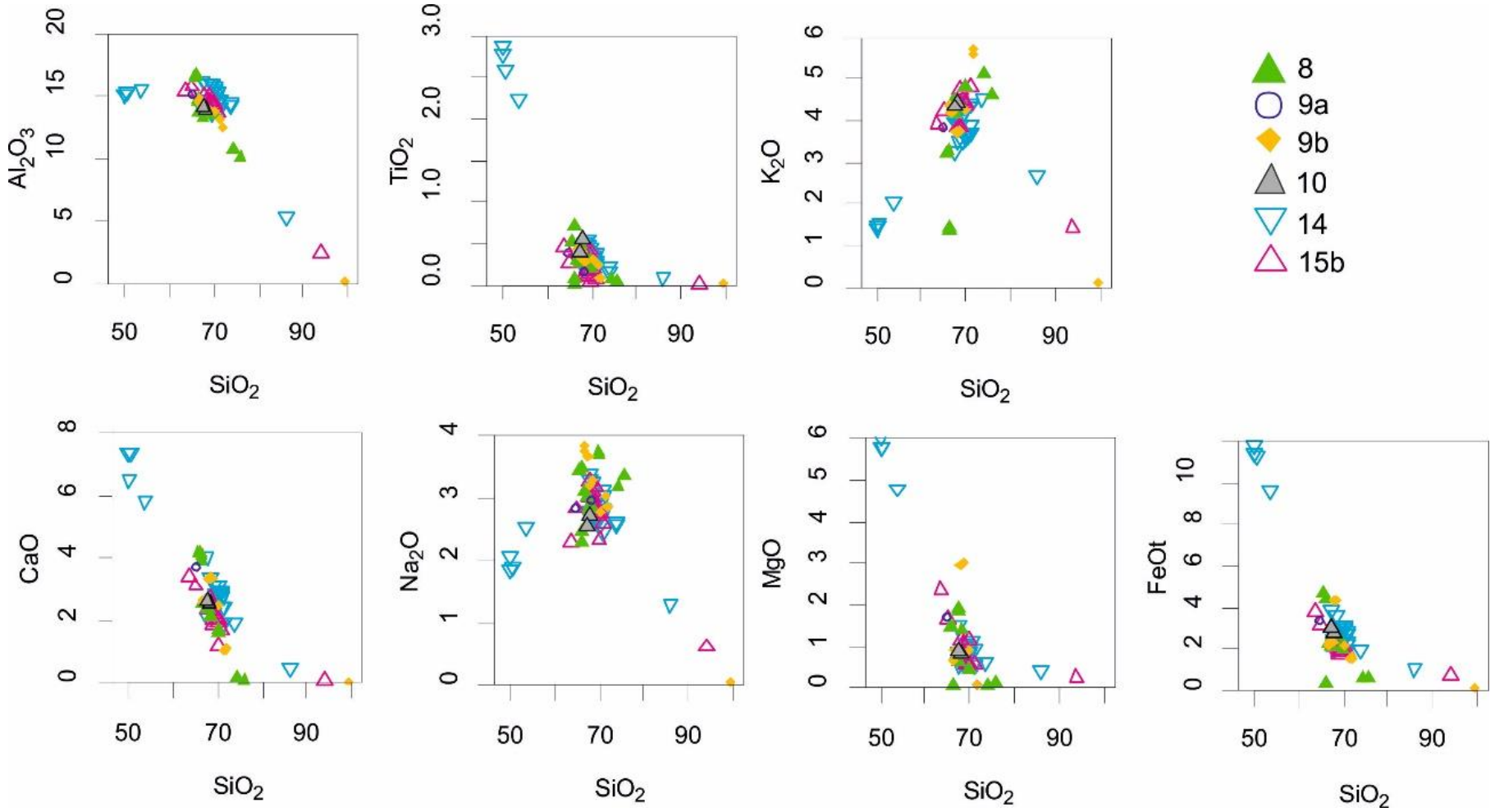

Fig. 34. *Multiple plots of major element contents versus SiO_2 (in wt%) of melt shards (point analyses). There is a population with significant systematic different compositions, displaying elevated CaO, FeO, TiO_2, and MgO concentrations (in wt%). These represent the lighter areas (BSE grey-scale) of sample 14 20 (see Fig 32h blue arrows).*

6.2.1.5 Spherules

Spherules occur just one meter below the top of the onset of the transition layer randomly distributed within the suevite. In general, they consist of glass either of homogeneous (e.g. Figs. 36a, c and Fig. 38h) or heterogeneous (e.g. Figs 36 e-h) composition. The majority reaches sizes ranging from 100 to 300 µm. The smallest spherule is about 20 µm in diameter (Sph 15b 02). A TAS plot after Le Bas et al. (1986) yields rhyolitic to dacitic compositions for most spherules (Fig. 35). But trachyandesitic and trachdacitic compositions can be documented as well.

Spinel or pyroxene crystal inclusions occur frequently. These are either located at the rim or within the core area (Figs. 36 e-f). Particularly two internally homogeneous spherules exhibit strong crystallized rims which can be divided into two sections (Figs. 36 a-d). The outer rim (5-10 µm wide) contains tiny (3 to 5 µm) high mass contrast phases possibly Cr- and Ni-bearing augite or diopside crystals embedded in glass that might be of the same composition as the rest of the spherule. The inner rim (10 to 20 µm wide) represents hollow space possibly hosting the same pyroxene crystals as there are in the outer rim, but with minor differences in chemistry. These crystals are slightly enriched in Al and Fe and contain as well Ni and Cr. Two spherules of this kind have been detected so far (MK 9b sph4 and MK 9b sph7). Even their chemical composition varies compared to the other spherules. They are enriched in Al_2O_3, TiO_2, CaO, FeO, and MgO and are depleted in SiO_2, K_2O, and Na_2O (see Fig. 36).

Compositionally heterogeneous spherules exhibit grey-scale color differences on BSE Images. Lighter areas on those images are usually enriched in FeO, MgO, CaO, and TiO_2 and are depleted in SiO_2 and K_2O. The expression of their compositional zonation is not uniform. There are spherules that are compositionally divided into a rim and core (Fig. 36h and Fig. 38b). The zone that is more enriched in mafic elements can vary. There are spherules where the core is enriched, but there are as well spherules that exhibit a higher concentration of mafic elements in the rim section. Other spherules do not show any rim-core divisions. Such samples exhibit flow patterns of different composition that can resemble into schlieren (Fig. 36g and Fig. 38f). Harker diagrams of zoned spherules are shown in Fig. 38. Definite chemical variations among different zones can be observed. As mentioned above lighter grey-scale colors (BSE) are enriched in heavier elements such as FeO, MgO, TiO_2, and CaO. These elements are as well negatively correlated to SiO_2. Darker regions (grey-scale BSE images) yield higher amounts of SiO_2, mostly ranging from 61 to 78 wt% SiO_2. On the contrary, lighter grey-scale regions exhibit 58 to 63 wt% SiO_2.

There are two spherules that have a small bubble that extends into the suevite from their peripheral area (Figs. 38 a-e, MK14 Sph 14 and MK 10 sph2). One bubble yields a rim that contains even more tiny (1-4 µm) bubbles possibly representing fluid inclusions (Fig. 38c).

Representative electron microprobe data of major elements of various spherules are given in Table 9. Chemically heterogeneous spherules among these analyses are MK 8 sph1, MK 9b sph6, MK 10 sph3, MK 14 14, and MK 15b 07 indicated by lighter and darker colors on BSE-Images. Spherules MK 9b sph4 and sph7 represent the most mafic ones with MgO contents of 8.43 and 11.46 wt% respectively. The amount of CaO yields 6.20 and 6.70 wt% and FeO comes to 6.73 and 7.95 wt%. These are the only spherules that exhibit basaltic compositions and contain the most pronounced crystal rim.

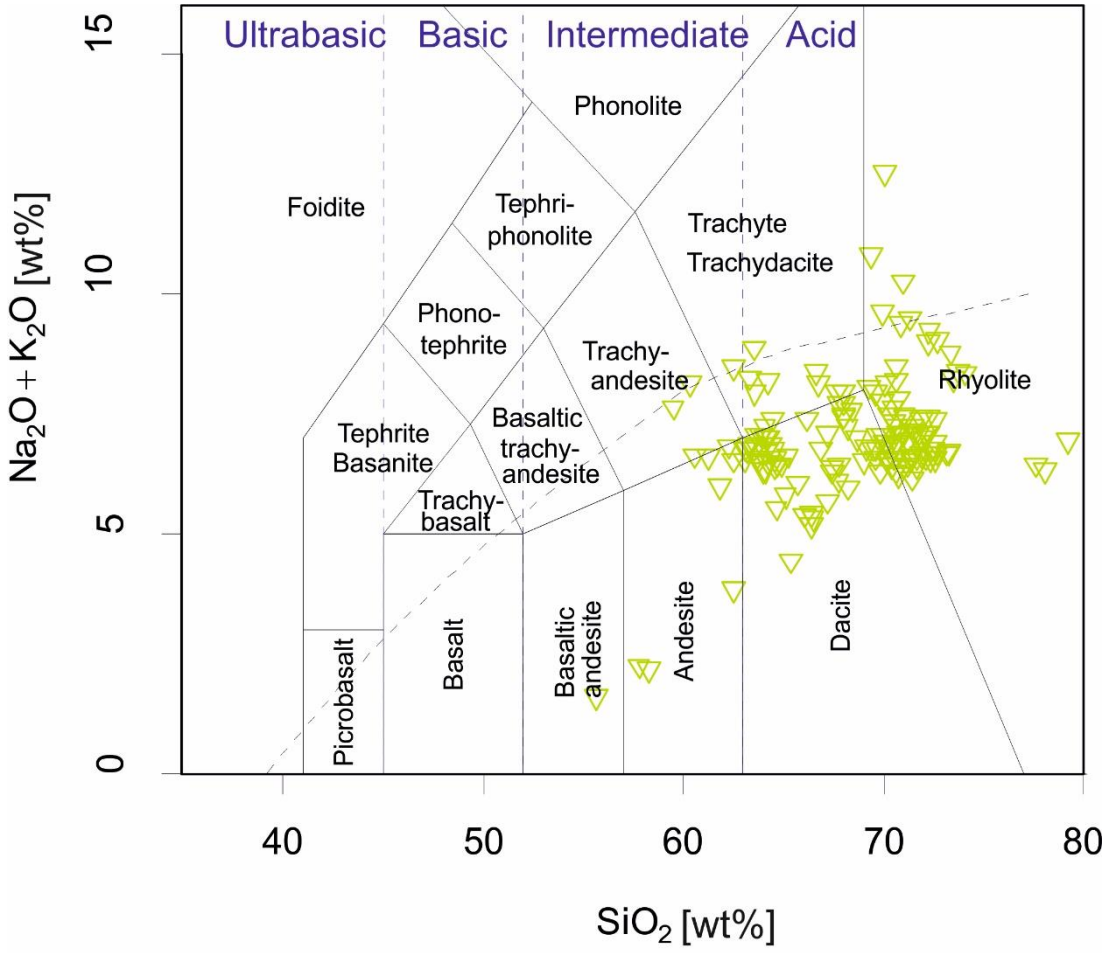

↑ ***Fig. 35***. *Total alkali-silica (TAS) diagram after Le Bas et al. (1986). 149 El'gygytgyn spherule analyses have been plotted. Three samples that yield basaltic compositions represent sample 9b shp4 (two analyses) and sph7.*

Table 9. *Representative electron microprobe data of diverse El'gygytgyn impact spherules. MK 8 sph1, MK 9b sph6, MK 10 sph3, MK 14 14, and MK 15b 07 are heterogeneous spherules hosting lighter and darker regions (BSE-grey-scale). MK 9b sph4 and sph7 represent spherules with the most pronounced crystal rim (Fig. 36 a-d). Their chemistry differentiates from the rest, representing the most mafic spherules of all analyzed spherules.*

Sample	***MK 8***	***MK 8***	***MK 8***	***MK 9a***	***MK 9b***	***MK 9b***	***MK 9b***	***MK 9b***	***MK 9b***	***MK 10***	***MK 10***	***MK 10***	***MK 14***	***MK 14***	***MK 15b***	***MK 15b***	***MK 15b***
Point	sph1-d	sph1-h	sph3	16_07	sph4	sph6-h	sph6-d	sph7	sph14	sph3-h	sph3-d	sph5	14p_h	14p_d-rim	02_sph02	07_sph02	07_sph rim 05
Depth [mblf]	315.50	315.50	315.50	315.02	314.98	314.98	314.98	314.98	314.98	315.19	315.19	315.19	316.93	316.93	317.07	317.07	317.07
Size µm]	270	270	500	320	320	300	300	240	80	240	240	75	210	210	20	150	150
Shape	ovoid het	ovoid het	ovoid het	spher hom	ovoid hom	ovoid het	ovoid het	ovoid hom	ovoid het	ovoid het	ovoid het	spher hom	ovoid het	ovoid het	spher het	spher het	spher het
Info	*dark*	*light*	-	-	*crystal rim*	*light*	*dark*	*crystal rim*	*Ti-rich-est*	-	*Si-rich-est*	-	*light*	*dark*	-	*dark*	*light*
SiO_2	70.17	59.16	72.12	71.58	57.48	63.23	69.23	55.81	64.58	71.93	78.71	61.97	67.46	70.25	64.52	66.53	60.02
Al_2O_3	13.59	15.60	15.09	14.98	16.68	12.93	13.94	15.61	14.65	14.94	10.86	11.06	16.10	14.98	15.99	15.13	13.14
Cr_2O_3	<0.02	0.08	<0.02	<0.02	0.08	0.15	<0.02	0.14	0.05	<0.02	<0.02	0.12	0.05	<0.02	<0.02	0.06	0.06
TiO_2	0.42	0.69	0.24	0.34	0.83	0.42	0.22	0.95	2.31	0.33	0.07	0.38	0.44	0.36	0.31	0.49	0.48
K_2O	5.22	3.68	4.42	3.80	0.45	3.61	5.02	0.35	3.60	4.11	4.21	3.95	3.27	3.72	4.67	4.39	3.16
CaO	0.56	4.86	2.30	2.28	6.29	4.54	1.48	6.70	3.79	2.62	1.17	3.22	4.02	2.74	3.15	2.35	4.00
FeO[a]	1.59	6.54	2.05	2.43	6.73	6.31	1.41	7.95	4.91	2.37	1.13	7.02	3.92	2.54	2.82	3.74	7.89
MnO	0.02	0.17	0.06	0.06	0.12	0.11	0.06	0.17	0.14	0.04	0.08	0.11	0.14	0.07	0.11	0.05	0.13
Na_2O	2.68	3.92	3.00	2.83	1.69	3.52	3.60	1.26	2.98	3.06	2.70	2.17	2.80	2.58	2.39	3.72	3.41
MgO	0.47	4.82	1.11	1.28	8.43	4.04	0.91	11.46	2.10	1.07	0.50	6.87	1.49	0.85	0.93	3.36	6.91
NiO	n.m.	n.m.	n.m.	0.03	n.m.	n.m.	n.m.	n.m.	n.m.	n.m.	n.m.	n.m.	0.02	0.04	<0.01	0.10	0.26
Total	94.72	99.53	100.38	99.61	98.77	98.85	95.87	100.39	99.10	100.47	99.43	96.88	99.71	98.12	94.88	99.92	99.46

[a] All iron as FeO; n.m. = not measured; spher = spherical; hom = homogeneous; het = heterogeneous; Light and dark are referred to BSE grey-scale colors; All analyses in wt% and measured by EPMA.

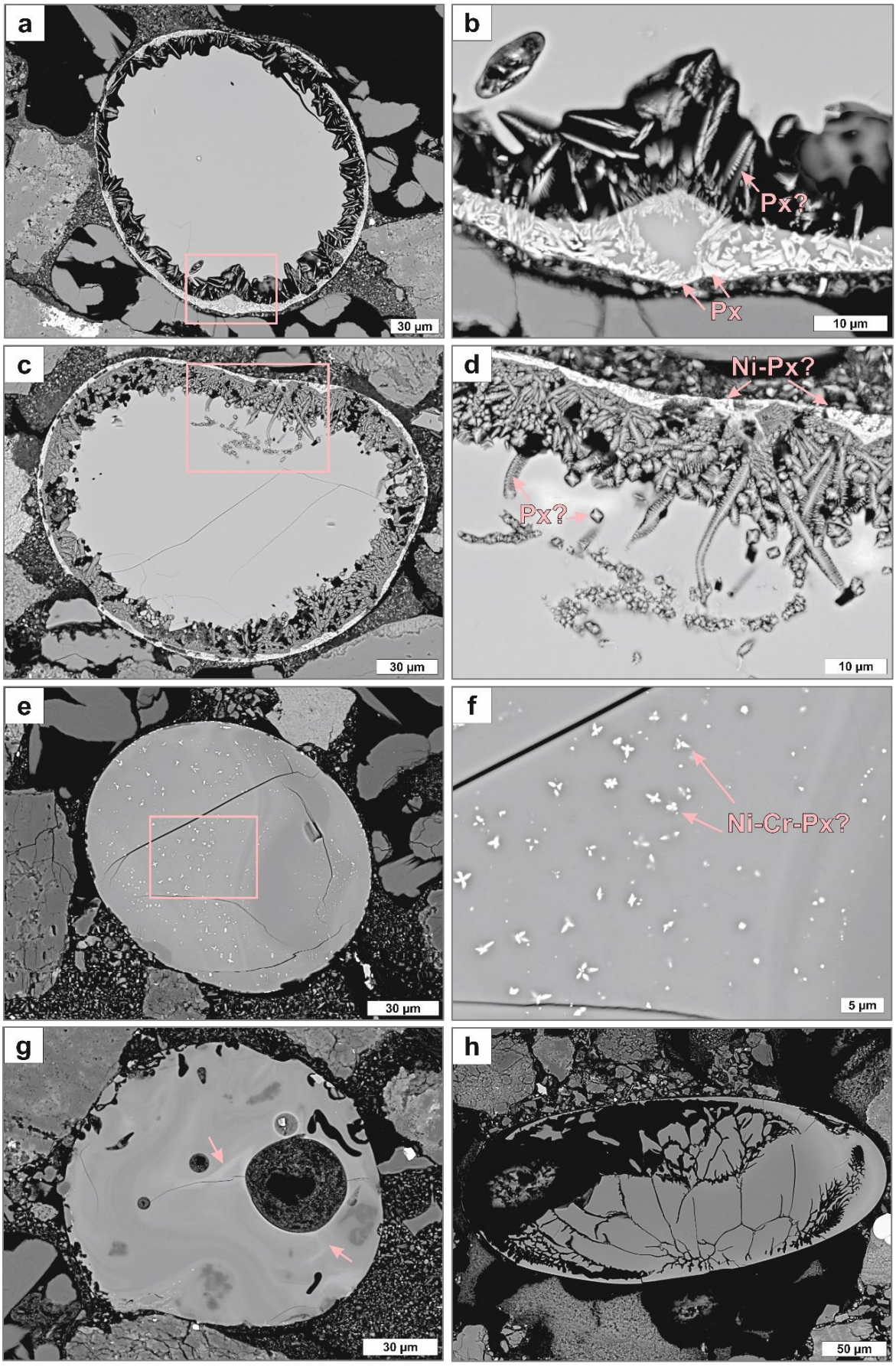
a
30 µm
b
Px?
Px
10 µm
c
30 µm
d
Ni-Px?
Px?
10 µm
e
30 µm
f
Ni-Cr-Px?
5 µm
g
30 µm
h
50 µm

→ ***Fig. 36. a)*** *BSE-EM image of a spherule with a pronounced crystallite rim. Note the crystallite in the center. Sample 9b sph 4, 314.98 mblf.* ***b)*** *The same image under higher magnification (pink rectangle in a) displaying the pyroxene (Px) crystals, which are Cr- and Ni-bearing. Note the division into an outer and an inner rim. BSE-EM image.* ***c)*** *Ovoid-shaped spherule that yields a thick rim of prismatic crystals. The crystals are of the same chemistry as the ones in a, and b respectively. Note that the pyroxene prisms project inward suggesting that they grew from the outside to the inside. BSE-EM image. Sample 9b sph 7, 314.98 mblf.* ***d)*** *Higher magnification of the same image displaying the crystallized rim of the same spherule. The high mass contrast phases of the outer rim might be pyroxenes (diopside or augite) that contain Ni. BSE-EM image.* ***e)*** *Crystal bearing ovoid-shaped spherule with internal flow fabric (schlieren). Note the crystals accumulate in the lighter areas. BSE-EM image. Sample 9b sph15, 314.98 mblf.* ***f)*** *The same image (pink rectangle in e) under higher magnification showing the 2-4 µm crystals that yield pyroxene compositions containing Ni as well as Cr. BSE-EM image.* ***g)*** *BSE-EM image of a spherical-shaped spherule with internal flow fabric (schlieren) containing several holes. The lighter schlieren host tiny objects that might represent crystal seeds (pink arrows). Sample 9b sph12, 314.98 mblf.* ***h)*** *Ellipsoidal spherule with internal fracture patterns. Almost half of the spherule contains hollow space. Note the lighter rim on the far right. BSE-EM image. Sample 10 sph16, 315.19 mblf.*

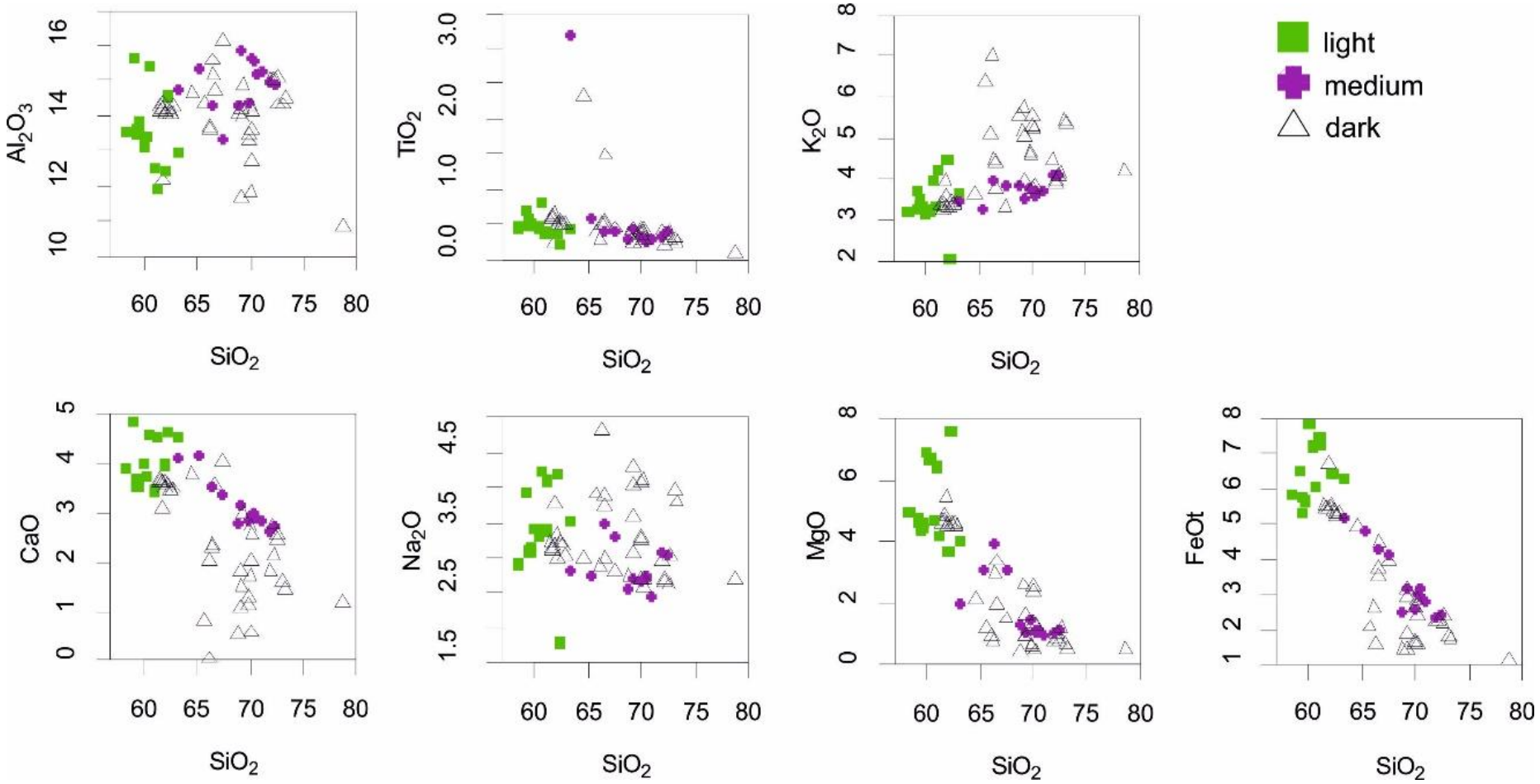

Fig. 37. *Harker diagrams of heterogeneous spherules (analyses in wt%). Light areas (BSE grey-scale) are definitely enriched in heavier elements. Darker spots within the spherules exhibit high SiO_2, K_2O, and Na_2O concentrations.*

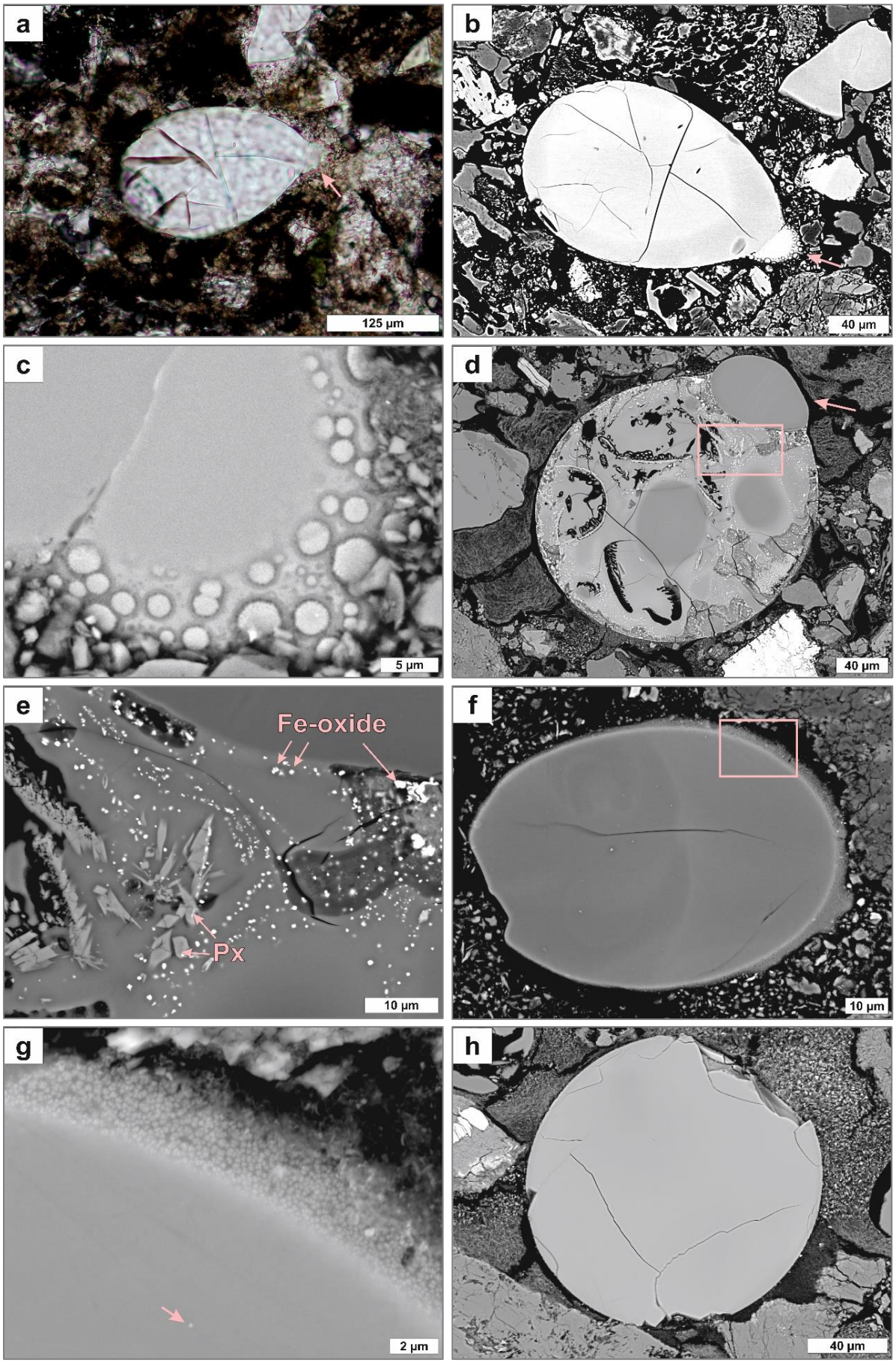
a
125 µm
b
40 µm
c
5 µm
d
40 µm
e
Fe-oxide
Px
10 µm
f
10 µm
g
2 µm
h
40 µm

→ ***Fig. 38. a)*** *Microphotograph of a teardrop-shaped spherule that yields an extension on the far right. Plane-polarized light, optical microscopy. Sample 14 14, 316.93 mblf.* ***b)*** *BSE-EM image of the same spherule revealing a better view of the extension (pink arrow). Note the dark rim on the right side.* ***c)*** *The extension from b (pink arrow) under higher magnification. Note the tiny (1-4 µm) bubbles at the rim. BSE-SEM image.* ***d)*** *Spherule yielding various internal textures and displaying a spherical extension on the upper right (pink arrow). There are various crystallites within the spherule restricted to certain areas. Note the arche-shaped cavities. BSE-EM image. Sample 10 sph2, 315.19 mblf.* ***e)*** *The same spherule under higher magnification (pink rectangle from d) displaying the crystallites. The tiny (< 3 µm) high mass contrast phases represent Fe-oxides and the bigger crystals (> 5 µm) might be pyroxenes (augite or diopside). BSE-EM image.* ***f)*** *Ovoid-shaped spherule displaying a compositional heterogeneity which becomes visible due to different grey-scale colors. The left half is darker and exhibits a flow pattern. The rim on the right displays a pronounced rim. BSE-EM image. Sample 9b sph10, 314.98 mblf.* ***g)*** *The rim of the same spherule under higher magnification (pink rectangle from f) showing < 0.5 µm crystal seeds. Note the crystallite within the spherule (pink arrow). BSE-EM image.* ***h)*** *BSE-EM image of a strongly spherical-shaped spherule that is internally homogeneous. Sample 9b sph9, 314.98 mblf.*

6.3. Bulk Rock Geochemistry

Neutron activation analyses were performed at the University of Vienna on 13 samples, of which thin sections were prepared as well.

6.3.1 Minor and Trace Elements

The data of all measured bulk rock samples via INAA are given in Table 10. Concentrations for Ba generally vary between ~ 337 and 501 ppm. Sample KME11, yields the highest Ba contents with ~816 ppm, probably due to local contamination, as the sample hosts large lithic clasts. Contents in the suevite vary between ~118-150 ppm for Rb, and ~124-234 ppm for Sr. The abundances of the siderophile elements Co, Ni, and Au exhibit variations between ~3.81-6.92 ppm for Co, ~8-26 ppm for Ni, and ~1.3-2.6 ppb for Au. There is one sample (KME13) that exhibits an Au concentration of 16 ppb. Chalcophile element contents of Cr and Zn vary between ~18-57 ppm for Cr, and ~47-72 ppm for Zn. Iridium contents are below the detection limit of about 1.4 ppb. Figure 40 shows a chondrite-normalized multielement (spider) diagram (normalization factors from Thompson 1982) displaying the trace element patterns for the El'gygytgyn transition layer. The diagram reveals high concentrations of Rb, Th, and K, which are the more mobile large ion lithophile (LIL) elements. Tantalum and Sr contents are depleted.

6.3.2 Rare Earth Elements

Chondrite-normalized rare earth element (REE) abundance patterns (normalization factors from Nakamura 1974) (Fig. 39) exhibit negative Eu anomalies for all suevite samples. Light rare earth elements (LREE) are enriched.

Table 10. *Major, minor, and trace element contents of whole rock samples from transition layer of the El'gygytgyn impact structure measured by INAA. Analyses in ppm (except as noted).*

Sample	***KME01***	***KME02***	***KME03***	***KME04***	***KME05***	***KME06***	***KME07***	***KME08***	***KME09***	***KME11***	***KME12***	***KME13***	***KME14***
Depth [mblf]	311.58	311.91	313.02	313.64	313.78	314.27	314.62	315.50	314.99	315.59	315.82	315.96	316.93
Na (wt%)	2.22	2.54	2.33	2.24	2.14	1.95	2.13	2.21	2.21	2.18	2.19	1.92	2.43
K (wt%)	2.71	3.05	3.08	2.68	2.92	2.73	2.81	2.97	3.23	3.29	2.85	2.45	2.89
Sc	7.37	9.78	7.81	9.6	10.3	8.86	6.64	7.85	7.71	5.88	8.22	6.64	8.99
Cr	40.4	57.1	36.5	26.1	22.3	26	40.5	39.0	33.6	23.9	26.9	18.2	32.4
Fe (wt%)	1.95	3.07	2.08	1.92	2.75	2.01	1.97	2.14	2.14	1.77	2.23	1.84	2.32
Co	4.79	6.92	4.71	4.18	6.11	4.41	4.82	5.25	5.05	3.81	5.25	4.45	5.23
Ni	16.7	26.4	17.9	17.7	<25	10.8	11.8	18.0	15.8	12.1	14.8	8.2	13.1
Zn	50.7	65.7	59.6	57.8	72.5	58.3	51.8	56.4	55.6	50.6	58.8	46.8	61.4
Ga	4.04	20.4	5.73	4.08	5.71	7.97	6.00	<5.3	5.48	<5.5	11.2	7.50	12.5
As	7.97	10.2	10.3	8.39	10.1	8.56	10.3	12.7	9.95	11.1	9.4	6.74	12.8
Se	<1.6	<1.9	<1.6	<1.8	<1.9	0.36	<1.7	<1.3	<1.7	<1.1	<1.8	<1.6	<1.7
Br	<1.1	<1	<1.1	<1.1	<1.1	<0.8	0.4	0.5	<1.1	<1.1	<1.0	<0.3	<1.2
Rb	118	139	150	119	142	125	142	135	145	139	135	131	147
Sr	169	234	196	180	225	139	186	178	196	229	162	124	195
Zr	213	243	231	292	286	216	230	235	189	197	218	203	241
Sb	1.07	1.02	1.24	0.98	1.22	2.02	1.19	1.23	1.1	1.08	1.19	2.11	1.17
Cs	8.21	10.1	9.3	8.78	6.23	8.54	10.7	8.4	9.13	8.55	10.5	8.14	9.06
Ba	337	448	454	403	501	365	464	480	441	816	391	352	477
La	30.4	34.3	31.8	31.8	44.9	34	31.8	29.8	30.3	38.6	32.1	33.1	34.8
Ce	58.2	90.4	63.9	61.7	64.3	65.5	60.9	58.6	60.9	65.3	60.9	61.7	65.6
Nd	21.4	34.9	22.8	25.2	24.7	25.1	22.5	22.6	23.3	22.8	24.1	22.9	25.5
Sm	4.13	5.68	4.8	5.11	5.64	4.93	4.46	4.66	4.65	4.92	5.1	4.55	5.60
Eu	0.84	0.98	0.92	1.03	0.98	0.83	0.80	0.87	0.88	0.83	0.89	0.80	0.94
Gd	3.71	4.07	4.05	4.57	4.70	4.33	3.34	3.69	3.71	4.07	3.97	3.69	4.31
Tb	0.58	0.82	0.70	0.76	0.74	0.71	0.59	0.65	0.65	0.69	0.68	0.6	0.77
Tm	0.32	0.43	0.43	0.5	0.49	0.45	0.30	0.40	0.36	0.37	0.38	0.36	0.39
Yb	2.28	2.79	2.36	2.91	2.44	2.55	2.1	2.20	2.4	2.28	2.38	2.34	2.77
Lu	0.36	0.47	0.39	0.48	0.42	0.4	0.36	0.38	0.37	0.36	0.39	0.38	0.43

Table 10. *Continued. Major, minor, and trace element contents of whole rock samples from transition layer of the El'gygytgyn impact structure measured by INAA. Analyses in ppm (except as noted)*

Hf	4.95	5.74	5.83	6.49	6.79	5.06	5.06	4.94	4.56	4.54	5.05	4.67	5.24
Ta	0.66	0.91	0.87	0.8	0.8	0.75	0.82	0.77	0.78	0.78	0.81	0.84	0.81
Os (ppb)	<719	<423	<702	<787	<777	<374	<724	<632	<825	<684	<479	<146	<505
Ir (ppb)	<1.3	<1.7	<1.3	<1.5	<1.5	<1.3	<1.5	<1.1	<1.4	<0.9	<1.5	<1.3	<1.4
Au (ppb)	<2.0	<1.5	<1.9	<2.1	<2.0	1.3	<2.0	1.3	<2.1	2.6	1.5	16	1.5
Th	12.9	15.3	15.9	12.5	14.9	13.8	14.8	14.2	15.1	15.4	14.2	16.8	14.8
U	2.73	3.94	3.92	2.86	3.64	3.42	3.65	4.41	3.52	3.93	3.81	3.68	4.36

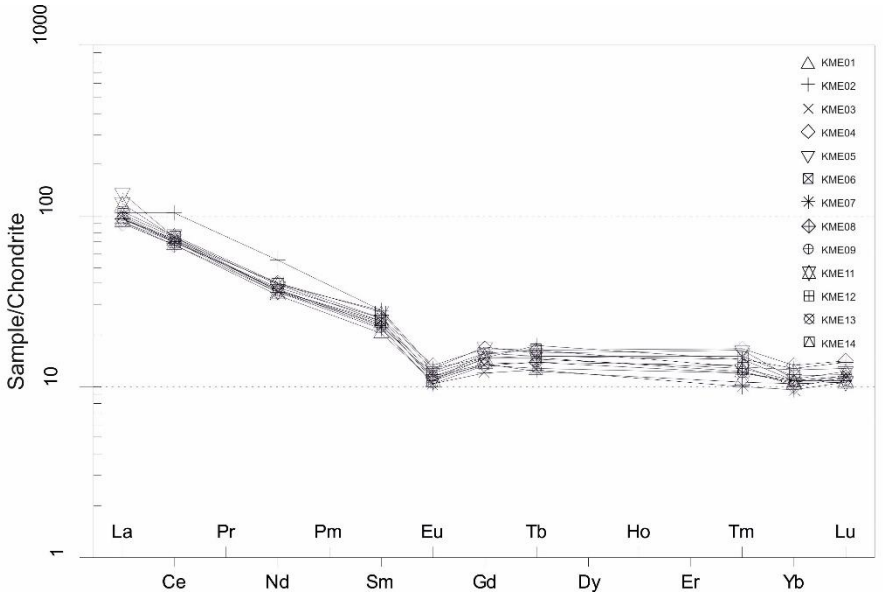

Fig. 39. *Chondrite-normalized (Normalization factors from Boynton 1982) rare earth element distribution patterns showing an Eu-anomaly and an enrichment of the LREE (light rare earth elements).*

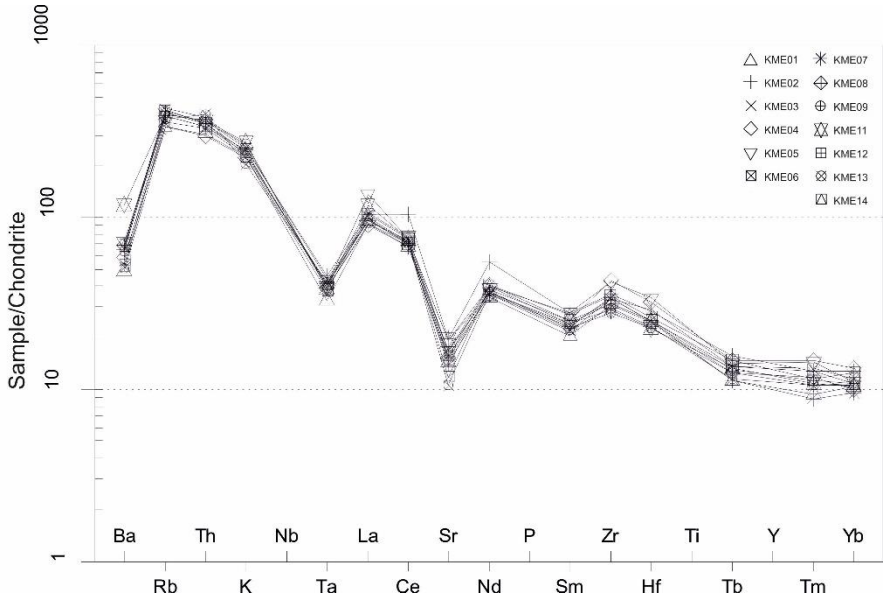

Fig. 40. *Multielement patterns from rocks from the El'gygytgyn transition layer that are chondrite normalized (Thompson 1982). The diagram reveals higher abundances of Rb, Th, and K, and depletions of Ta and Sr.*

6.4 Siderophile Elements Abundances and the Implications for a Meteoritic Component

The detection of meteoritical components in impactites represents a major challenge. Such questions can only be determined by using elements that have high abundances in meteorites and low abundances in terrestrial crustal rocks. Siderophile elements, such as Ni, Cr, and Co have often been used and their interelement ratios act as an efficient discriminator. However, there exists a great number of meteorite groups and types that contain varying siderophile element contents. The three main types are stony meteorites, iron meteorites, and stony-iron meteorites. Chondrites and iron meteorites show distinctly higher siderophile element concentrations in impact melts, wherefore achondritic projectiles have lower siderophile element abundances and are more difficult to discern (e.g., Koeberl 1998). Concerning the interelement ratios of Ni, Cr, and Co, there is the possibility to distinguish between chondrites (stony meteorites) and iron meteorites if the meteoritic contribution is > 0.1 % (Koeberl 1998). Chondrite show high Cr concentrations (about 0.026 wt%), whereas the Cr content in iron meteorites is much more variable, but mostly about 100 times lower than those of chondrites. A detailed study of the target rocks is however, of great importance, due to the possibility of high indigenous components. Consequently, mixing calculations can be done to determine the relative proportions of the target rock types that constitute the impact rocks. The substraction of the siderophile element contents of the target rocks from those of the impact melt rocks, may generate a corrected meteoritic component.

Ni, Cr, and Co interelement ratios of the bulk rock samples determined by INAA and the spherules measured by EPMA of the El'gygytgyn transition layer have been plotted in Fig. 41 a, b, and c. For some of the El'gygytgyn transition layer spherules, only Ni and Cr concentrations have been measured (Fig. 41c). For comparison, the El'gygytgyn target rocks, the spherules of the El'gygytgyn impactite drill core, and chondrite data have been plotted as well. The El'gygytgyn target rock data were determined by EPMA and are from Pittarello et al. (2013) and the spherule data were obtained by Wittmann et al. (2013) analysed by LA-ICP-MS and EPMA. The data for different averaged chondrite groups is from Tagle and Berlin (2008) (Fig. 41 a-c) and from Jarosewich (1990) (Fig. 41d).

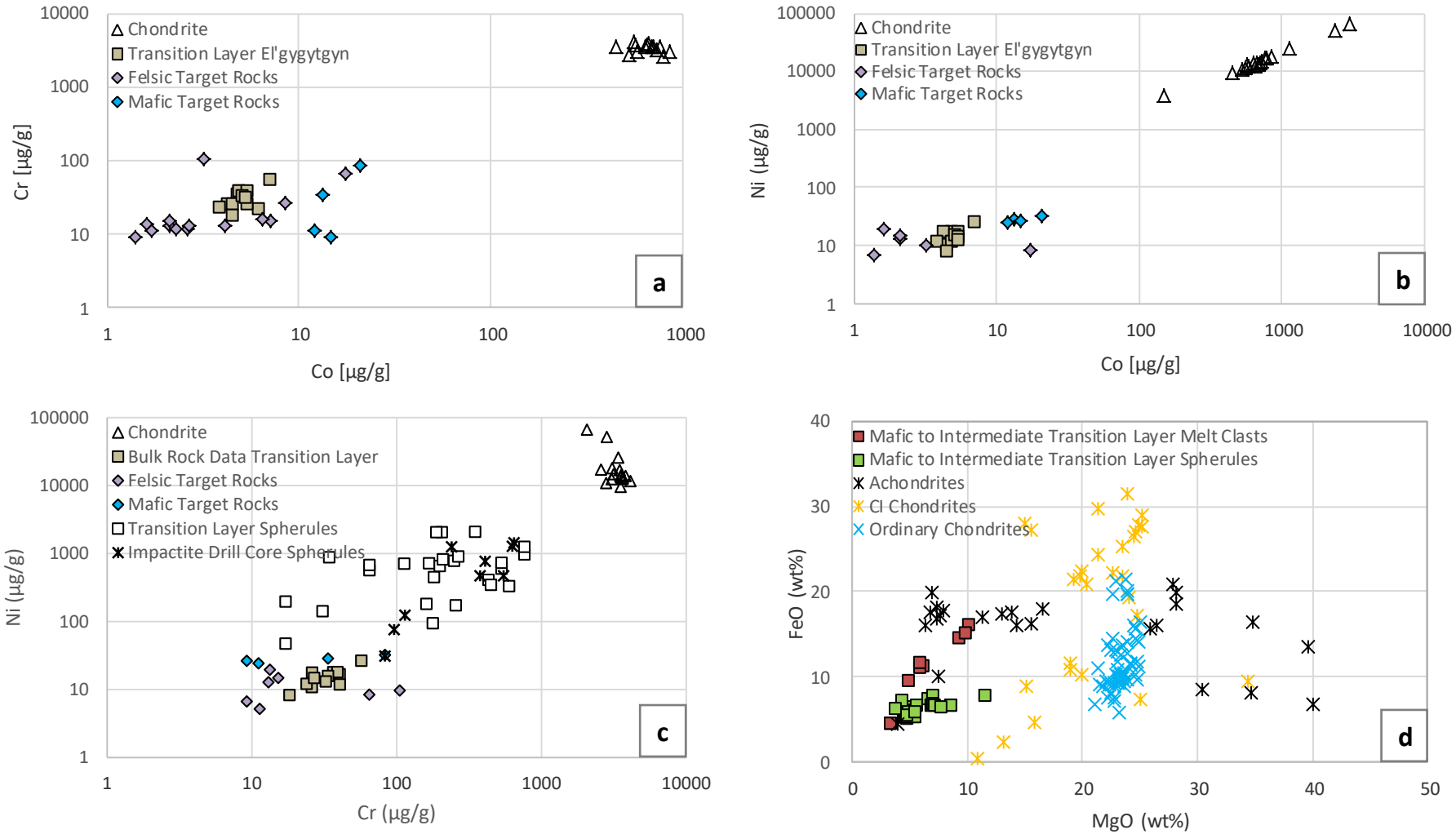

Fig. 41 *Plots of* ***a)*** *Cr versus Co,* ***b)*** *Ni versus Co,* ***c)*** *Ni versus Cr, and* ***d)*** *FeO versus MgO. Spherules from the El'gygytgyn impactite drill core were determined by Wittmann et al. (2013) by LA-ICP-MS and EPMA. El'gygytgyn target rock data are from Pittarello et al. (2013) and Chondrite data are from Tagle and Berlin (2008) for the Ni. Cr, and Co plots and from Jarosewich (1990) for the FeO versus MgO diagram. The data from the El'gygytgyn transition layer for Ni-Cr-Co interelement ratios (grey squares) represent bulk rock analyses measured by INAA. Impact spherule data from the El'gygytgyn transition layer (white, orange, and green squares) have been determined via EPMA.*

The bulk rock data from the El'gygytgyn transition layer (grey squares) show similar Ni, Cr, and Co interelement ratios as the felsic El'gygytgyn target rocks. However, the spherules from the El'gygytgyn transition layer exhibit Ni and Cr concentrations (Fig. 41c), that do not correspond to target rock values. Compared to the impactite drill core spherules from Wittmann et al. (2013), some of the transition layer spherules report higher Ni concentrations. Figure 41d shows a FeO versus MgO plot of mafic spherules and mafic impact melt clasts from the El'gygytgyn transition layer. The Mg and Fe abundances exhibit positive correlations for the spherules and the impact melt clasts (with R=0.86 and R=0.95, respectively). The MgO and FeO contents of the intermediate to mafic spherules reach a maximum of 11.5 wt% and 8 wt%, respectively. The intermediate to mafic andesites and basalts from the target rocks, however, show maximal MgO concentrations of about 4 wt% and for FeO about 8 wt% (Pittarello et al. 2013).

CHAPTER 7

Discussion

7.1. Petrography and Geochemistry

7.1.1 Mineral Clasts in the Suevite

Mineral clasts within suevite match the lithologies of the target rocks in terms of their mineralogy. Quartz and feldspar clasts and grains are dominant. Feldspar occurs in various stages of alteration. The majority of those feldspar grains exhibit sericitization and carbonation demonstrating that the rocks from the transition layer were penetrated by fluids. Also the abundant occurrence of zeolites indicates hydrothermal alteration.

Quartz grains are the most common mineral and exhibit shock features such as PFs and PDFs. These features can be observed within the whole section of the transition layer mostly randomly distributed only within the suevite matrix. They exhibit usually four to six non-decorated sets of PDFs. Shocked quartz grains within melt or volcanic fragments have not been documented so far from the transition layer of El'gygytgyn drill core. There is no accumulation of quartz grains with PDFs within certain areas of the drill core section. They occur even at the beginning of the onset of the transition layer. The majority of the quartz grains are not shocked and the occurrence of PDFs represents the exception rather than the rule. However, SEM studies of these PDFs have revealed uncommon and interesting microstructures which have never been described in any other impact structure. The PDFs are locally deformed, forming about 1 to10 µm broad open microbasins within the crystal. These appear similar to pull-apart structures, just in micro-dimensions. After Pittarello et al. (2013), these deformation features might have formed when the ambient temperature in the suevite was sufficiently high enough allowing quartz to deform in a ductile regime.

Feldspar grains are represented by alkali-feldspar compositions (Or_{04} to Or_{98}), matching those compositions that were reported by Koeberl et al. (2013) and reflecting the felsic character of the target rocks. Occasionally plagioclase crystals occur as parts of lithic fragments. These are mostly fragmented and appear fresh and exhibit polysynthetic twining. The arrangement of these clasts (Fig. 16 e-f) could indicate that they were derived from one single grain and/or volcanic fragment. The rare occurrence of plagioclase, mostly within volcanic clasts, would correspond to the abundance of basalt and andesites in the target rocks.

Amphibole and pyroxene clasts are relatively common and exhibit constant chemical compositions. Amphiboles were classified as ferro-tschermakites that are usually altered at their edges to Fe-oxide and/or biotite and occur mostly as part of volcanic fragments and to a lesser extend as well in the suevite matrix. Pyroxene grains however, are primary bound to the suevite matrix. Just one strongly vesiculated blackish melt clast was hosting augite crystals. Compared to ones within the suevite, these pyroxenes show substantial alteration features at their edges (Figs. 20 e-f). The pyroxenes within the suevite exhibit augite- to diopside compositions and appear fresh, rarely exhibiting alteration features. These might reflect the greater stability of pyroxenes over amphiboles when it comes to weathering and hydrothermal alteration.

Phyllosilicates are represented by biotite, chlorite, and muscovite. They are randomly distributed within the suevite. Chlorite mostly represents secondary phases, occurring as an alteration product of biotite. Biotite and a few primary chlorites even exhibit kink bands. These result from gliding within the crystal combined with an external axis of rotation. Such features are not specifically diagnostic for shock, they could also form due to tectonic deformation. Narrow widths, a high kink angle, and a high frequency of the kink bands may indicate an impact-related formation (Hörz 1970). The kinked biotites of the El'gygytgyn drill core transition layer show kink band widths ranging from ~10 to 20 µm, mostly exhibiting two conjugate sets (Figs. 24 c-d). These features and the occurrence of other impact related features in close vicinity to the kinked biotites and chlorites (e.g., PDFs and spherules) might be in favor of an impact origin.

7.1.2 Lithic Fragments in the Suevite

Lithic fragments in the suevite are mostly of volcanic origin. Under the optical microscope plagioclase laths and pyroxene (augite) crystals reveal subophitic textures that are diagnostic for basalts. Nearly all volcanic clasts show pronounced alteration, suggesting that they might be fragments of the Late Cretaceous target rocks. Other fragments seem to have been affected by partial melting. Such host mineral clasts (rutile) are already partially resorbed and are embedded in a flow structure (schlieren) of feldspathic compositions. It is even possible to discern relicts of former crystals within those flow structures. These fragments appear fresh and it is difficult to determine whether or not they formed due to impact melting.

7.1.3. Melt Fragments in the Suevite

Melt fragments within the suevite are represented by at least three populations, as described in Chapter 6. (1) White- to greyish vesiculated clasts, (2) denser blackish fragments that locally

contain vesicles, and (3) brown- to greenish melt clasts that can host former crystal relicts. The distinction between volcanic and impact melt is not precisely determinable in the case of the El'gygytgyn impact structure, because of the silicic volcanic origin of the target rock. Previous works on the El'gygytgyn structure (e.g., Pittarello et al. 2012) used the following possible distinction criteria: (a) the occurrence of shocked grains, (b) the porosity, (c) the freshness and (d) the composition.

In the case of the rocks from the transition layer shocked grains (a) such as quartz and/or feldspar have not been detected within melt fragments.

Abundant vesicles (b) within melt clasts might suggest an impact origin, because previously investigated samples form the target do not show such features (e.g. Raschke et al. 2013). Pittarello et al. (2013) generally considers highly vesiculated melt fragments to be of impact origin, because porous glass samples were detected at the crater in surface outcrops, and were classified as impact melts (Gurov and Koeberl 2004; Pittarello and Koeberl 2013).

Recently formed melt fragments might be fresh (c), in contrast to the target rocks that formed in the Late Cretaceous. However, many melt fragments, especially those that are vesiculated, host secondary minerals (K-Na-Ca aluminosilicates), rarely exhibiting even devitrification textures. These melt fragments, still fresher than the target rocks, might have experienced pervasive impact-induced postimpact hydrothermal alterations

Generally, the composition of melt fragments (d) is a useful tool distinguishing between different melts of different origins. Target rocks that are composed of different lithologies would generate impact-induced melt fragments that exhibit mixed compositions or could be of the composition of a specific lithology within the target. At El'gygytgyn the overall lithology's composition is felsic, with minimal local variations wherefore the melt fragments would exhibit felsic compositions as well. As a consequence, the determination between impact and volcanic formation cannot be made on the basis of composition. However, there are various melt fragments that contain areas that are enriched in more mafic elements. Some even show basaltic compositions (see Fig. 29h, Fig. 30, and Fig. 31). There are two possibilities that could explain these features. The first explanation would be that basaltic material from the target rock was melted during the impact event and incorporated in some melt clasts. Basaltic rocks are even cropping out at the top of the volcanic sequence of the target rock. The second one would restrict such a formation to an immiscibility effect. The molten rock would have had no time to homogenize and different melts are mixed in the form of droplets. Some of these areas contain MgO and FeO contents that to not correspond to those of the target rocks such as basalts and

andesites. The MgO contents in the transition layer melt clasts show a maximum of 10 wt% and the FeO contents of about 16 wt%. In Fig. 41.d FeO is plotted against MgO including the mafic spots of the melt clasts, impact spherules from the transition layer as well as carbonaceous chondrite (CI-Chondrite), ordinary chondrite, and achondrite compositions. Based on this observation, an achondritic projectile could have contributed to such MgO-FeO compositions.

7.1.4. Spherules in the Suevite and the Possible Contribution of a Meteoritical Component

Spherules that form in an impact event are thought to result from condensation of vaporized target rock and impactor, or as impact melt droplets that are formed ballistically (Glass and Burns 1988, Smit 1999, Simonson and Glass 2004). The spherules that formed due condensation are called “microkrystites”. These are round and contain crystallites of pyroxene and/or Ni-rich spinel. These are most abundant in distal ejecta layers. “Mikrotektites” are spherules that represent impact melt droplets. These are usually glassy and variable in shape. They may even contain relicts of target rock debris and are most abundant in proximal ejecta layers (Smit 1999). Mikrokrystites might be sph15 and sph4 from sample 9b (Figs. 36 a-f). Spherules that are mikrotektites might be sph16 from sample 10 (Fig. 36h) and possibly spherule 14 from sample 14 (Figs. 38 a-c). Many spherules are strongly fractured or contain holes, implying that secondary alteration processes may have changed their compositions. Many of those, exhibit pronounced rims or strongly developed flow textures that resemble schlieren. However, there is no correlation between strongly fractured and compositionally hydrated spherules.

Spherules from the El’gygytgyn transition layer drill core occur randomly distributed within the suevite matrix. The abundance of spherules increases downwards the drill core from about 3 to 4 spherules per thin section at the first meters to about 15-20 spherules per thin section at a depth of about 315 mblf.

Compositionally, the spherules exhibit strong variations. Similar observations were also mentioned by Wittmann et al. (2013), who investigated spherules from the El’gygytgyn impactite drill core, ranging from 319.1 to 315.4 mblf. Based on this study, mixing calculations were obtained trying to reproduce spherule compositions from the major lithologies from the upper 620 m of the target rocks. These calculations, however, failed. He suggested that the spherules record different portions of the target rock sequence and/or reflect variable admixtures of an ultramafic projectile (Goderis et al. 2013). Two spherules (9b sph4 and sph7) of the transition layer yield mafic compositions and contain a well pronounced crystallite rim. No other spherule from the entire investigated section displays such a feature. It might reflect an admixture of a

basaltic target rock member. However, comparing the compositions from the basalts and andesites from the target rocks (e.g., Pittarello et al. 2013) to the mafic to intermediate spherules from the transition layer do not show a correlation. Especially, the MgO contents (in wt%) exhibit significant differences. The basalts and andesites from the target rock lithologies have MgO contents of about 3 to 4 wt%. The MgO contents of the mafic spherules are much higher, varying between 8 and 11 wt%. Figure 41d shows the MgO-FeO plot of the mafic to intermediate spherules and melt clasts of the transition layer, compared to compositions of possible projectile groups. The achondritic and CI-chondritic MgO-FeO ratios show similarities to those of the transition layer spherules.

Interelement ratios of Cr and Ni also indicate that some spherules of the El'gygytgyn transition layer might contain a meteoritical component (Fig. 41c). They exhibit Cr and Ni concentrations that do not correspond to those of the target rocks. Compared to the impactite drill core spherules (Wittmann et al. 2013), the spherules from the transition layer exhibit slightly higher Ni concentrations.

7.1.5 Bulk Rock Compositions and the Possible Contribution of a Meteoritical Component

Rare earth element distribution patterns that are chondrite normalized show enriched LREE patterns. Enriched LREE are typical for upper crustal rocks. The suevites, ignimbrites, and felsic rocks from the impactite drill core show the same distribution pattern for the REE (Pittarello et al. 2013). There is as well an Eu-anomaly, reflecting possible Ca-plagioclase removal during the volcanic target rock formation. The Ta trough is a characteristic of subduction zone magmas (Winter 2001) which is consistent with the overall geology of the OCVB and the adjacent volcanic provinces (e.g. Berlozhya Magmatic Association BMA).

Sample KME13 yields anomalous Au concentrations, compared to other samples from the transition layer. The Au contents of the target rocks and impactites that have been investigated by Pittarello et al. (2013), lie below detection limit or show low concentrations. The Au content of sample KME13 yields 16 ppm. All other samples from the transition layer have Au concentrations ranging from 1.3 to 2.6 ppm or lie below detection limit. Optical microscopic observations of the sample's thin section do not show any exceptional properties. The possibility of a contamination cannot be completely excluded. The OCVB, and especially the area around Lake El'gygytgyn, is also known for its epithermal gold and silver deposits (Sidorov et al 2009). These deposits might represent another explanation for this positive Au anomaly.

The siderophile elements Ni, Cr, and Co have been used to investigate the possibility of the contribution of a meteoritical component. As shown in Figs. 41 a-c the El'gygytgyn bulk rock samples exhibit similar Ni, Cr, and Co ratios as the target rocks. The Ir concentrations of all samples are below the detection limit. Based on these observations, the contribution of a meteoritical component, is either too small to be recognized or non-existent. However, since the El'gygytgyn transition layer spherules have shown possible admixtures of the projectile, the contribution is likely to small for the bulk rock samples to be recognized.

CHAPTER 8

Conclusions

The El'gygytgyn impact structure represents a unique opportunity to study shock metamorphic features in mainly siliceous volcanic rocks. In the course of this master's thesis, the transition layer, between the immediate impact deposits (and fallout) and post-impact crater fill, ranging from 311.467 to 317.38 mblf, has been the focus for petrographical and geochemical investigations. The rocks of the transition layer consist of suevite intercalated with lacustrine sediments.

The suevite itself contains abundant melt clasts and shards, spherules, volcanic and lithic fragments, and shocked, and non-shocked mineral clasts. The volcanic and lithic fragments are allocated to the lithologies of the target rocks. Based on petrographical and geochemical investigations of the numerous melt clasts and shards, and spherules, these can be classified as impact related melt particles and spherules. Shock metamorphic effects in minerals are only documented in quartz, and were firstly revealed by optical microscopy and further studied by electron microscopy. These shock effects include PFs and PDFs, diaplectic glass hosting coesite, and lechatelierite. Even the top of the onset of the transition layer contains shock metamorphic effects such as PDFs. Impact spherules, impact melts, silica diaplectic glass, and lechatelierite, however, occur about one meter below the onset of the transition layer. This section is marking the beginning of the more coherent impact ejecta layer.

The compositions of the different impact spherules show variations, but do correspond to those of the spherules that were investigated by Wittmann et al. (2013). Impact spherules and impact melts exhibit elevated Ni, Cr, MgO, and FeO concentrations. The comparison with the target lithologies and the impact spherules and melts from the impactite drill core (e.g.,Wittmann et al. 2013), indicated that there is in fact the contribution of a meteoritical component. Mixing calculations of impact spherule compositions from the El'gygytgyn impactite drill core, investigated by Goderis et al. (2013), modeled mixtures between rhyolitic ignimbrite target rock lithologies and 0.50 to 18 wt% of ordinary chondrite. The LL-chondrites, however, yielded the best fit. The MgO and FeO ratios of mafic impact spherules and mafic impact melt particles of the El'gygytgyn transition layer (Fig. 41d), however, show that an achondritic contribution would explain these elevated values. LL-chondrites are ordinary chondrites with low total Fe and low metal, compared to L- and H-chondrites, which are also part of the ordinary chondrites.

Chondrites result from undifferentiated parent bodies, whereas achondrites originate from differentiated parent bodies, from the mantle or from the crust.

References

Akinin V. V. and Miller E. L. 2011. Evolution of calc-alkaline magmas of the Okhotsk-Chukotka volcanic belt. *Petrology* 19(2):1-42

Akinin V. V., Layer P., Benowitz J., and Ntaflos Th. 2014. Age and composition of final stage of volcanism in Okhotsk-Chukotka volcanic belt: An example from the Ola Plateau (Okhotsk Segment). International Congress for Applied Mineralogy VI Proceedings 171-193.

Bailer-Jones C. 2011. Bayesian time series analysis of terrestrial impact cratering. Monthly Notices of the Royal Astronomical Society 416:1163-1180.

Belyi V. F. 1977. *Stratigraphy and Structures of the Okhotsk-Chukotka Volcanic Belt.* Nauka, Moscow 190 pp.

Belyi V. F. 1982. Basin of the El'gygytgyn Lake – Meteorite crater or geological structure of a recent stage of evolution of Central Chukotka? Tichookeeanskaya Geologia 5:85-92. In Russian.

Belyi V. F. 1988. *Topical questions of phytostratigraphy of middle Cretaceous of North- East USSR.* Magadan: North East Interdisciplinary Research Institute Magadan, Russian Academy of Sciences Far East Branch. 34 p. In Russian.

Belyi V. F. 1994. *The Geology of the Okhotsk-Chukotka Volcanic Belt.* SVKNII DVO RAN, Magadan. 76 pp. (in Russian)

Belyi V. F. and Belyaa B. V. 1998. *The Late Stage of the Okhotsk Chukchi Volcanic Belt development (the Emnyvaam River upper run area).* North East Interdisciplinary Research Institute, Magadan. Russian Academy of Sciences Far East Branch (in Russian). 107 pp.

Brigham-Grette J., Melles M., Minyuk P., and Scientific Party. 2007. Overview and significance of a 250 ka paleoclimate record from El'gygytgyn Crater Lake, NE Russia. *Journal of Paleoclimatology* 37:1-16.

Chipera S. J., Apps J.A. 2001. Geochemical stability of natural zeolites. In Natural zeolites: Occurrence, properties, applications, edited by Bish D. L. and Ming D. W. *Reviews in Mineralogy* vol. 45. Washington, DC.: Mineralogical Society of America. pp. 117-161

Dabizha A. I. and Feldman V. I. 1982. Gephysical characteristics of some astroblemes of USSR. *Meteoritika* 40: 91-101. In Russian.

Deer W. A., Howie R. A., Zussman J. 1992. *An Introduction to the Rock Forming Minerals.* Harlow, Essex, England: Longman Scientific & Technical. 696 pp.

Dietz R. S. and McHone J. F. 1976. El'gygytgyn: Probably the world largest's meteorite crater. *Geology* 4:391-392.

Faure G., Mensing T. M. 2007. *Introduction to Planetary Science: The Geological Perspective.* Dortrecht: Springer. 526 pp.

Feldman V. I., Granovsky L. B. Kapustkina I. G., Karoteeva N. N., Sazonova L. V., and Dabizha A I. 1981. Meteorite crater El'gygytgyn. In Impactites, edited by Marakhushev A. A. Moscow: *Moscow State University Press*. pp. 70-92. In Russian.

Filatova N. I. 1988. *Circum-oceanic volcanic belts.* Nedra, Moscow 296 pp. (in Russian).

French B. M. 1998. *Traces of Catastrophe: A Handbook of Shock-Metamorphic Effects in Terrestrial Meterorite Impact Structures.* LPI Contribution No. 954. Housten, Texas: Lunar and Planetary Institute. 120 p.

Glass B. P. and Burns C. A. 1988. Microkrystites—A new term for impact-produced glassy spherules containing primary crystallites. Proceedings, 18th Lunar and Planetary Science Conference pp. 455–458.

Goderis S., Witmann A., Zaiss J., Elburg M., Ravizza G., Vanhaecke F., Deutsch A., and Claeys P. 2013. Testing the ureilite projectile hypothesis for the El'gygtgyn impact: De- termination of siderophile element abundances and Os isotope ratios in ICDP drill core samples and melt rocks. Meteoritics & Planetary Science 48:1296-1324.

Govindaraju K. 1989. Compilation of the working values and sample description for 272 geostandards. *Geostandards Newsletter* 13:1-113.

Gurov E. P. and Gurova E. P. 1991. *Geological structure and rock composition of impact structures.* Kiev: Naukova Dumka Press. 160 p. In Russian.

Gurov E. P. and Koeberl C. 2004. Shocked rocks and impact glasses from the El'gygytgyn impact structure (Russia). *Meteoritics and Planetary Science* 39:1495-1508.

Gurov E. P., Koeberl C., Reimold W. U., Brandstätter F., and Amare K. 2005. Shock metamorphism of siliceous volcanic rocks of the El'gygytgyn impact crater (Chukotka, Russia). In *Large meteorite impacts III*, edited by Kenkmann T., Hörz F., and Deutsch A. GSA Special Paper 384. Boulder, Colorado: Geological Society of America. pp. 391- 412.

Gurov E. P., Valter A. A., Gurova E. P., and Kotlovskaya F. I. 1979. El'gygytgyn impact crater, Chukotka: Shock metamorphism of volcanic rocks (abstract). 10th Lunar and Planetary Science Conference. pp. 479–481.

Hörz F. 1970. Static and dynamic origin of kink bands in micas. *Journal of Geophysical Research*. 75:965-977.

Ispolatov V. O., Tikhomirov P. L., Heizler M., and Cherepanova I., Yu. 2004. New 40Ar/39Ar ages of Cretaceous continental volcanics from central Chukotka: Implications for initiation and duration of volcanism within the northern part of the Okhotsk Chukotka Volcanic Belt (northeastern Eurasia). *The Journal of Geology* 112:369–377.

Jarosewich E. 1990. Chemical analyses of meteorites. A compilation of stony and iron meteorite analyses. *Meteoritics and Planetary Science* 25:323-337

Jarosewich E., Clarke R. S. J., and Barrows J. N. 1987. The Allende meteorite reference sample. *Smithsonian Contributions to Earth Science* 27:1-49.

Kalinina E. A., Tikhormirov P. L., Moriguti T., and Nakamura E. 2008. The north of the Okhotsk Chukotka volcanic belt (NE Russia): sources of mafic magmas. Origin, Evolution and Dynamics of Earth. COE-21 International Symposium MISASA-III abstr. 155- 1656.

Koeberl C. 1998 Identification of meteoritic components in impactites. In Grady, M. M., Hutchison R., McCall G. J. H., and Rothery D. A. (eds) *Meteorites: Flux with Time and Impact Effects*. Geological Society London. Special Publications 140: 133-143.

Koeberl C. 2001.The sedimentary record of impact events. In: *Accretion of Extraterrestrial Matter throughout Earth's History* (ed. B. Peucker-Ehrenbrink and B. Schmitz). Kluwer Academic/Plenum Publishers. p 333-378.

Koeberl C. and Milkereit B. 2007. Continental drilling and the study of impact craters and processes – an ICDP perpective. In *Continental Scientific Drilling*, edited by Harms U., Koeberl C., and Zoback M. D. Heidelberg: Springer. pp. 95-161.

Koeberl C., Pittarello L., Reimold W. U., Raschke U., Brigham-Grette J., Melles M., Minyuk P. 2013. El'gygytgyn impact crater, Chukotka, Arctic Russia: Impact cratering aspects of the 2009 ICDP drilling project. *Meteoritics and Planetary Science* 48:1108- 1129.

Komarov A. N., Koltsova T. V., Gurova E. P., and Gurov E. P. 1983. *Determination of the El'gygytgyn crater impactites' age by fission track method*. Doklady Academii Nauk UkrSSR 10:11-13. In Russian.

Layer P.W. 2000. Argon-40/Argon-39 age of the El'gygytgyn event, Chukotka, Russia. *Meteroritics and Planetary Science* 35:591-599.

Mader D. and Koeberl C. 2009. Using Instrumental Neutron Activation Analysis for geochemical analyses of terrestrial impact structures: Current analytical procedures at the University of Vienna Geochemistry Activation Analysis Laboratory. *Applied Radiation and Isotopes* 67, 2100-2103.

Melles M., Brigham-Grette J., Minyuk P., Koeberl C., Adreev A., Cook T., Fedorov G., Gebhardt C., Haltia-Hovi E., Kukkonen M., Nowaczyk N., Schwamborn G., Wennrich V., and the El'gygytgyn Scientific Party. 2011. The Lake El'gygytgyn Scientific Drilling Project – Conquering Arctic challenges through continental drilling. *Scientific Drilling* 11:29-40.

Melosh H. J. 1989. *Impact Cratering: A Geologic Process*. Oxford Univ. New York. 245 pp.

Nekrasov I. A. and Raudonis P. A. 1963. *Meteorite craters*. Priroda 1:102-104. In Russian.

Newberry R. J., Layer P. W., Burleigh R.E., and Solie D. N. 1998. New 40Ar/39Ar dates for intrusion and mineral prospects in the eastern Yukon-Tanana Terrane, Alaska- Regional patterns and significance. Geologic studies in Alaska, edited by Gray J. E. and Riehle J. R. US Geological Survey 1996. Professional Paper 1595:131-159.

Nokleberg W. J., Parfenov L. M., Monger J. W. H., Norton I. O., Khanchuck A. I., Stone D. B., Scotese C. R., Scoll D. W., and Fujita K. 2011. Phanerozoic tectonic evolution of the Circum North Pacific. US Geological Survey. Professional Paper 1626:122p.

Obruchev S. V. 1957. *Across the tundra and mountains of Chukotka*. Moskow: State Press of Geography. 198 p. In Russian.

Pittarello L. and Koeberl C. 2013. Petrography of impact glasses and melt breccias from the El'gygytgyn impact structure, Russia. *Meteoritics and Planetary Science* 48:1236–1250.

Pittarello L., Schulz T., Koeberl C., Hoffmann J. E., Münker C. 2013. Petrography, geochemistry and Hf-Nd isotope evolution of drill core samples and target rocks from the El'gygytgyn impact crater, NE Chukotka, Arctic Russia. *Meteoritics and Planetary Science* 48:1160-1198.

Polin V. F. and Moll-Stalcup E. J. 1999. Petrological and geochemical criteria of the structural environment for formations of the Chukchi segment, Okhotsk-Chukotka volcanic belt. *Russian Journal of Pacific Geology* 18:29-47 (in Russian). 81

Raschke U., Reimold W. U., Zaag P. T., Pitarello L., and Koeberl C. 2013. Lithostratigraphy of the impactite and bedrock section of ICDP drill core D1c from the El'gygytgyn impact crater, Russia. *Meteoritics and Planetary Science* 48:1143-1159.

Raschke U., Zaag P. T., Schmitt R. T., and Reimold W. U. 2014. The 2011 expedition to the El'gygytgyn impact structure, Northeast Russia: Toward a new geological map for the crater area. *Meteoritics and Planetary Science* 49:978–1006.

Sidorov A. A., Volkov A. V., Belyi V. F., Alekseev V. Yu., and Kolova E. E. 2009. The gold-silver Okhotsk-Chukotka volcanic belt. *Geology of Ore Deposits* 51(6):441-455.

Simonson B. M. and Glass B. P. 2004. Spherule layers—Recorders for ancient impacts. *Annual Reviews of Earth and Planetary Sciences.* 2004:329–361.

Smit J. 1999. The global stratigraphy of the Cretaceous Tertiary boundary impact ejecta. *Annual Review of Earth and Planetary Science*. 27:75–113.

Sokolov S. D. Bondarenko G. Ye., Morozov O. L., Shekhovtsov V. A., Glotov S. P., Ganelin A. V., and Kravchenko-Berezhnoy I. R. 2002. The South Anyui suture, northeast Arctic Russia: facts and problems to solve. In *Tectonic Evolution of the Bering Shelf– Chukchi Sea-Arctic Margin and Adjacent Landmasses* edited by Miller E. L., Grantz A., and Klemperer S.L. Geological Society of America. Special Papers 360:209-224.

Stöffler D., Grieve R. A. F. 2007. Impactites. In *Metamorphic Rocks: A classification and glossary of terms, recommendations of the International Union of Geological Sciences*, edited by Fettes D. and Desmons J. Cambridge, UK: Cambridge University Press. pp. 82-92.

Stone D. B., Layer P. W., and Raikevich M. I. 2009. Age and paleomagnetism of the Okthosk-Chukotka Volcanic Belt (OCVB) near Lake El'gygytgyn, Chukotka, Russia. Stephan Mueller Special Publication Series 4:243-260.

Storzer D. and Wagner G. A. 1979. Fission track dating of El'gygytgyn, Popigai and Zhamanshin craters: No source for Australasian or North American tektites. *Meteoritics* 14:541-542.

Tagle R, and Berlin J. 2008. A database of chondrite analyses including platinum group elements, Ni, Co, Au, and Cr: Implications for the identification of chondritic projectiles. *Meteoritics and Planetary Science* 43:541-559.

Tikhomirov P. L., Kalinina E. A., Moriguti T., Makishima A., Kobayashi K., Cherepanova I. Yu., and Nakamura E. 2012. The Cretaceous Okhotsk-Chukotka Volcanic Belt (NE Russia): Geology, geochronology, magma output rates, and implications on the genesis of silicic LIPs. *Journal of Volcanology and Geothermal Research* 221-222:14-32.

Winter J. D. 2001. An introduction to igneous and metamorphic petrology. Upper Saddle River, NJ: Prentice Hall.

Wittmann A., Goderis S., Claeys P., Vanhaecke F., Deutsch A., and Adolph F. 2013. Petrology of impactites from El'gygytgyn crater: Breccias in the ICDP-drill core 1C, glassy impact melt rocks and spherules. *Meteoritics and Planetary Science* 48:1199–1235.

Zonenstrain L. P., Kuzmin M. I., and Natapov L. M. 1990. Geology of the USSR: A Plate-Tectonic Synthesis. Edited by Page B. M. *Amer. Geophys. Union: Geodynamic Series*. 21:242 pp.

List of Tables

List of Figures

Appendix A

Thin Section scans that were prepared by the Department of Mineralogy Natural History Museum in Vienna.

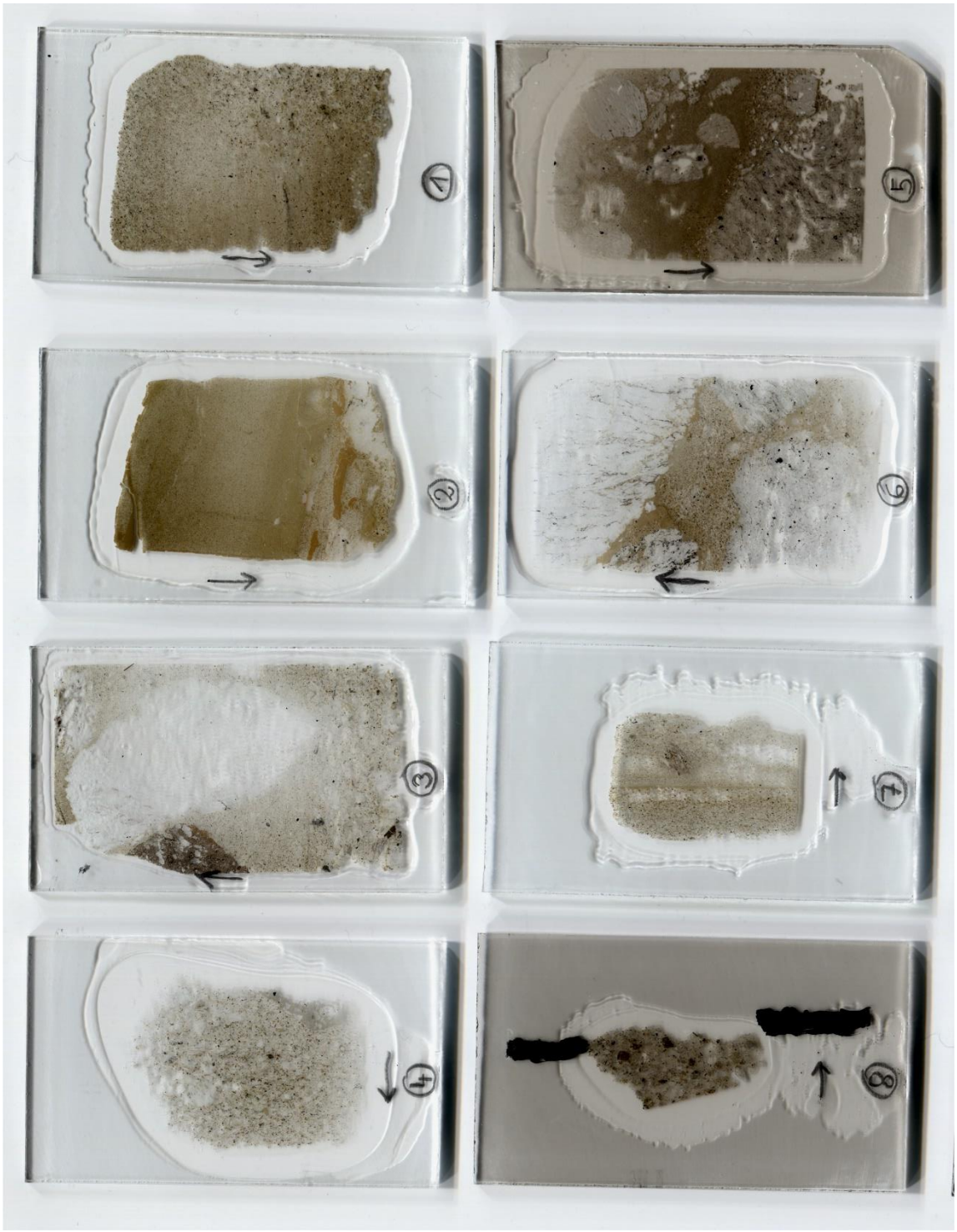

9a
12
4b
13
GLADAU
10
14
11
15a
2 mm
15
9

Thin Section scans that were prepared by the Department of Lithospheric Research at the University of Vienna.